Jül-4266

Institut für Festkörperforschung (IFF)
Elektronische Materialien (IFF-6)

Impact of the interface on the paraelectric-to-ferroelectric phase transition in epitaxial $BaSrTiO_3$ thin film capacitors

Rafael Plonka

Mitglied der Helmholtz-Gemeinschaft

JÜLICH
FORSCHUNGSZENTRUM

Impact of the interface on the paraelectric-to-ferroelectric phase transition in epitaxial $BaSrTiO_3$ thin film capacitors

Rafael Plonka

Berichte des Forschungszentrums Jülich ; 4266
ISSN 0944-2952
Institut für Festkörperforschung (IFF)
Elektronische Materialien (IFF-6) Jül-4266
D 82 (Diss., RWTH Aachen, Univ., 2007)

The complete volume is freely available on the Internet on the Jülicher Open Access Server (JUWEL) at http://www.fz-juelich.de/zb/juwel

Zu beziehen durch: Forschungszentrum Jülich GmbH · Zentralbibliothek, Verlag
D-52425 Jülich · Bundesrepublik Deutschland
☎ 02461 61-5220 · Telefax: 02461 61-6103 · e-mail: zb-publikation@fz-juelich.de

Interfaceeinfluss auf den Phasenübergang paraelektrisch-ferroelektrisch bei epitaktischen $BaSrTiO_3$ Dünnschichtkondensatoren

Immer höhere Speicherdichten im Bereich des sog. Dynamic Random Access Memory (DRAM) führen dazu, dass die Fläche der verwendeten Speicherkondensatoren drastisch reduziert werden muss. Damit einhergehend müssen die Schichtdicken des Dielektrikums im gleichen Maße verringert werden. Bei den derzeit verwendeten dielektrischen Materialien mit einer relativen Permittivität ε_r von ca. 10-25 liegen die hierfür erforderlichen Schichtdicken im Bereich weit unter 100 nm, was zu einer drastischen Zunahme der Selbstentladung der Kondensatoren führt. Alternative Materialien mit deutlich höherem ε_r sind die sogenannten Perowskite, die je nach Zusammensetzung eine theoretische Erhöhung der Speicherdichte etwa um den Faktor 20-50 gegenüber heute verwendeten Materialien zulassen. Bei dem am häufigsten in diesem Zusammenhang untersuchten Material $BaSrTiO_3$ (BST) ist jedoch eine Verringerung von ε_r bei Dünnschichten (kleiner 200 nm) beobachtet worden, welche mit dem sogenannten „dead-layer“ Modell erklärt wird: Hier wird vereinfachend angenommen, dass im Bereich der Grenzschicht zwischen Dielektrikum und Elektrode eine dünne Schicht mit verringerter Permittivität existiert, welche die effektive Permittivität der Struktur verringert.

Ziel dieser Arbeit ist es, die für die Verringerung der Permittivität verantwortlichen extrinsischen Einflüsse zu identifizieren und eliminieren sowie weitere intrinsische Beiträge zu untersuchen. Hierzu werden Probekondensatoren hergestellt, die aufgrund ihres einkristallinen epitaktischen Schichtwachstums eine nahezu defektfreie Kristallstruktur besitzen, und so direkte Rückschlüsse auf intrinsische Beiträge zum Phänomen der verringerten Permittivitäten zulassen. Anhand von temperaturabhängigen Messungen von Kapazität und Polarisation lassen sich Informationen über den schichtdickenabhängigen ferroelektrischen Phasenübergang sowie die aus dem dead-layer Modell abgeleiteten Größen „Interfacekapazität“ und „Bulkpermittivität“ gewinnen. Die experimentell ermittelten Werte werden im Rahmen einer theoretischen Diskussion und durch Erweiterung der Landau-Ginzburg-Devonshire Theorie zum ferroelektrischen Phasenübergang diskutiert. Hierzu wird neben dem Einfluss der Gitterfehlanpassung und den daraus resultierenden Verzerrungen auch der Beitrag des depolarisierenden Feldes diskutiert, so dass sowohl die Verschiebung der ferroelektrischen Phasenübergangstemperatur als auch die Temperaturabhängigkeit der Interfacekapazität besser verstanden werden können.

Bei der Untersuchung von Kondensatoren mit $SrRuO_3$ (SRO) als oberer Elektrode kann eine exzellente epitaktische Grenzfläche zwischen Dielektrikum und Elektrode nachgewiesen werden. An diesen Proben liegt eine starke Abhängigkeit der gemessenen Permittivität von der Amplitude des verwendeten Kleinsignalanregungssignals vor, wohingegen Proben mit Pt als oberer Elektrode diese Abhängigkeit nicht aufweisen. Die Ursache für dieses Verhalten kann über eine generelle Koexistenz von relaxor- und ferroelektrischen Eigenschaften in den BST-Proben erklärt werden, die im Fall der Pt-Proben jedoch aufgrund der schlechteren Grenzfläche zwischen Pt und BST kaum in Erscheinung tritt.

Impact of the interface on the paraelectric-to-ferroelectric phase transition in epitaxial $BaSrTiO_3$ thin film capacitors

The ever increasing memory densities of the so called Dynamic Random Access Memory (DRAM) lead to a drastic reduction of the area of the incorporated storage capacitors. As a consequence, the film thickness of the used dielectrics has to be decreased in a similar way. When considering state-of-the-art dielectrics showing a relative permittivity e_r of around 10-25, the necessary thicknesses are well below 100 nm, which leads to a drastic increase of the self-discharge in the capacitors. Alternative materials that display much higher permittivity values are the so called perovskites, which depending on their composition allow a theoretical increase of the memory density about a factor of 20-50, compared to standard materials. Investigations on $BaSrTiO_3$ (BST) as the most intensively studied material in this context however revealed, that the permittivity is strongly suppressed when dealing with thin films (below 200 nm). This behavior is often tried to explain using the so called “dead-layer” model, which assumes a thin layer with reduced permittivity at the electrode/dielectric interface, resulting in an overall decrease of the measurable permittivity.

The goal of this thesis is to identify and eliminate the extrinsic influences responsible for the observed decrease of the permittivity, as well as to examine additional intrinsic effects. For this purpose, capacitor samples are fabricated, which due to their epitaxial single-crystalline film growth show a crystal structure nearly free of any defects, thus allowing to gain further insight into the phenomenon of the reduced permittivity. Electrical analysis from temperature dependent measurements of capacitance and polarization give additional information about the thickness dependent ferroelectric phase transition as well as the values of “interface capacitance” and “bulk permittivity” derived from the dead-layer model. The experimentally achieved values are discussed theoretically using the approach of a modified Landau-Ginzburg-Devonshire theory of the ferroelectric phase transition. In addition to the influence of the misfit dislocation and its contribution to the strain in the films, also an impact of the depolarizing field will be considered, such that the shift of the phase transition temperature as well as the temperature dependence of the interface capacitance can explained more accurate.

Investigations of samples with an $SrRuO_3$ (SRO) upper electrode reveal excellent epitaxial interfaces between dielectric and electrodes. However, these samples show a strong dependence of the permittivity on the amplitude of the incorporated small signal excitation voltage, whereas this behavior cannot be found on samples wit Pt upper electrode. The reason for this peculiarity might be explained with a general co-existence of relaxor- and ferroelectric properties in the BST samples, which in case of Pt electrodes is suppressed by the considerably deteriorated interface between BST and Pt.

Preface

This dissertation was written during my Ph.D. studies at the Institut für Werkstoffe der Elektrotechnik II (IWE II) of the Rheinisch Westfälische Technische Hochschule Aachen, Germany (RWTH Aachen), with regular stays at the Institut für Festkörperforschung (IFF) at the Forschungszentrum Jülich, Germany.

I would like to express my gratitude to Prof. R. Waser for allowing me to do research at the Institut für Werkstoffe der Elektrotechnik and the Institut für Festkörperforschung in the exciting field of the high-k dielectrics for DRAM Applications. I highly appreciate his advice and support.

I am also indebted to Prof. B. Rembold who kindly agreed to be the co-examiner in the jury.

Many thanks also to the following people, who by their valuable support made this dissertation possible:

Dr. R. Dittmann for giving me an excellent supervision during these five years of research and her support in the numerous iterations of proof-reading of the manuscript.

Dr. habil N.A. Pertsev for generously offering me to use his theoretical results together with my experimental findings, as well as for his helpful annotations to the manuscript.

Dr. U. Böttger for his support in the IWE group and the important advices in the final writing phase.

Dr. C. Kügeler for giving me lots of helpful advices in the process of writing the thesis and preparing myself for the exam, his careful proof-reading, being a great office-mate & travel companion and his hospitality whenever necessary.

Dr. S. Hoffmann-Eifert for the recommendation of a rather unusual approach that finally helped to explain the last remaining questions.

Dr. C.L. Jia and J.Q. He for providing the excellent HRTEM images.

Dr. T. Schneller and R. Thelen for guidance in the field of chemistry and the spontaneous help getting dry-shod to the thesis delivery.

T. Pössinger and D. Leisten for supporting me in the most critical phases of desktop-publishing and the admission to spectacular football matches.

U. Evertz, M. Gerst, P. Roegels, H. Pütz and J. Heiss for assistance in the numerous hardware- and software-related problems in the last years.

D. Erdoglia and G. Wasse for supplying Pt top-electrodes, assistance in SEM micrographs and their helpful advices.

U. Kall, Dr. P. Gerber, Dr. S. Tappe, Dr. T. Hölbling, Dr. C. Kügeler, C. Dehoff, S. Menzel, D. Bräuhaus and H. Kambara for being great office mates and providing a pleasant work climate in the past years.

M. Heins and M. Garcia for their important support, especially at the final phase of submitting the thesis.

I am very much obliged to all co-workers from IWE and IFF which in one or the other way contributed to the successful completion of this work.

Special thanks go to my parents, who supported me in the last years whenever necessary. The encouragements of my family have been very helpful to regain my motivation at certain times.

Dedicated to my parents and Mirjam Blum

Contents

1 Introduction 1
1.1 Motivation 1
1.2 State of the Art 2
1.3 Objectives 4
2 Ferroelectric Materials and their Properties 7
2.1 Crystallographic Considerations and Definition of a Ferroelectric 7
2.2 General Features of Ferroelectric Crystals 8
2.3 Material Systems 12
2.4 Mechanical Boundary Conditions 16
2.5 Thermodynamics of Ferroelectrics 18
3 Thickness Dependence of Dielectric Properties in Ferroelectrics 27
3.1 Extrinsic Influences 30
3.2 Intrinsic Influences 32
4 Experimental Methods 41
4.1 Sample Preparation 41
4.2 Electrical Characterization Methods 44
4.2.1 Small Signal Measurements 44
4.2.2 Hysteresis Measurements 46
5 Results 49
5.1 Physical Characterization: X-Ray Diffraction 49
5.2 Electrical Characterization: Small Signal Response 52
5.2.1 Voltage Dependence of the Small Signal Capacitance 53
5.2.2 Temperature dependence 59
5.2.3 Loss tangent 68
5.3 Electrical Characterization: Large Signal Hysteresis Measurements 69
5.4 Summary of the Experimental Results 74
6 Discussion 77
6.1 Influences from the Measurement Voltage Level 77
6.2 Strain Effects 87
6.3 Depolarizing Fields and their Competition with Strain Effects 93
6.4 Comparison with experimental Values 98
6.5 Validation of the Theoretic Findings 99
7 Conclusion 103
7.1 Summary 103
7.2 Outlook 105
References 107

Used Symbols and Abbreviations

Symbols

a	Lattice constant
a_i, a_{ij}, a_{ijk}, ...	Dielectric stiffness and higher order stiffnesses
A	Capacitor area
b	Lattice constant
c	Lattice constant
c, c_b, c_{eff}, c_i, c_t	capacitance density, bulk ~, effective ~, interface ~, total ~
C, C_i, C_{rev}, C_S	Capacitance, Interface ~, Reversible ~, Storage ~
C_{eff}	Effective Capacitance
C	Curie constant
d	molecular diameter
D, D_i, D_b	Dielectric displacement, ~ in the interface, ~ in the bulk
e	Electron charge
E, E_b, E_c, E_{dep}	Electric field, ~ in the bulk, coercive field, Depolarizing field
E_{AC}	Small signal excitation field
E_F, E_{pot}	Fermi energy, Potential energy
f	Frequency
F	Free energy
G, $\tilde{G}$	Gibbs Free Energy, Modified ~
g_i	Coefficients
k_B	Boltzmann constant
K_s, K_{sc}	Sensitivity of the permittivity on strain
l, l_{TF}	screening length, Thomas-Fermi ~
L	Debye Length
n_0	Free electron density
N	gas concentration
p	Pressure
P, P_s	Electrical polarization, Spontaneous ~
P_r, P_{r+}, P_{r-}	Remanent polarization, Positive ~, Negative ~
$P_{r,rel+}$, $P_{r,rel-}$	Positive relaxed polarization, Negative relaxed polarization
Q	Heat
Q	Charge
Q_{ln}	Electrostrictive constants
r_0	Penetration length
R_i	Internal resistor
s_{ln}	Elastic compliances
S	Entropy
S_m, S_m^*	Misfit strain, Critical ~
t, t_c	Thickness, Critical ~
t_{eq}, t_i, t_{phys}	Equivalent dielectric ~, Interface ~, Physical ~
T, T_C, T_0	Temperature, Phase transition ~, Curie-Weiss ~
ΔT_C	Shift of the Curie Temperature
T_g	Film growth temperature

U	Internal energy
V, V_c, V_{c+}, V_{c-}	Voltage, coercive ~, positive coercive ~, negative coercive ~
W	Work
x_i	Misfit strain (same as S_m)

Greek Symbols

α_i	Thermal expansion coefficient
β, γ	Critical exponent
δ	Loss angle
$\varepsilon, \varepsilon_0$	Permittivity, Vacuum ~
$\varepsilon_b, \varepsilon_i, \varepsilon_r$	Permittivity of the bulk, ~ of the interface, Relative ~
ε_m	Permittivity of the electrode material
η	Kinetic fitting parameter
κ	Fitting parameter
λ	mean free path length
ρ	Specific conductivity
ρ	Dislocation density
ρ	charge density
σ_0	free screening charge
σ_i	Mechanical stress
χ_e	Dielectric susceptibility

Abbreviations

ABO_3	Perovskite type crystal
AC	Alternating current
BST	Barium Strontium Titanate $Ba_xSr_{1-x}TiO_3$
BTO	Barium Titanate $BaTiO_3$
CV	Capacitance vs. voltage
DC	Direct current
DRAM	Dynamic random access memory
DUT	Device under test
HRTEM	High resolution transmission electron microscopy
LGD	Landau-Ginzburg-Devonshire
PLD	Pulsed laser deposition
PV	Polarization vs. voltage
RT	Room temperature (~ 300 K)
SNR	Signal to noise ratio
STO	Strontium Titanate $SrTiO_3$
SRO	Strontium Ruthenate $SrRuO_3$
TEM	Transmission electron microscopy

1 Introduction

1.1 Motivation

The use of ceramic thin films exhibiting ferroelectric, pyroelectric, piezoelectric, electro-optical and magneto-optical properties in combination with silicon technologies (e.g. CMOS) allows for the development of a variety of novel functional devices in the fields of memory, sensors, actuators and modulators [1-6]. Restricting on the memory sector, it is obvious that in recent years the performance of mobile electronic devices such as digital cameras, PDAs, cell phones, notebooks and even wearable electronics has been increased rapidly. As a consequence, the need for low power-consuming non-volatile high-density memory technologies compatible with the powerful processors of those devices has increased, too. On the other hand, the efficiency of non-mobile electronic applications (e.g. desktop computers) has been improved in a similar way: Here, the incorporated memory devices were mostly optimized to achieve higher storage densities and faster data transfer rates, whereas the power consumption plays only a secondary role. According to the above considerations, the application of electroceramics in storage capacitors is promising in the following two cases:

- The development of novel, non-volatile ferroelectric semiconductor memories (FeRAM) could be achieved by the implementation of ferroelectric ceramics such as lead zirconate-titanate, $Pb(Zr_{1-y}Ti_y)O_3$ or strontium bismuth tantalate, $SrBi_2Ta_2O_9$. This type of memory exhibits high switching cycles (typically > 10^{14}) as well as fast write access times (< 50 ns) and therefore is a potential candidate for replacing EEPROMs as a widely used non-volatile memory in mobile applications [7,8].
- As the current state of the art dielectrics in dynamic random access memory (DRAM), Al_2O_3, Ta_2O_5 as well HfO_2 were incorporated, which show maximum permittivity values ε_r between 10 and 26. For a higher miniaturization level (higher memory density), the current area of the storage capacitor has to be further reduced while at the same time the thickness of the dielectric layer must be decreased substantially to maintain a sufficiently high capacitance level. This in term leads to unfavorable high tunneling currents through the dielectric, which means a faster self-discharge of the capacitor and hence a possible dysfunction of the memory device. As an alternative, the integration of thin film ceramic perovskites display-

ing high permittivity values into DRAM storage capacitors offers storage densities 20 to 50 times higher than what can be achieved at present, while the dielectric thickness would not be changed. These materials are thought to have the potential for replacing the currently used dielectrics, according to the latest semiconductor roadmaps [9]. One of the most studied materials (thus the model material) in this context is $Ba_xSr_{1-x}TiO_3$ (BST), and here especially its composition with $x = 0.7$, showing dielectric permittivities ε_r as high as 15,000 [10-12].

However, several obstacles have been detected during the general implementation of perovskite ceramics into memory applications: Amongst others, these include the adjustment of the necessary deposition temperatures to levels compatible with the silicon technology and general compatibility issues of the used materials. In the case of FeRAM, failure mechanisms in ferroelectrics such as fatigue, imprint and retention have to be considered, which partly could be handled even though physical explanations have not always been found. In the DRAM case, a reduction of the effective permittivity with decreasing thickness of the incorporated high permittivity materials has been observed as the most restraining challenge.

Thus, the goal should be to minimize the difficulties that by now do not allow for a successful implementation of ferroelectrics into memory devices considering a commercial point of view. Therefore, it is indispensable to get a detailed knowledge of the variety of material properties derived by exhaustive experimental characterizations as well as by theoretical predictions utilizing the inherent physical mechanisms and theories. In this context, much of the work will be spent on the electrode/dielectric interfaces as they are assumed to be accountable for the majority of the hindering behavior.

1.2 State of the Art

A deterioration of ferroelectric properties can be observed when the dimensions of thin films become more and more reduced, as it is mandatory for the ever-growing integration densities in modern microelectronic applications [13]. At thicknesses in the region well below 50 nm, the dielectrics approach length scales associated with characteristics of the ferroelectric material and electrode interfaces themselves. It is also expected that reducing the lateral dimensions of the structures could alter the response of the ferroelectric [14]. The influence of the size on

the properties of ferroelectrics is an important factor determining the way to implement these materials in future generations of microelectronic structures. With respect to possible memory applications, it has been found that by decreasing the thickness of capacitors with high permittivity dielectrics such as BST, the measured permittivity ε_r does not remain constant but rather decreases significantly [15]. Hence, ε_r no longer appears to be a material constant but rather seems to be an effective value that depends on the capacitor thickness. Additional to the general permittivity decrease, it has also been found that the former pronounced ferroelectric to paraelectric phase transition in high permittivity materials becomes strongly suppressed or even hardly noticeable when dealing with thin films of the same composition [13]. Various approaches have been used that attribute the observed phenomena to a so called interface capacitance, hence a thin layer with reduced permittivity that acts electrically in series to the actual high permittivity capacitor and therefore leads to a reduction of the overall capacitance. Experimentally, the idea of this series connection has been confirmed according to the measured thickness dependent permittivity by a number of authors [13-18], whereas a physical evidence of such a low permittivity layer (or „dead layer“) has never been found by means of any microstructural investigation. Several different mechanisms have been discussed to be responsible for the observed phenomenon, which include changes in the phonon spectrum at the interface due to broken lattice periodicity [19,20] or crystal defects related to the interface [21-23], chemically different reaction layers [24-26], electronic surface- or interface-states [27-29], electric field penetration into the electrode material and corresponding screening length issues [30-32], whereas the hardening of the soft phonon throughout the whole ferroelectric film is a result of all intrinsic effects [33], and is strongly related to the existence of depolarizing fields [34]. In general, the use of oxide electrode materials such as $SrRuO_3$ (SRO) instead of Pt has an improving effect on the observed permittivity decrease with reduced thickness, as reported from several authors [35-37].

Taking a look at the measured polarization in thin film ferroelectrics, it can be found that in general the coercive field becomes increased, while the remanent polarization drops as the film thickness is decreased [38,39]. This thickness dependence is generally attributed to a surface layer and depends strongly on the properties of the ferroelectric/electrode interface. Such a surface layer can appear as a consequence of non-stoichiometry near the film surface or damage induced by the electroding process, but may also be caused by intrinsic factors. The different

reported polarization behavior in general can be explained by the different preparation techniques used, which may induce different properties in the ferroelectric close to the electrodes. Investigations on BST as a ferroelectric model system easily allow the study of ferroelectric properties such as the remanent polarization P_r, the coercive field E_c and the phase transition temperature T_C, which are all strongly influenced by the particular choice of the electrode/dielectric interface.

In summary, it should be noted that there exists a variety of extrinsic as well as intrinsic influences that cause a suppression of the dielectric permittivity and a frustrated ferroelectric-to-paraelectric phase transition. Among those, grain boundaries from polycrystalline films, tensile strains from crystal lattice mismatch or deteriorated interfaces due to defects and interdiffusion as well as different screening properties of the electrodes have the most critical impact.

1.3 Objectives

From the previous paragraph it follows, that in order to investigate the pure intrinsic influences it is especially mandatory to get rid of all extrinsic influences. This will be accomplished most of all by choosing an epitaxial growth technique and a single crystalline substrate to prepare high quality ferroelectric thin films free from grain boundaries and results in interfaces without interdiffusion layers or defects. Thus, the extraction of intrinsic material properties can be accomplished and a successful comparison between BST capacitors electroded with Pt and SRO can be performed.

Besides a comprehensive introduction into the principles of ferroelectric materials and the experimental methods for the fabrication and characterization of thin film capacitors, the following main tasks will be accomplished in this work:

- Epitaxially grown thin film capacitors with dielectric layers of various BST thicknesses will be fabricated. These capacitors show a high crystalline quality and allow an extensive analysis of their electrical properties.
- Starting from capacitance and polarization measurements at room temperature, the electrical analyzes will be carried out in a wide temperature range under systematic variations of the applied voltage and frequency. This allows a thickness and temperature dependent anal-

ysis of the key properties and will permit the evaluation of the phase transition temperature.

- The thus determined measurement results will be compared with those reported in the literature for comparable studies to evaluate the achieved quality of the experimental work. A theoretical discussion in the light of a thermodynamic model based on the Landau-Ginzburg-Devonshire (LGD) theory of ferroelectric materials finally concludes the presented studies.

2 Ferroelectric Materials and their Properties

This chapter deals with the basic properties of ferroelectric materials that will be relevant in this work. For a detailed description of the fundamentals of ferroelectric phenomena, the reader is advised to the standard text books [5,40-49] or review articles [50-52].

2.1 Crystallographic Considerations and Definition of a Ferroelectric

Among the classical 32 crystal classes (or point groups) describing all crystalline material, 11 classes have a center of symmetry and are therefore called *centrosymmetric*. Applying an electric field to such a centrosymmetric crystal will create a mechanical strain that does not change its sign, regardless to the direction of field. The strain is proportional to the square of the applied field and this quadratic effect is called *electrostriction*. Electrostriction occurs in *all* substances, no matter if it is crystalline or amorphous, solid or fluid.

The remaining 21 classes do not have a center of symmetry, they are non-centric and show (except for one) the *piezoelectric effect*: Piezoelectricity means that the crystal exhibits electric polarity when exposed to strain. This effect is a *linear* one, i.e. reversing the sign of the stress will cause a reversed polarity. By applying an electric field to the crystal, it will be stretched or compressed, corresponding to the polarity of the field. This is the *converse* piezoelectric effect.

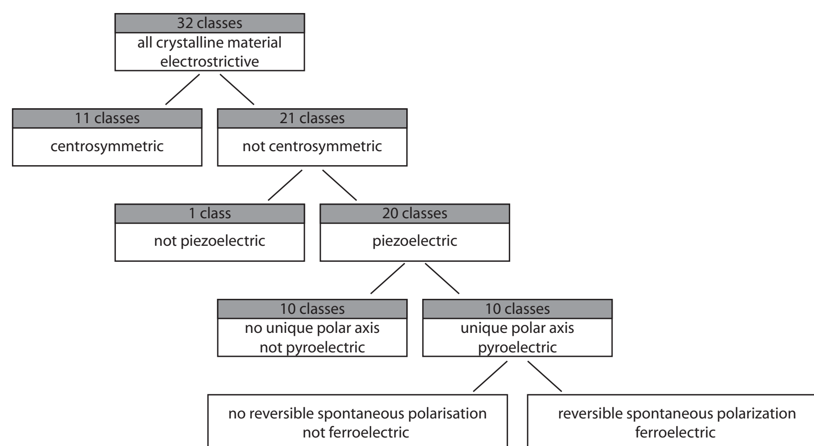

FIGURE 2.1:
Ferroelectric crystals and their position among the 32 general crystal classes.

From those 20 classes, ten have a *unique* polar axis, i.e. an axis which shows different properties on the one end than on the other end. These crystals are called polar and exhibit a spontaneous polarization which is dependent on temperature. These are the *pyroelectric* crystals.

If the direction of the spontaneous polarization in such a pyroelectric crystal can be switched between two stable states by applying an electric field, the crystal is called *ferroelectric*. For ferroelectrics it is therefore a necessary attribute to belong to one of the ten pyroelectric crystal classes *as well as* to have a reversible spontaneous polarization.

2.2 General Features of Ferroelectric Crystals

Ferroelectric Hysteresis

Measuring the relationship between the applied electric field and the electric polarization in a ferroelectric material, a typical hysteresis curve results as displayed in Figure 2.2. The ideal case of a single domain[1] crystal is shown in Figure 2.2 (a): Here, a variation of the electric field E leads to a linear increase of the polarization P, while for fields exceeding the coercive field E_c, a jump of the polarization occurs. In the zero field case, the polarization remains either at the positive or negative spontaneous polarization P_s. Figure 2.2 (b) shows the hysteresis curve of a polydomain sample: Starting at the virgin state (the polarization is pointing in an equal portion of volume to the positive *and* negative direction), a part of the negatively oriented domains will be switched over into the positive direction by increasing the electric field (path *AB*), and the polarization increases strongly until the saturation state is reached (path *BC*). Here, the complete volume is aligned in the positive direction and the crystal consists now of one single domain. Decreasing the field does not bring the net polarization in generally back to zero but rather follows the path *CD*, which means that some of the domains will stay positively oriented without applied field and the crystal exhibits a remanent polarization P_r. Extrapolating the saturation path *BC* back to the polarization axis, the intercept represents the spontaneous polarization P_s. To decrease the polarization then further to zero, it is necessary to apply a negative electric field (portion *DE*). The electric field corresponding to this zero polarization state is called the *coercive field* E_c. Additional decrease of the field will cause all dipoles to align in the negative orientation (portion *EF*), after which the cycle can be completed

1. A domain describes a fraction of volume in which the polarization is oriented uniformly

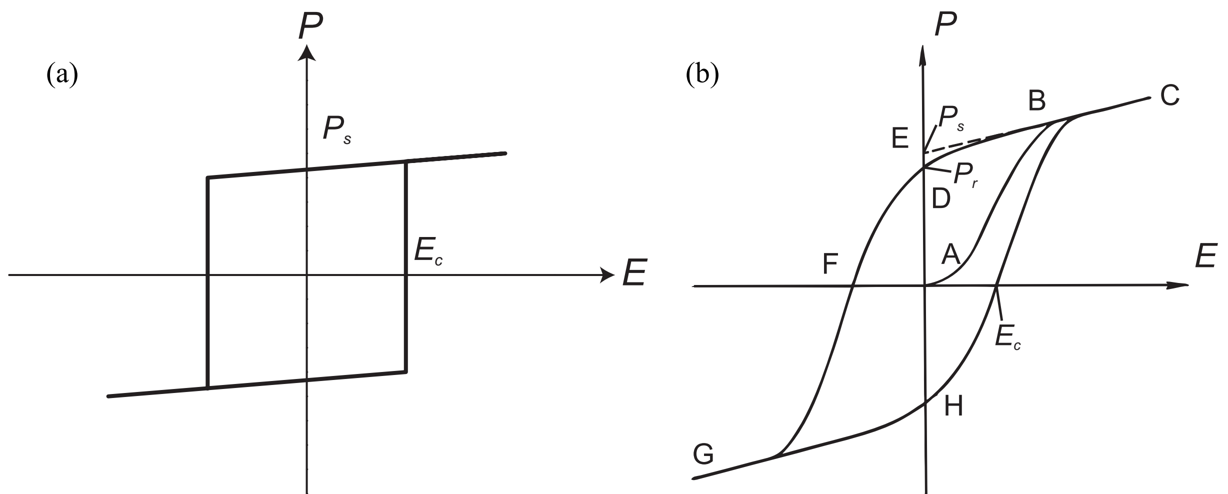

Figure 2.2:
Schematic drawing of a ferroelectric hysteresis loop
(a) Single domain
(b) Polydomain sample

by reversing the field once again (portion *FGC*).

One then finds a hysteresis loop (*CDFGC*) as the relation between P and E, which is the most important electrical characteristic of a ferroelectric crystal. Actually, the y-axis from Figure 2.2 should be denoted as the dielectric displacement

$$D = \varepsilon_0 E + P, \tag{2.1}$$

where in general $\varepsilon_0 E$ denotes the vacuum contribution to the displacement D caused by an externally applied field E, and P represents the electrical polarization of the material, independent of its cause. Since in ferroelectric materials the polarization is by many orders of magnitude larger than the vacuum term, the approximation $D \approx P$ is justified. Additional to the ferroelectric contributions, the polarization consists of dielectric contributions from the susceptibility of the material (ionic and electronic polarization).

Dielectric Constant and Loss

The relative dielectric constant ε_r or $\varepsilon/\varepsilon_0$ is the ratio between the charge stored on an electroded slab of material brought to a given voltage and the charge stored on a set of identical electrodes separated by vacuum. It is often simply denoted as *the dielectric constant* and is the dimensionless multiplier of the vacuum permittivity ε_0 ($8.8542 \cdot 10^{-12}$ As/Vm). For general materials the

value of ε_r is low, under 5 for organic materials and under 20 for most of the inorganic solids. Ferroelectrics, however may possess a much higher dielectric constant, with values typically about several hundred or even several thousand. When applying alternating voltages, the charge stored on a dielectric has both real (in phase) as well as imaginary (out of phase) components, which may be due to resistive leakage or dielectric absorption. The loss is then expressed by the ratio of the out-of-phase component to the in-phase component, which is usually called the loss tangent or $\tan\delta$. Considering ε' and ε'' as real and imaginary components of the complex permittivity $\underline{\varepsilon} = \varepsilon' - j\varepsilon''$, the loss tangent can be calculated by $\tan\delta = \varepsilon''/\varepsilon'$.

Connection between Hysteresis and Dielectric Constant

According to an electrostatic approach, the dielectric constant $\varepsilon = \varepsilon_r \varepsilon_0$ is defined as the derivative of the dielectric displacement D with respect to the field E. The dielectric susceptibility χ_e is analogously defined as the derivative of the polarization P with respect to the field E, divided by the vacuum permittivity ε_0. Applying this derivation on (2.1) and dividing by ε_0, the relative dielectric constant can be expressed as

$$\varepsilon_r = 1 + \chi_e. \tag{2.2}$$

This definition is valid only for normal *linear* dielectrics, in which the relationship between D and E is linear up to high values of E. In ferroelectric crystals however, the definition of ε_r becomes more complicated due to the *non-linear* relationship between D and E (Figure 2.2). Here, the dielectric constant ε_r is defined as the slope of the D-E curve at the origin:

$$\varepsilon_r = \frac{1}{\varepsilon_0} \frac{\partial D}{\partial E}\bigg|_{E=0} \tag{2.3}$$

In the case of materials in their paraelectric phase, the spontaneous polarization disappeared and the polarization is simply related to the electric field by

$$P = \varepsilon_0 \chi_e E. \tag{2.4}$$

Combining (2.1) together with (2.4), this leads to

$$D = \varepsilon_0(1 + \chi_e)E = \varepsilon_0 \varepsilon_r E, \tag{2.5}$$

giving the linear relation between electric displacement and electric field. It has to be mentioned that the dielectric permittivity does not have to be constant and in certain circumstances also depends on the applied field.

Temperature Dependence

In general, ferroelectric materials perform a phase transition from the (low temperature) ferroelectric phase to the (high temperature) paraelectric phase (strong analogy with ferromagnetism). The temperature at which this transition occurs is called the *Curie temperature* T_C, above which no ferroelectricity is observable. The corresponding material condition is then called the paraelectric phase. Also, the dielectric constant ε_r exhibits some kind of anomaly at the transition temperature. In many ferroelectrics (including those that were investigated in this work), the temperature dependence of the dielectric constant above the phase transition obeys a quite simple law, the so-called *Curie-Weiss law*:

$$\varepsilon_r = \frac{C}{T - T_0} \tag{2.6}$$

Here, C means the Curie-Weiss constant and T_0 denotes the paraelectric Curie point (or extrapolated Curie point or Curie-Weiss temperature). It should be noted that T_C and T_0 generally do not coincide, which is one of the most frequent errors in this subject. In a ferroelectric with a second order phase transition (properties such as lattice constants, dielectric constant, polarization, etc., change rather continuously with temperature), these two temperatures may be effectively the same. In the case of first order transitions, however (above mentioned properties change rather discontinuously, i.e. exhibit “jumps”), the Curie temperature can be more than 10K lower than the Curie point.

2.3 Material Systems

Most investigations in this work were performed on Barium-Strontium Titanate $Ba_xSr_{1-x}TiO_3$ (BST) thin films. Since this material is derived from the prototypic materials Barium Titanate $BaTiO_3$ (BTO) and Strontium Titanate $SrTiO_3$ (STO), first an introduction to BTO and STO will be given.

Barium Titanate

The ferroelectric solid solution system BTO is one of the most extensively studied ferroelectric materials. Its anomalous dielectric properties were discovered on ceramic samples independently from each other around 1943 by Wainer and Salomon in the USA, Ogawa in Japan and Wul and Goldman in Russia. Its ferroelectric properties were reported 1945-1946 by von Hippel et al. [53] and independently by Wul and Goldman [54].

Shown in Figure 2.3 (a) is the unit cell[2] of BTO, which is a typical specimen of the perovskite[3] type crystals with the general formula ABO_3. One finds a nearly cubic cell structure where Ba^{2+} ions reside on the corners (*A*-sites), in the center lies the Ti^{4+} ion (*B*-site) and in the face centers are the O^{2-} ions. At higher temperatures (above T_C = 120 °C), the crystal is in its paraelectric phase and the structure is exactly cubic with a center of symmetry, lacking any piezoelectric or ferroelectric properties. Below T_C, a phase transition occurs that distorts the cu-

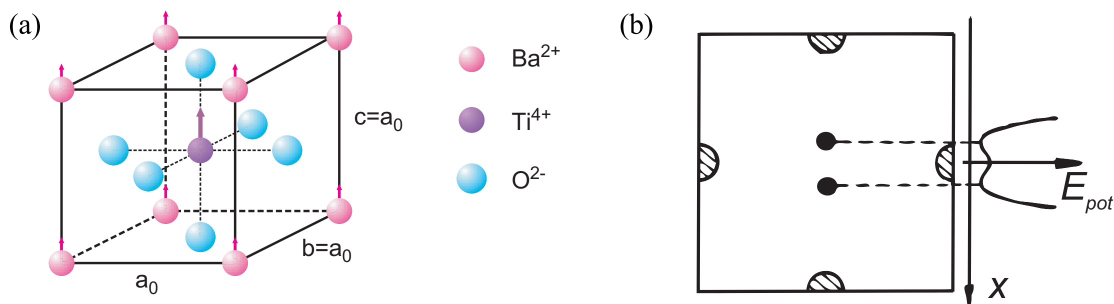

FIGURE 2.3:
(a) The cubic (paraelectric) unit cell of $BaTiO_3$. Possible displacements of the sublattices for the tetragonal distortion are indicated by arrows.
(b) Cross sectional view of the tetragonal distorted BTO unit cell. Shown are the two stable states of the Ti^{4+} ion and the potential energy E_{pot} depending on its position [48].

---

2. The unit cell is a spatial arrangement of atoms which is tiled in three-dimensional space to describe the crystal.
3. Perovskite is a name of the mineral CaTiO3 which itself belongs to the orthorhombic system. “Perovskite type structure” means that a structure has an atomic arrangement such as Figure 2.3 (a).

bic cell into a tetragonal shaped cell. Whereas one axis of the crystal becomes elongated (the so called c-axis), the other two crystal axes become compressed (a-axes). As can be seen in Figure 2.3 (b), the potential energy E_{pot} of the Ti^{4+} ion now has two minima that mark the two stable states of polarization. Using an external electric field, it is possible to switch between those states, hence to reverse the polarization, so $BaTiO_3$ fulfills the essential requirement for ferroelectric materials. Since the necessary energy to overcome the maximum in E_{pot} and to switch the Ti^{4+} ion from one to another state is very low, also the field from surrounding dipoles could be strong enough to polarize the crystal, resulting in a spontaneous polarization P_s.

Besides the already mentioned cubic and tetragonal phases, further crystal configurations of BTO are possible. As can be seen in Figure 2.4 (a), there exist three different phase transitions for BTO in the temperature range 150-400 K, connecting the four possible crystal phases. Figure 2.4 (b) shows the dependence of the lattice constants of the BTO unit cell depending on the temperature, hence the resulting phases at those temperatures. Below 180 K the crystal is in its rhombohedral phase with the polarization along the space diagonal. Up to 275 K, the orthorhombic phase exists and the polarization is oriented in parallel to the face diagonal. Then the crystal becomes tetragonal shaped with a polarization in the <001> direction, parallel to the (longer) c-axis. The phase transition from tetragonal to cubic occurs at the Curie temperature T_C which is at about 390K. Above this critical temperature no ferroelectric polarization remains, the crystal has a symmetry center which is the central Ti^{4+} ion. It can be seen that the phase transitions occur with a certain temperature hysteresis, which means that depending on the direction of the temperature change (cooling or heating) of the crystal the transition temperatures may vary by about ten K. Since all but the cubic phase lack a center of symmetry, there exists a switchable polarization in the crystal with different direction for each of these phases (Figure 2.4 (c)). The temperature dependence for the dielectric constant is given in Figure 2.4 (d): Again, there are three phase transitions, indicated by the respective dielectric anomalies. The permittivity ε_r reaches its highest value of about 12,000 at the phase transition form the tetragonal to the cubic phase (ferroelectric to paraelectric phase).

Strontium Titanate

Strontium Titanate $SrTiO_3$ (STO) has a similar shaped unit cell compared to BTO except that here the Ba^{2+} ions are replaced by Sr^{2+} ions. Its electrical and structural properties, however,

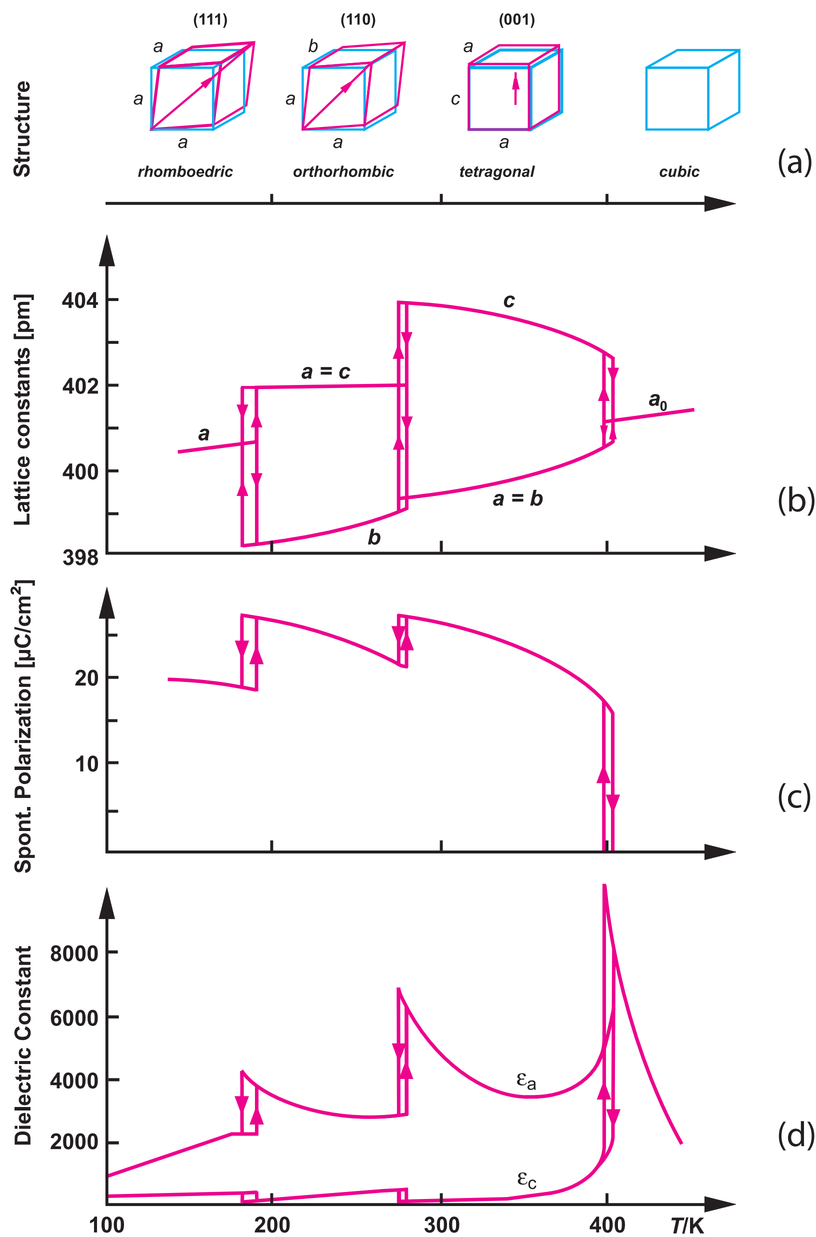

FIGURE 2.4:
Various properties of barium titanate as a function of temperature. [5]
(a) Structure
(b) Lattice constants
(c) Spontaneous polarization P_s
(d) Relative permittivity ε_r (also for fields in the direction of the c-axis)

differ from the BTO ones. In the temperature range from 0-300 K there is only one (structural) phase transition at about 110 K from the tetragonal to the cubic phase [55]. Nevertheless, the behavior of the dielectric permittivity ε_r (exactly said the dielectric susceptibility) in the corresponding temperature range does not show any evidence of ferroelectricity since there cannot

be found any decrease of ε_r below the structural phase transition temperature, as it is the case for BTO [56].

Barium-Strontium Titanate

$Ba_xSr_{1-x}TiO_3$ (BST) has become attractive due to its promising properties, i.e. high dielectric constant, for using it in high density dynamic random access memory (DRAM) [14,57,58] as well as tunable microwave devices like filters and phase shifters [59-61].

The material is a solid solution of $BaTiO_3$ and $SrTiO_3$, while the Ba/Sr-ratio of x/(1-x) strongly affects its physical properties. Its unit cell, again, has the typical perovskite shape, while on the A-sites an alternating occupation of Ba^{2+} and Sr^{2+} atoms according to x can be found. Mc-Quarrie [62] reported that the crystal phase at room-temperature is strongly affected by the fraction x and identified a room-temperature phase transition at about 0.7, which means 70% Ba^{2+} and 30% Sr^{2+}. In Figure 2.5 (a), the corresponding graph for the susceptibility χ_e depending on the temperature with the Ba/Sr-ratio as a parameter confirms this observation: For this certain ratio, χ_e (and also ε_r) shows its highest values near room temperature, which makes this composition most attractive for high dielectric constant applications.

Detailed studies for this BST composition ($Ba_{0.7}Sr_{0.3}TiO_3$) were performed by Hilton and Ricketts [64], who determined a maximum dielectric constant exceeding 5000 and a phase

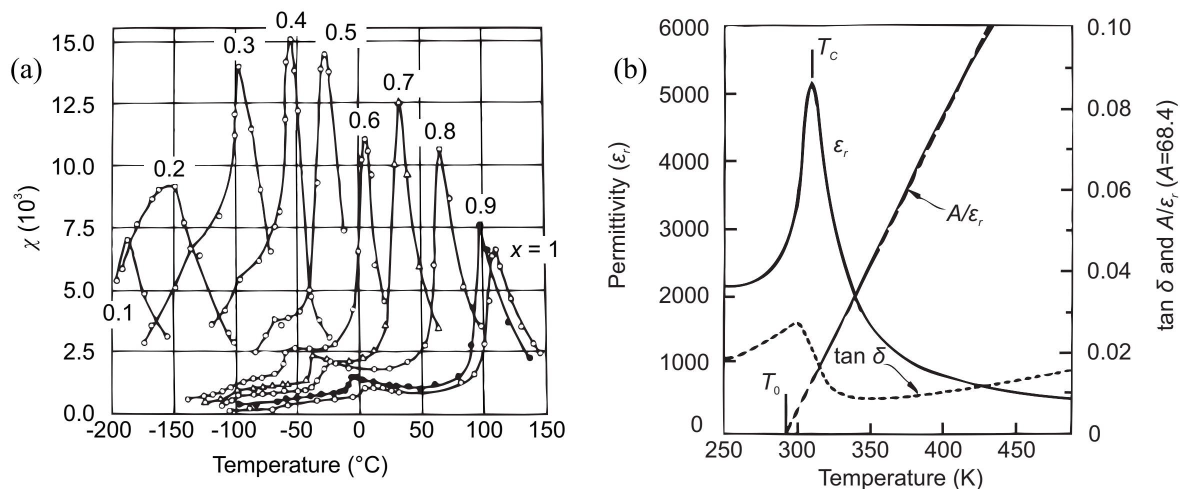

FIGURE 2.5:
(a) Dependence of the susceptibility of $Ba_xSr_{1-x}TiO_3$ on temperature for different x-values [63].
(b) Small signal permittivity versus temperature for $Ba_{0.7}Sr_{0.3}TiO_3$. Also shown are tan(δ) and the Curie plot ($1/\varepsilon_r$) [64].

transition temperature T_C = 310 K, as can be found in Figure 2.5 (b). Here, the difference between T_C and T_0 is about 20 K, indicating that bulk BST exhibits a first order phase transition.

Strontium Ruthenate as Electrode Material

For building a ferroelectric thin film capacitor, not only the used dielectrics BTO, STO and BST, but also the choice of suitable electrode material must be considered. Besides the widely used standard material Pt, here $SrRuO_3$ (SRO) has been chosen as an alternative electrode material. Similar to STO, SRO is an ABO_3 or perovskite-type material where the Ru^{4+} ions lie on the (central) B site. Its room temperature resistance (ρ_{SRO} = 340 µΩcm [65]) is rather high compared to the standard material Pt (ρ_{Pt} = 10.4 µΩcm [44]), nevertheless it is an excellent electrode for the (epitaxial) growth of BTO or BST due to its (pseudo-cubic) lattice constant of 3.93 Å, which is similar to BTO, STO or BST and results in low lattice mismatch [66,67]. Its work function is lower compared to the one for Pt (5.3 eV [68]) and can be determined to 4.6 - 5.0 eV, depending on the state of SRO oxidation [69].

Strontium Titanate as Substrate Material

From the above mentioned parameters such as the lattice constants of the used materials, an adequate substrate material can be derived. (100) STO single crystals that result in small lattice mismatch (with respect to BST or SRO) are commercially available in excellent quality and will be used in this work as sample substrates.

2.4 Mechanical Boundary Conditions

Instead of freestanding, thick layers, the samples used in this work incorporate rather thin films which are mostly grown epitaxially on much thicker substrates. The materials under investigation are thus subjected to mechanical boundary conditions, whose impact will be discussed in the following:

By interaction with the underlying substrate significant mechanical stresses can be generated inside the films. At the time of the film deposition, *growth stresses* may appear while the material is in its paraelectric phase. The specific amount of stress strongly depends on the parameters of the particular deposition process, i.e. the choice of the involved materials. It is known that in the growth process of thinner films (usually done in the paraelectric state) the deposited

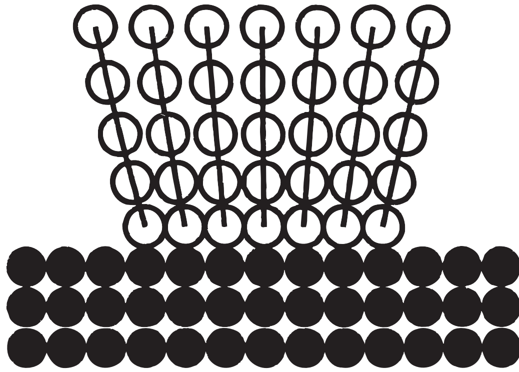

FIGURE 2.6:
Strain relaxation in pseudomorphic (dislocation free) films

material stays in its pseudomorphic cubic phase, which is accompanied by epitaxial strain, as shown in Figure 2.6 [70]. In the case of the deposition of thicker films, a significant stress relaxation occurs by the formation of misfit dislocations at the film/substrate boundary, as it is outlined in Figure 2.7 [71].

The strain that is induced by the substrate may cause lattice constants in the epitaxial films that differ strongly from those of the bulk material. To describe the substrate effects on the electrical properties of the film, a misfit-strain has been introduced in the theory. Dealing with perovskite films epitaxially grown on cubic substrates, a possible definition of this strain may be

$$S_m^0 = \frac{b - a_0}{a_0}, \tag{2.7}$$

where b describes the lattice substrate parameter and a_0 denotes the cubic cell constant of a free standing film [72]. Since this definition only holds for fully strained films, a modified

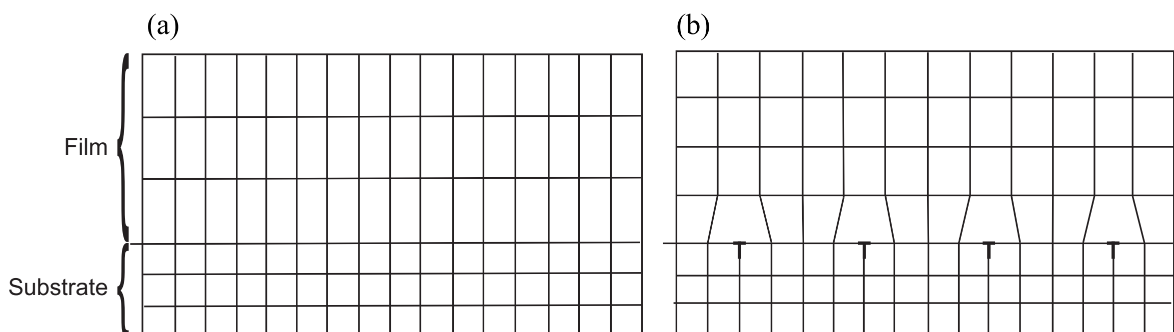

FIGURE 2.7:
Strain relaxation by introducing misfit dislocations for the example of two initially cubic materials.
(a) Since the (upper) film has a larger lattice constant than the (lower) substrate, the forced matching at the boundary results in a tetragonal distortion of the film.
(b) The strain from the distortion can be relaxed by introducing misfit dislocations so that the film regains its former cubic structure.

strain definition must be found. Due to the fact that above a critical thickness the incorporation of misfit dislocations is energetically favorable, the lattice strain becomes dependent on the film thickness [73]. When the density ρ of these dislocations is evaluated to $\rho \ll 1$, the actual misfit strain can be expressed as

$$S_m = \frac{b^* - a_0}{a_0} \tag{2.8}$$

with $b^* = b(1-\rho)$ as the effective lattice parameter of the substrate [71,74]. This reduced substrate lattice constant can be explained in the following way: Once a misfit dislocation array has developed at the film/substrate interface, the film no longer experiences the lattice parameter of the original substrate, but that of a substrate with an array of misfit dislocations.

Additional strains may arise from *thermal stresses* that develop inside the film due to different expansion coefficients of substrate and film. Here, we can neglect these contributions due to the fact that the used materials (BST, SRO and STO) all have similar thermal expansion coefficients.

2.5 Thermodynamics of Ferroelectrics

The thermodynamics of ferroelectric phase transitions can be described using a mean field theory: Here, the dipole as the thermodynamic entity is subject to the mean field of all other dipoles. Landau [78] and Ginzburg [79] expanded the thermodynamic potential near the phase transition temperature into a power series and introduced the polarization P as an **order parameter**, which for a second order phase transition diminishes continuously to zero at the phase transition T_C. This approach has been used by Devonshire to describe both ferroelectric and non-ferroelectric phases so that he could characterize the phase transition of $BaTiO_3$ (see chapter 2.3) [80].

From the first law of thermodynamics it is known that a change of the internal energy U (per unit volume) is given as

$$dU = dQ + dW, \tag{2.9}$$

where dQ means an infinitesimal portion of heat received by a unit volume of dielectric and dW is the work done on this volume (by electrical and mechanical forces) during the resulting quasi-static transformation. On the other hand it is known that dW can be expressed by

$$dW = \sigma_i dx_i + E_i dP_i, \tag{2.10}$$

defining the total work dependent on infinitesimal changes of strain x_i (to prevent confusion with the entropy density S, the strain S_i as defined in chapter 2.4 will be named x_i here) and electric polarization P_i in the presence of uniform stress σ_i and electric field E_i [40,43]. The second law of thermodynamics then gives

$$T \cdot dS \geq dQ, \tag{2.11}$$

with the absolute temperature T and the entropy density S. Besides, the equality sign in Eq. (2.11) is valid for a reversible process, while the inequality holds for an irreversible process. Using Eq. (2.9) and (2.10), Eq. (2.11) can be written as

$$dU \leq T \cdot dS + \sigma_i dx_i + E_i dP_i, \tag{2.12}$$

where the inequality sign in Eq. (2.12) again becomes an equality sign in the case of a reversible process. One obtains from Eq. (2.12)

$$T = (\partial U/\partial S)_{x,P,} \quad \sigma_i = (\partial U/\partial x_i)_{S,P,} \quad E_i = (\partial U/\partial P_i)_{S,x} \tag{2.13}$$

This means that when a system is described by independent variables S, x_i and P_i, the other variables can be found by first derivatives of the internal energy U. There are eight ways for describing a system by independent variables, chosen from the pairs (T, S), (σ, x) and (E, P) and therefore eight possible thermodynamic functions.

Mean Field Theory

One of the thermodynamic functions is the **free energy** F (Helmholtz Free Energy), which can be written near the phase transition temperature as a function of the order parameter P up to the sixth order:

$$F(P, T) = \frac{1}{2}g_2P^2 + \frac{1}{4}g_4P^4 + \frac{1}{6}g_6P^6 - PE \tag{2.14}$$

Here, the odd-powers of P do not occur in this expansion because of symmetry reasons. The coefficients g_2, g_4 and g_6 generally depend on the temperature, but as simple examples of first- and second-order ferroelectric phase transitions showed, g_4 and g_6 can be assumed to be temperature independent [40]. In particular, around the Curie-Weiss temperature T_0, the coefficient g_2 can be approximated to

$$g_2 = C^{-1}(T - T_0) \tag{2.15}$$

(cmp. above sub-chapter about the general temperature dependence).

In the following, the thermodynamic stable states will be determined in the case of zero electrical field ($E = 0$). Using the minima of the free energy, one yields

$$\frac{\partial F}{\partial P} = P(g_2 + g_4P^2 + g_6P^4) = 0, \tag{2.16}$$

$$\frac{\partial^2 F}{\partial P^2} = \chi^{-1} = g_2 + 3g_4P^2 + 5g_6P^4 > 0 \tag{2.17}$$

Equations (2.16) and (2.17) can be solved by $P = 0$ and $g_2 > 0$, which represents the paraelectric phase. There exist further solutions with $P = P_s \neq 0$, describing the ferroelectric phase.

Paraelectric Phase

In the paraelectric phase ($T > T_0$) P becomes zero, and by inserting Eq. (2.15) into Eq. (2.17), the susceptibility χ can be expressed according to a Curie-Weiss law with a critical exponent

$\gamma = 1$:

$$\chi(T) = \frac{C}{(T - T_0)} \propto (T - T_0)^{-\gamma}; \quad \gamma = 1 \tag{2.18}$$

Ferroelectric Phases: First Order Transition

Materials of this type of phase transition are characterized by the appearance of metastable phases, since a new phase has to nucleate out of an old one. Further characteristics of first order transitions are the sudden changes in the structure and volume of the material under investigation.

Considering the first derivative of the free energy (Eq. (2.16)) for $g_4 < 0$ and $g_6 > 0$, the thermodynamic stable states are given by $P = 0$ or

$$P_s^2 = \frac{|g_4| + \sqrt{g_4^2 - 4C^{-1}(T - T_0)g_6}}{2g_6} \tag{2.19}$$

In Figure 2.8 (a) the free energy as a function of polarization is depicted for different temperatures in case of a material with a first order phase transition. As it was already mentioned, the Curie-Weiss temperature T_0 is not equal to the phase transition temperature T_C. The following temperature regimes can be distinguished:

- $T \gg T_C$: stable paraelectric phase ($P = 0$)
- $T > T_C$: stable paraelectric phase, metastable ferroelectric phase ($\pm P_s \neq 0$)
- $T = T_C$: coexistence of paraelectric and ferroelectric phase
- $T_0 < T < T_C$: stable ferroelectric phase and metastable paraelectric phase
- $T < T_0$: stable ferroelectric phase

Somewhere during cooling from the regime where the stable ferroelectric phase coexists with the metastable paraelectric phase ($T_0 < T < T_C$), the first order phase transition will occur with a corresponding jump of the spontaneous polarization from zero to a finite value. Additional discontinuous changes in susceptibility χ and entropy S will be achieved using the known thermodynamic relations.

Ferroelectric Phases: Second Order Transition

Materials undergoing such a kind of phase transition are characterized by a continuos change in their structure and volume. Here, it will be sufficient to consider the polynomial expansion of the free energy (Eq. (2.14)) up to the fourth order and choosing $g_4 > 0$. From the derivative of Eq. (2.14)

$$\frac{\partial F}{\partial P} = P(C^{-1}(T - T_0) + g_4 P^2) \tag{2.20}$$

the solutions $P_s = 0$ and

$$P_s^2 = -\frac{(T - T_0)}{g_4 C} \tag{2.21}$$

can be found. At $T < T_C$, a spontaneous polarization exists. Here, the phase transition temperature T_C and the Curie-Weiss temperature T_0 are identical for the second order phase transition, while the critical exponent β for the order parameter is 1/2:

$$P_s \sim \left[\frac{1}{C g_4}\right]^{1/2} (T - T_C)^{1/2} \sim (T - T_C)^{\beta}; \quad \beta = \frac{1}{2} \tag{2.22}$$

Figure 2.8 (b) shows the free energy close to the second order phase transition as a function of the spontaneous polarization for different temperatures. At temperatures greater than or equal to the phase transition temperature $(T \geq T_C)$, a stable minimum can be found at $P_s = 0$, while decreasing the temperature below T_C will result in two minima of finite polarization value.

By inserting Eq. (2.15) and Eq. (2.22) into Eq. (2.17) (again neglecting the 6th order polarization term), the temperature dependence of the susceptibility below the phase transition temperature can be found as

$$\chi^{-1}\big|_{T < T_C} = 2\frac{T_C - T}{C}. \tag{2.23}$$

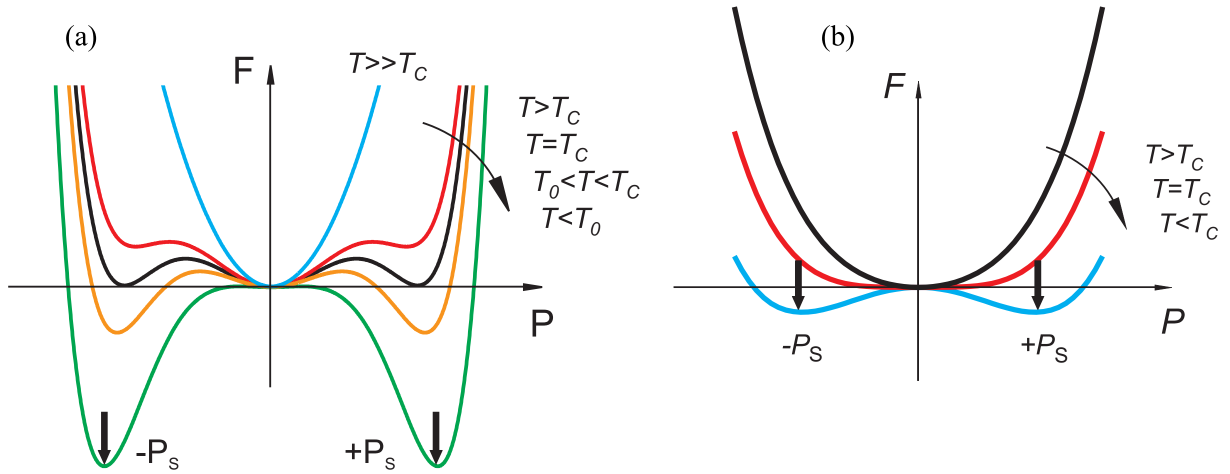

FIGURE 2.8:
Schematic presentation of the free energy as a function of polarization for ferroelectrics with (a) first order and (b) second order phase transition

It is remarkable that compared to Eq. (2.18), the pre-factor of the susceptibility changes at a phase transition by a factor of two.

Thermodynamics of epitaxial ferroelectrics

The **Gibbs free energy** G, as an additional thermodynamic potential is described by:

$$G = U - TS - X_i\sigma_i - E_iP_i \tag{2.24}$$

Pertsev et al. [75,76,81] developed a nonlinear thermodynamic theory to connect the Gibbs free energy with the mechanical boundary conditions and the electrical polarization and field, as described in the following:

In the case of a thin film grown epitaxially on a thick substrate, there will be no traction on the surface of the film such that σ_3, σ_4 and σ_5 must be zero (using the Voigt matrix notation). The in-plane lattice strains S_1, S_2 and S_6 (now using the old naming convention introduced in chapter 2.4, since no confusion with the entropy will occur anymore) of the film at the film/substrate interface are totally controlled by the substrate, which is assumed to be sufficiently thick. Since the minima of the standard elastic Gibbs function G (with polarization and stress used as independent variables) do not correspond to the equilibrium thermodynamic states (they are

associated with the equilibrium thermodynamic states at fixed stresses), the necessary thermodynamic potential is given by the following Legendre transformation of G:

$$\tilde{G} = G + S_1\sigma_1 + S_2\sigma_2 + S_6\sigma_6 \quad (2.25)$$

While this is a general expression for the thermodynamic potential of a thin ferroelectric film on a thick substrate, the here considered case of a (001) ferroelectric thin film epitaxially grown in a cubic paraelectric phase on a cubic (001) substrate results in $S_1 = S_2 = S_m$ (S_m according to Eq. (2.8)) and $S_6 = 0$.

Using the Landau-Ginsburg-Devonshire formalism from chapter 2.5, the modified Gibbs free energy $\tilde{G}$ was expanded into a power series of the polarization, with simplifications according to Ref. 82. Instead of a huge mathematical term expanding over several lines or more that includes all possible cases of polarization states and crystallographic orientations as it is shown in Ref. 83, here the result simply is

$$\tilde{G} = \frac{S_m^2}{s_{11} + s_{12}} + a_3^* P_3^2 + a_{33}^* P_3^4 + a_{111} P_3^6 - P_3 E_3. \quad (2.26)$$

In Eq. (2.26), simplifications have been included due to the fact that here only the particular case of thin films grown on compressive substrates will be considered. In this case, the film stabilizes below T_C in the out-of-plane polarization state $(P_1 = P_2 = 0, P_3 \neq 0)$, while the renormalized coefficients (as defined in this 2D-clamping case) are

$$a_3^* = a_1 - 2S_m Q_{12}/(s_{11} + s_{12}) \text{ and } a_{33}^* = a_{11} + Q_{12}^2/(s_{11} + s_{12}). \quad (2.27)$$

The parameters a_1, a_{11} and a_{111} are the dielectric stiffness and higher order stiffness coefficients at constant stress (a_1 is also known as the reciprocal dielectric susceptibility of the unpolarized crystal), s_{ln} are the film elastic compliances at constant polarization and Q_{ln} are the electrostrictive constants in polarization notation.

The phase transition temperature as a function of the lattice mismatch strain can be found by

setting $a_3^* = 0$ and with

$$a_1 = \frac{T - T_0}{2C\varepsilon_0} \tag{2.28}$$

(see Ref. 75) as

$$T(= T_C) = T_0 + S_m C \cdot 2\varepsilon_0 \frac{2Q_{12}}{s_{11} + s_{12}}. \tag{2.29}$$

The dependence of the dielectric susceptibility on the lattice strains has been extensively studied by Pertsev et al. [75-77]. They considered a thin film grown on a thicker substrate and found the reciprocal dielectric susceptibility $1/\chi_{el}$ (perpendicular to the film/substrate interface) to be linearly dependent on the misfit strain:

$$\frac{1}{\chi_{el}} = 2a_1(T) - \frac{4S_m Q_{12}}{s_{11} + s_{12}} \tag{2.30}$$

Here, s_{ln} are the film elastic compliances at constant polarization, Q_{ln} are the electrostrictive constants in polarization notation and a_1 is the dielectric stiffness of a bulk crystal linearly dependent on the temperature T. For describing the dielectric permittivity ε (which is almost the susceptibility) depending on the misfit strain, Eq. (2.30) leads to

$$\varepsilon = \frac{\varepsilon_0 K_s}{S_m - S_m^*}. \tag{2.31}$$

One realizes, that the dependence of the permittivity on the lattice strain in the film obeys a Curie-Weiss type law. Eq. (2.31) describes the conditions of a tetragonal thin film grown on a compressive substrate ($S_m < 0$) and is valid only at $S_m > S_m^*$. $K_s = -(s_{11} + s_{12})/(4\varepsilon_0 Q_{12}) > 0$ represents a material parameter equivalent to the Curie constant C and describes the sensitivity of the permittivity on the strain (in analogy to the sensitivity of the permittivity on the temperature from Eq. (2.18)). $S_m^*(T) = a_1(T)(s_{11} + s_{12})/(2Q_{12})$ displays a critical misfit strain at which the paraelectric phase loses its stability against the appearance of the out of plane polarization P_3 (in analogy to

the critical temperature T_0 from Eq. (2.18) above which the ferroelectricity disappears).

3 Thickness Dependence of Dielectric Properties in Ferroelectrics

Several authors reported a strong decrease of the dielectric constant with decreasing thickness of the BST thin films under investigation [13-18,84-92]. Figure 3.1 (a) shows a comparison between the temperature dependence of the dielectric constant of a ceramic BST sample and a 100 nm BST thin film: Whereas the dielectric value for ceramic samples shows a distinct peak (hence phase transition) at 310 K with a maximum value of approx. 20,000, the picture looks very different for the 100 nm BST thin film. Here, the maximum dielectric value is decreased to approx. 400, while the phase transition is strongly smeared with a hardly noticeable transition temperature $T_C \approx 180\,K$. The plot of the reciprocal dielectric constant $1/\varepsilon_r$ (Figure 3.1 (b)) shows that both samples obey the Curie-Weiss law above their phase transition with identical slopes, e.g. identical Curie constants. A more detailed analysis is given by Basceri et al. [15], where they analyzed the dielectric properties dependent of the film thickness, electric field and temperature. The analysis of the reciprocal capacitance density (@ zero bias) for different thicknesses reveals a linear dependence (Figure 3.2), as it was also reported by other groups [14-18,89-92]. This general behavior is often described by the so-called "dead-

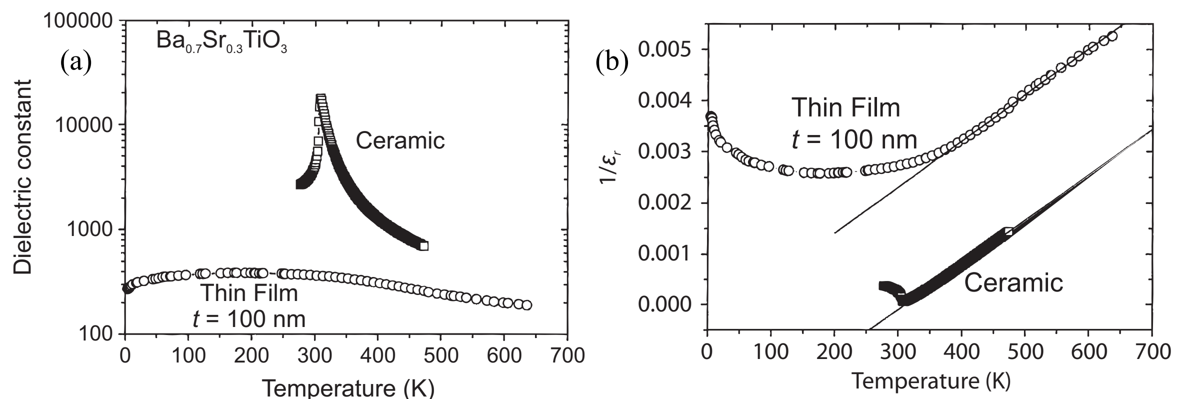

FIGURE 3.1:
Comparison of the temperature dependence of the dielectric properties of a BST ceramic and a thin film of the same composition [13]
(a) Dielectric constant, showing a more or less clear phase transition
(b) Reciprocal dielectric constant, obeying the Curie-Weiss law

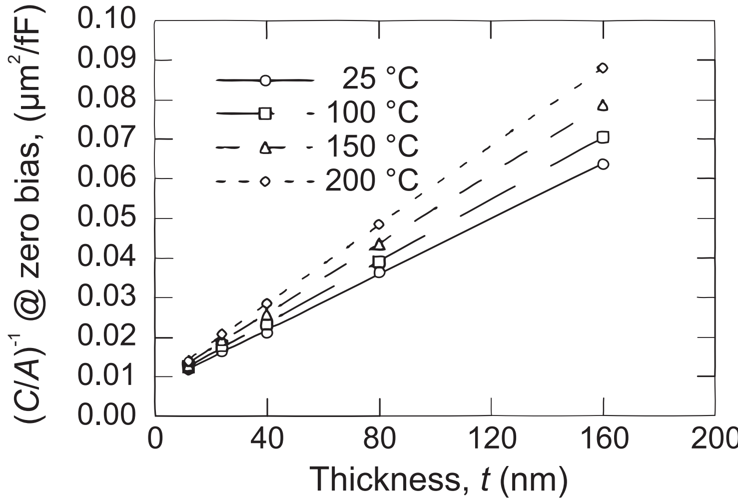

FIGURE 3.2: Reciprocal capacitance density (@ zero bias) as a function of BST film thickness at temperatures of 25, 100, 150, and 200 °C [15].

layer-model", which is schematically depicted in Figure 3.4: Here, an additional parasitic "interfacial capacitance" in the plate capacitor was introduced that hypothetically has a lower dielectric constant than the dielectric material under investigation. This small capacitive component acts electrically in series with the rest of the film, suppressing the dielectric constant in the whole system. Since a series connection of capacitive elements follows the rule $1/C = \sum_i 1/C_i$, the influence of the interfacial capacitance is maximized at the phase transition temperature, and less influential far away from T_C, thus automatically causing a peak-suppressing effect. The total thickness of the bulk dielectric layer with the permittivity ε_b is denoted by t and the thicknesses of the (two) dead layers with lowered permittivity ε_{i1} and ε_{i2} are t_{i1} and t_{i2}. Multiplied by the total capacitor area A, it can be expressed most easily by its reciprocal capacitance density $1/c_{eff}$:

$$\frac{A}{C_{eff}} = \frac{1}{c_{eff}} = \frac{t_i}{\varepsilon_0 \varepsilon_i} + \frac{t - t_i}{\varepsilon_0 \varepsilon_b} \approx \frac{1}{c_{i,\,total}} + \frac{1}{c_b} \tag{3.1}$$

Here, the two dead layers are combined into one single layer with thickness t_i and permittivity ε_i, resulting in the total interface capacitance density $1/c_{i,total}$. In general, it can be assumed that $t \gg t_i$, so that a linear equation in t results with a y-axis intercept $1/c_{i,total}$ and a slope equal to $1/(\varepsilon_0\varepsilon_b)$. From plots similar to Figure 3.2, one may now directly conclude to the quality of the electrode-dielectric-interface and also the dielectric constant of the pure (undisturbed) ferroelectric layer by means of the interface capacitance and the bulk-epsilon value. It should be mentioned that this dead layer has never been found yet physically by any means of micro-

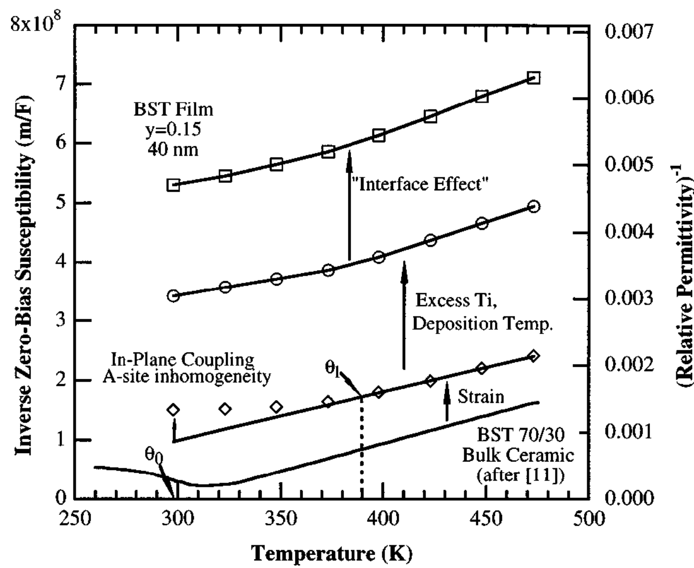

FIGURE 3.3:
Summary of contributions to the behavior of the temperature dependent (reciprocal) permittivity [89].

scopic investigations or chemical analyses. Nevertheless, it is a fairly good model to describe phenomenologically the permittivity decrease in ferroelectric thin film capacitors with decreasing thickness.

Figure 3.3 shows, how the authors of Ref. 89 attribute several possible influences on the decrease of the permittivity ε_r (shown here is the reciprocal permittivity $1/\varepsilon_r$ as a function of temperature T). In addition to the more precise terms of strain and non-stoichiometry (here: excess Ti), also a rather diffuse *interface effect* is mentioned, which seems to have a strong contribution on the permittivity decrease.

The whole issue has been very early discussed by Känzig [93], who supposed that a surface layer of 10 – 100 nm close to the bulk of $BaTiO_3$ crystals exists. He attributes the resulting surface strain to anionic or electronic space charge layers while in later investigations the thickness of this layer has been approximated to values between 10 and 1,000 nm ([94] and references therein). It is important to mention here that by measurements of thickness series as shown in Figure 3.4 it is only possible to determine the quotient of the thickness and the permittivity of the surface layer, t/ε_r (corresponding to the reciprocal capacitance density, A/C_{eff}). The separation of these strongly linked parameters is only possible under the assumption of a defined value of the dielectric constant of the layer. In early stages of the investigations thickness ranges of 1 µm for an assumed $\varepsilon_r = 200$, and 100 nm for an assumed $\varepsilon_r = 5$ were reported. By reaching higher degrees of technical development, the deposition of films in

the range of the assumed thickness of the surface layer could be realized, while these specimens still had high dielectric constants, so the value of t/ε_r was changed, but in general the idea of a surface layer remains valid.

The interface capacitance density has been investigated in the case of BST deposited using the method of chemical solution deposition (CSD) on platinized Si wafers by Ellerkmann et al. [95]. Using a modified approach of the LGD-theory, it was found that the interface capacitance does not show any dependence on the applied bias voltage. Together with the fact of a thickness independent permittivity at high applied electric fields, this allowed to explain the strong suppression of the tunability for thin BST films. As a result, the thickness and permittivity of the assumed interface layer had been estimated as $t_i = 20$ nm and $\varepsilon_i = 100$. While these values have to be discussed extremely carefully (especially the very thick interface layer, t_i), it must be stressed that in the conclusion some simplifications could be done that will not hold in every case. These include the absence of a spontaneous polarization at room temperature and a non-epitaxial nature of the films under investigation.

Accompanied by the decrease of the permittivity, several authors reported a shift of the phase transition temperature T_C depending on the thickness of the ferroelectric layer in the capacitor [17,92,96,97]. In general, T_C seems to deviate from the bulk values when dealing with thin films in the thickness range below 600 nm. While in some publications a decrease of the phase transition temperature with decreasing thickness of the dielectric has been reported [17,96], others found that the phase transition temperature increases with decreasing film thickness [97]. Depending on the involved electrode material, both of the above mentioned cases have been found in very similar BST capacitors [92].

In the following, possible physical explanations for the dielectric deterioration in thin ferroelectric films will be listed according to a classification in the two groups “intrinsic” and “extrinsic” influences.

3.1 Extrinsic Influences

Crystalline Imperfections

There exists a variety of crystal defects that may cause thickness dependences in the ferroelec-

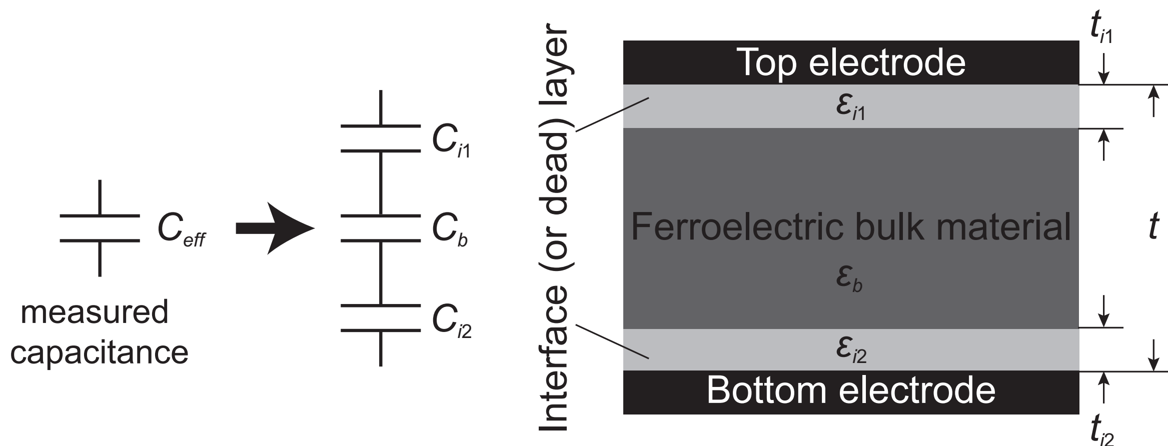

FIGURE 3.4:
Simplified sketch of the "dead layer" model.

tric properties as mentioned above [98,99]. A major cause for the formation of dislocations in ferroelectric thin films and hence the decrease of the ferroelectric properties can be found in the misfit across the interface between an epitaxial film and its underlying substrate [58,71,73,99]. As long as this misfit is small enough, it will be accommodated by uniform elastic strain until a critical film thickness is reached. Films above this critical thickness (in the order of 5 – 15 nm) relax from their strain by introducing dislocations that will deteriorate their functionality.

It is also well known that grain boundaries and grain sizes have a strong impact on the permittivity in ferroelectric thin films. Waser collected reports which showed for BTO with decreasing grain sizes an increase of the permittivity up to a maximum at around 700 nm [88]. Below this grain size, the permittivity decreased again.

To eliminate grain-size effects, several groups have investigated single-crystalline BST films [21,36,37,100,101]. The highest measured dielectric constant of these films is around 1,000 [100]. Depending on the film quality, BST films may show the paraelectric to ferroelectric phase transition, but much broader than that in a bulk material. A more consequential way to get rid of *all* defect- and grain boundary – based phenomena was chosen by Saad et al. [102] who prepared "free-standing" single crystal BTO capacitors with the focused ion beam (FIB) technique down to thicknesses of 75 nm. They observed maximum dielectric constants exceeding 25,000 and a ferroelectric phase transition at about 395 K as well as a Curie-Weiss-temper-

ature of about 377 K that usually can be seen only in single crystal bulk ceramics. These findings were regarded as a full recovery of bulk-like functional behavior for ferroelectrics in the sub-100 nm thickness regime, as no one has seen before.

Local Diffusion of Electrode Material into the Ferroelectric Film

The dependence of ionic interdiffusion on the ferroelectric properties of thin BST films was investigated by several groups. Tsai et al. found that BST thin films on Ru bottom electrodes showed a decreased dielectric constant from 548 down to 325 after annealing in O_2 at 700 °C, while the same films on Ru/RuO_2 bottom electrodes had an increased dielectric constant from 322 to 433 after a similar annealing treatment [103]. They assume that the BST films on Ru/ RuO_2 behave more stable while on Ru, a possible thin interfacial layer like (Ba, Sr)(Ru, Ti)O_3 might have been formed by the interdiffusion of ions after annealing, caused by the similarity of the ionic radii of Ru and Ti. The approach of Choi et al. was to use (Ba, Sr)RuO_3 (BSR) as the electrode material, where they found a strong dependence of the dielectric constant on the (Ba, Sr)/Ru ratio in the BSR electrodes with the highest values at about 550 for a stoichiometric ratio of 1.0 and lower values at 470 and 350 for ratios of 1.3 and 0.7 respectively [23]. They assume a diffusion of the shared elements Ba and Sr in either direction between stoichiometric BST and Ru-rich or Ru-deficient BSR, leading to the formation of a low dielectric interface layer. This diffusion may be suppressed in the case of stoichiometric BSR due to equal driving forces.

3.2 Intrinsic Influences

Built-In Electric Fields

The temperature dependence of the permittivity in BST has been investigated by Vendik et al. [104]. They consider perfect single crystals of BST (no defects) which are free of built-in electric fields and internal mechanical strains, where the position of the maximum permittivity coincides with the phase transition temperature. Since such a perfect crystal is not available when dealing with thin film capacitors, one has always to account for built-in fields from work-function differences of the used electrode materials, which following their calculations cause a shift of the maximum permittivity towards higher temperatures and a decrease of the permittivity in general. Other sources for internal built-in fields are mentioned by Tagantsev et. al., who iden-

tified depletion layers at the electrodes to be the reason for a reduction of the effective dielectric permittivity of the film [105].

Lattice Strains

The mechanical boundary conditions at the electrode/ferroelectric interface, as introduced in chapter 2.4, not only have an extrinsic effect when they lead to the generation of misfit dislocations (cmp. chapter 3.1), but also affect intrinsic size effects. In fact, the lattice strain can also affect the stability of the ferroelectric phase and impact the equilibrium domain structures. In Ref. 91, using a thermodynamic theory the decrease of the permittivity has been explained by the thickness dependent strain relaxation in epitaxial ferroelectric thin films, which leads to a thickness dependence of the reciprocal capacitance density in analogy to Eq. 3.1.

Finite Screening Abilities of the Electrode Material

The reduction of the applied field inside the ferroelectric film due to a finite screening length of the electrodes was first mentioned 1961 by Mead [106]. He reported measurements of the reciprocal capacitance density vs. film thickness for Ta-TaO_2 capacitors that resulted in plots similar to those in Figure 3.2 and attributed this thickness dependence to electric field penetration into the (metal) electrode, while he assumed the penetration depth to be approx. 1 Å. Theoretical studies from Ku and Ullman showed a good agreement with Mead´s investigation [30]. By using the Debye-length *L,* defined by

$$1/L^2 = 2n_0e^2/\varepsilon_m\varepsilon_0E_F, \tag{3.2}$$

with specific parameters of the electrode material such as its Fermi energy E_F, its dielectric constant ε_m and its free electron density n_0 they found a description of the reciprocal capacitance density similar to that given by Eq. (3.1):

$$\frac{1}{c} = \frac{t}{\varepsilon_0\varepsilon_r} + 2.3\frac{L}{\varepsilon_0\varepsilon_m} \tag{3.3}$$

Again, the reciprocal capacitance density consists of one thickness dependent part from the pure dielectric behavior plus one thickness independent part (intercept) governed by the characteristic length *L* multiplied by 2.3. The characteristic penetration length *L* has been corrected

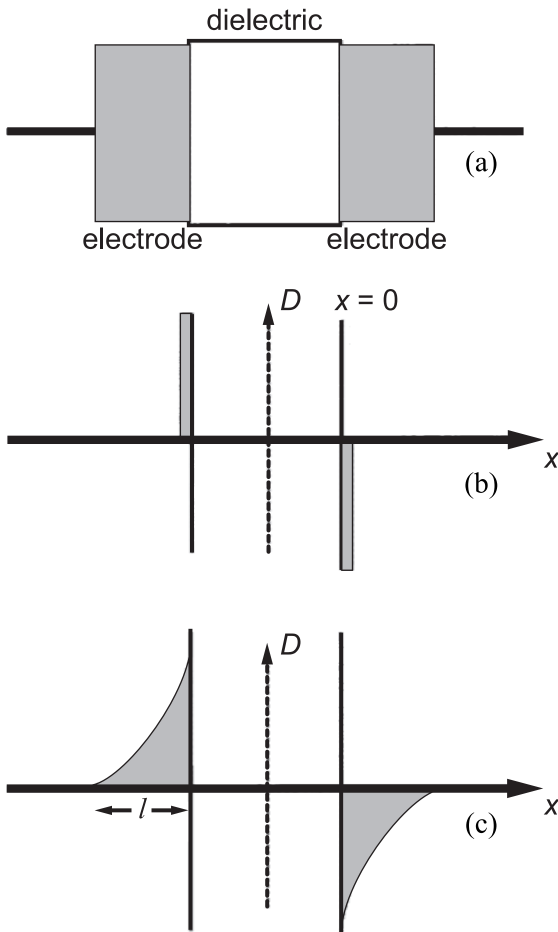

FIGURE 3.5:
(a) Schematic of a metal-dielectric-metal thin film capacitor. (b) In the simplest approximation, screening charges in the electrodes build up in an infinitely-thin plane at the electrode/dielectric interface. (c) A more realistic model acknowledges that the screening charge occupies a finite spatial extent (*l*) [31].

later by Simmons to r_0,

$$r_0 = 2L/\sqrt{3} \tag{3.4}$$

who found an analytical expression rather than the numerical values from Ku and Ullman [107].

Finally, an application of the electric field penetration towards high-dielectric constant perovskites was performed by Black and Welser [31]. They considered an exponential distribution of the screening charges inside the electrodes rather than a screening charge plane of zero thickness, as it is assumed in the conventional case of linear capacitors (Figure 3.5). They calculated

the characteristic screening length l by means of the Thomas-Fermi method as follows:

$$l^2 = \varepsilon_m \frac{2}{3}\frac{\varepsilon_0 E_F}{\rho_0 e} = \varepsilon_m {l_{TF}}^2 \tag{3.5}$$

Here, one finds again Fermi energy E_F and dielectric constant ε_m of the electrode material, while ρ_0 denotes the induced charge density at position $x = 0$ and l_{TF} is typically defined as the Thomas-Fermi screening length. Now the resulting reciprocal capacitance density can be calculated as

$$\frac{1}{c_{eff}} = \frac{1}{\varepsilon_0}\left[\frac{t}{\varepsilon_r} + \frac{2l_{TF}}{\sqrt{\varepsilon_m}}\right] = \frac{1}{c_{dielectric}} + \frac{1}{c_{interface}} \tag{3.6}$$

Again, this results in an equation describing $1/c_{eff}$ linear dependent on t with a y-axis intercept resulting from the interface capacitance. Hence, one can now calculate maximum values of the interface capacitance when l_{TF} and ε_m are known. It should be noted that these values, depending on the accuracy of the used electrode parameters, seem to display limits of the interface capacitance density *regardless* of the used dielectric material or thickness of the dielectric layer. The value of the electrode permittivity ε_m in the case of SRO is under controversial discussion in the literature: While Black and Welser suggest a speculative value of ~100, Kim et al. have calculated the SRO permittivity by means of optical measurements to a more realistic value of ~8.45 [108]. In contrast, Dawber et al. neglect the SRO permittivity by simply setting this value to 1 [32,109].

From publications of Batra et al. an influence of the so called depolarizing field E_{dep} on the phase transition temperature in ferroelectric thin films can be observed [110-112]. This field may occur when the polarization charges $\rho = -\mathrm{div}P$ are not perfectly compensated by free charges. Such compensation charges can reside either internally (in the ferroelectric) or externally (in the electrodes). Since the conductivity of the ferroelectric is generally rather low (several orders of magnitude smaller) compared to the electrode material, one assumes that for most cases of interest the polarization will be compensated externally. In thin films however, such a charge compensation cannot be done completely, resulting in a residual field that may modify the phase stability of ferroelectric films with sufficiently low thickness. With these ob-

servations, a decreasing phase transition temperature with decreasing film thickness could be found.

To determine the magnitude of the depolarizing field, the considerations of Mehta et al. can be used [113]. They found a strong dependence of the retention behavior in $Pb_{0.92}Bi_{0.07}La_{0.01}(Fe_{0.405}Nb_{0.325}Zr_{0.27})O_3$ on the film thickness and attribute this to depolarizing fields existing inside the ferroelectric. Assuming a charge distribution similar to what has been found by Black and Welser [31], and by solving Poisson's equation, the depolarizing field E_{dep} was calculated to

$$E_{dep} = -\frac{P}{\varepsilon_0 \varepsilon_r}\left[\frac{2\varepsilon_r/l}{2\varepsilon_r/l + \varepsilon_m/l_s}\right], \tag{3.7}$$

where they use the dielectric constant of the electrode ε_m again, while l_s means the screening length in the electrodes and P, l and ε_r denote the polarization, thickness and dielectric constant of the ferroelectric layer. By applying voltage pulses on the capacitor, they measured the time dependence on the retention loss and found that different polarities of the applied pulses result in different polarization retention decay. They attributed this to contact potential differences and could improve the retention behavior by applying additional external voltages compensating these differences.

Großmann has shown a way to connect the interface capacitance with the polarization and the depolarizing field by using the model of a short-circuited capacitor with the two possible dead layers combined into one single interface layer, as shown in Figure 3.6 [114]. With Maxwells equation

$$\oint \vec{E} d\vec{s} = 0 \tag{3.8}$$

and the continuity condition at the ferroelectric/electrode interface $D_i = D_b$ as well as the explicit expression of the screening in the ferroelectric ($E_b = -E_{dep}$)

$$D_b = P + \varepsilon_0 \varepsilon_b E_b \tag{3.9}$$

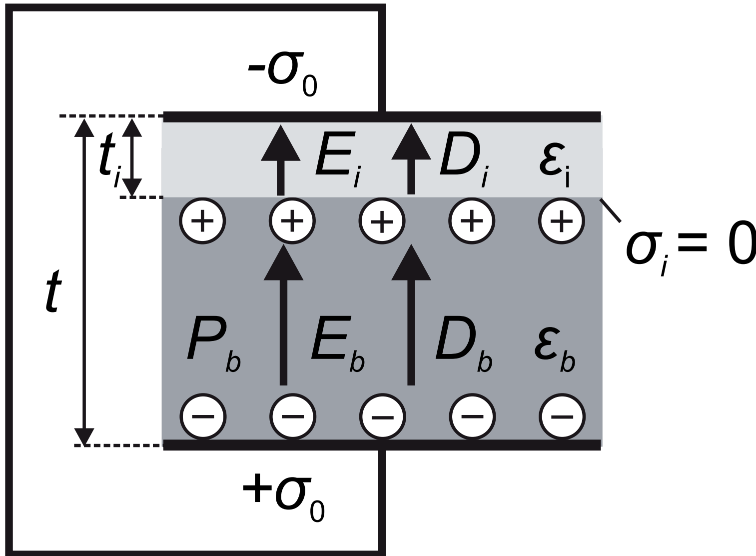

FIGURE 3.6:
Model structure of the ferroelectric capacitor with one thin interface layer and the corresponding fields, permittivities and polarization.

the resulting depolarizing field can be evaluated to

$$E_{dep} = -P\frac{1}{c_i + c_b} \cdot \frac{1}{t}. \tag{3.10}$$

Here, c_i and c_b are the interface and bulk capacitance densities. Since the thickness of the interface layer t_i can be assumed to be much smaller than the total thickness of the capacitor t, the second part of the denominator in Eq. 3.10 is often neglected [39], so that E_{dep} may be expressed as

$$E_{dep} \approx -\frac{P}{c_i \cdot t}. \tag{3.11}$$

Both Eq. 3.10 and Eq. 3.11 show a linear dependence of the depolarizing field E_{dep} on the electrical polarization P.

A method for direct measurements of the depolarizing field incorporating the voltage pulses introduced in Ref. 113 was suggested by Kim et al. [108]. They used SRO/BTO/SRO capacitors on STO substrates and observed a slow-down of the polarization retention loss, which they attributed to a (complete) compensation of the depolarizing fields. The values for E_{dep} derived in this procedure were shown to be in a similar range as those calculated with Eq. (3.7) using

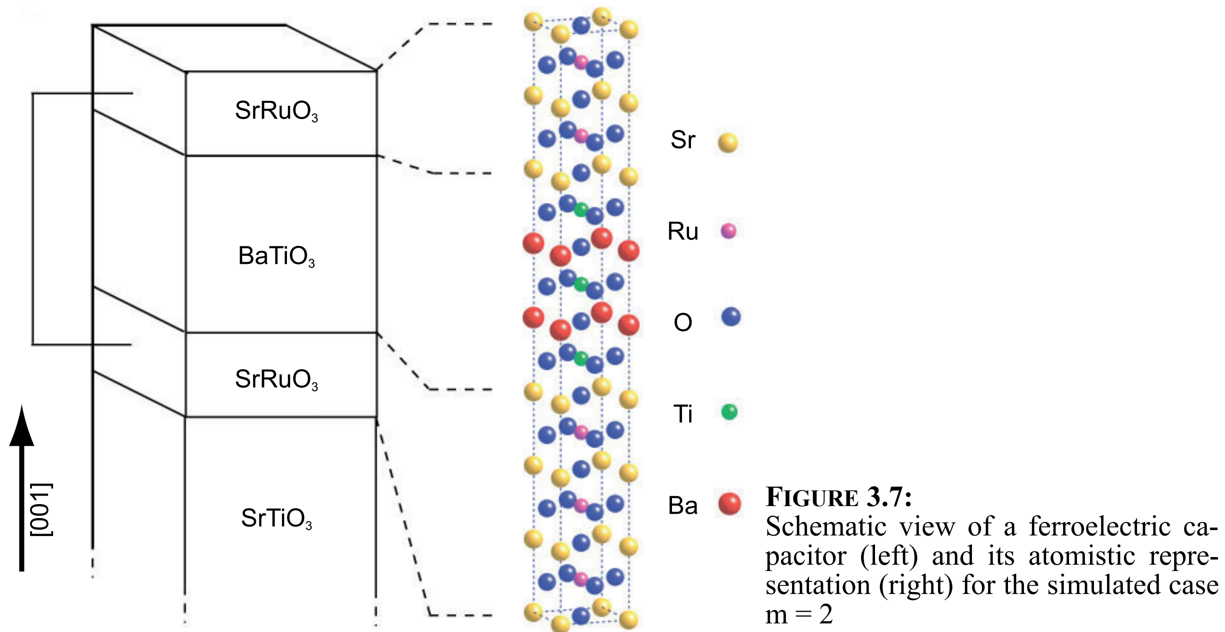

FIGURE 3.7: Schematic view of a ferroelectric capacitor (left) and its atomistic representation (right) for the simulated case m = 2

dielectric values calculated by optical spectroscopy of the SRO electrodes. In a publication of Bratkovsky and Levanyuk, however, it is strongly questioned wether this applied bias is related to the depolarizing field at all [115].

Ab-initio calculations of SRO/BTO/SRO capacitors epitaxially grown on STO were performed by Junquera and Ghosez [34]. They discussed the system depicted in Figure 3.7 under short circuit conditions. The basic unit, periodically repeated in space, corresponds to the general formula $[SrO\text{-}(RuO_2\text{-}SrO)_n/TiO_2\text{-}(BaO\text{-}TiO_2)_m]$ with $n = 5$ and m ranging from two to ten, thus controlling the thickness of the electrodes and dielectric layer. From first principle considerations of the internal energy and electrostatic arguments the existence of the depolarizing field in thin ferroelectric films could be validated, which, as will become clear later in this work, have a direct influence on the phase transition temperature of the investigated thin film capacitors.

Soft Mode Hardening

Changes of the lattice dynamical properties of perovskites have been studied extensively by Sirenko et al. [19]. They attribute the reduction of the dielectric constant in $SrTiO_3$ thin films to the hardening of the lowest optical phonon mode, which is also named the soft mode. They measured the effective dielectric constant as real and imaginary parts as a function of the

wavenumber (cm^{-1}) at various temperatures. From these measurements, the eigenfrequencies of the soft mode optical phonons were evaluated. As it is known from Ref. 116, this eigenfrequency, measured at bulk ceramics, should decrease with decreasing temperatures until it reaches approx. zero at a critical temperature. The experiments in Ref. 19 however showed a reduced softening of the soft mode depending on the temperature, e.g. the frequency of the soft mode phonon does not reach zero but saturates at finite frequency values. In contrast, the eigenfrequencies of all other longitudinal and transversal optical phonon modes will be only slightly affected by variations of the temperature and do not differ from those of the bulk STO. The comparison of the inverse of the static dielectric constant and the soft mode as a function of temperature showed a good agreement, as it was previously predicted by theoretical values of the Lyddane-Sachs-Teller (LST) relation.

In a Ref. 33, a correlation between the dead layer and the hardening of the $SrTiO_3$ soft mode could be established. With first principles calculations for SRO/STO/SRO heterostructures a macroscopically averaged local permittivity profile has been achieved. From the corresponding electrostatic potential, a direct conclusion on the depolarizing field E_{dep} was made, which the authors think is the main cause of both the interfacial dead layer and the soft-mode hardening. They found from their analysis that excellent screening properties at the interface are important, since even one or two sub-polarized atomic monolayers would seriously affect the properties of micrometer-thick devices (and of course thinner film thickness).

To summarize this chapter, the following should be noted: The simplest model assuming low permittivity layers at the electrodes/ferroelectric interfaces reveals a widely accepted equation for the calculation of the reciprocal capacitance density linearly dependent on the film thickness (Eq. 3.1). As will be shown later, some of the intrinsic and extrinsic effects lead to similar representations of the capacitance density with a variation of the basic equation due to the particular physical effect, so that additional terms are added that include the dependence of mechanical strains or depolarizing field.

4 Experimental Methods

The first part of this chapter gives the details about the preparation of the ferroelectric capacitors used in the investigations of this work. In the second part, the different methods and techniques of electrical characterization are described.

4.1 Sample Preparation

Numerous methods for the deposition of ceramic thin films have been developed in the last decades. Choosing the right method is not easy and always depends on the specific material to be grown on a certain substrate to fulfill a certain purpose. The deposition techniques can be classified into either physical or chemical deposition methods [5,117,118]. The physical methods are characterized by a well defined particle source (target) and generally a free flight (in vacuum) to the substrate. In chemical methods, so-called precursor solutions containing the desired materials dissociate at the hot substrate surface and release the atoms of interest.

Since in this work solely physical deposition methods were used, a detailed description of the chemical methods will be omitted.

In the following, a description of the deposition techniques used in this work will be given. The BST and SRO thin films were deposited by pulsed laser deposition while the Pt electrodes were fabricated by sputtering.

Pulsed Laser Deposition of perovskite thin films

A comprehensive description of all details of the pulsed laser deposition (PLD) technique can be found in Ref. 120, therefore this introduction will be rather brief to explain only the essential parts of this method. The working principle of the PLD technique is displayed in Figure 4.1 (a). A short pulsed laser beam from an excimer laser[4] is focused on a rotating target containing the materials to be deposited in a stoichiometric composition. In the deposition chamber an ambient gas pressure (usually O_2) of 0.3 to 1 mbar is maintained, so that these pulses with an energy of typically 2 – 5 J/pulse lead to the immediate formation of a plasma at the target surface, containing energetic neutral atoms, ions and molecules. This so-called

4. Here, a KrF excimer laser with a wavelength of 248 nm and a repetition rate between 5 and 10 Hz was used

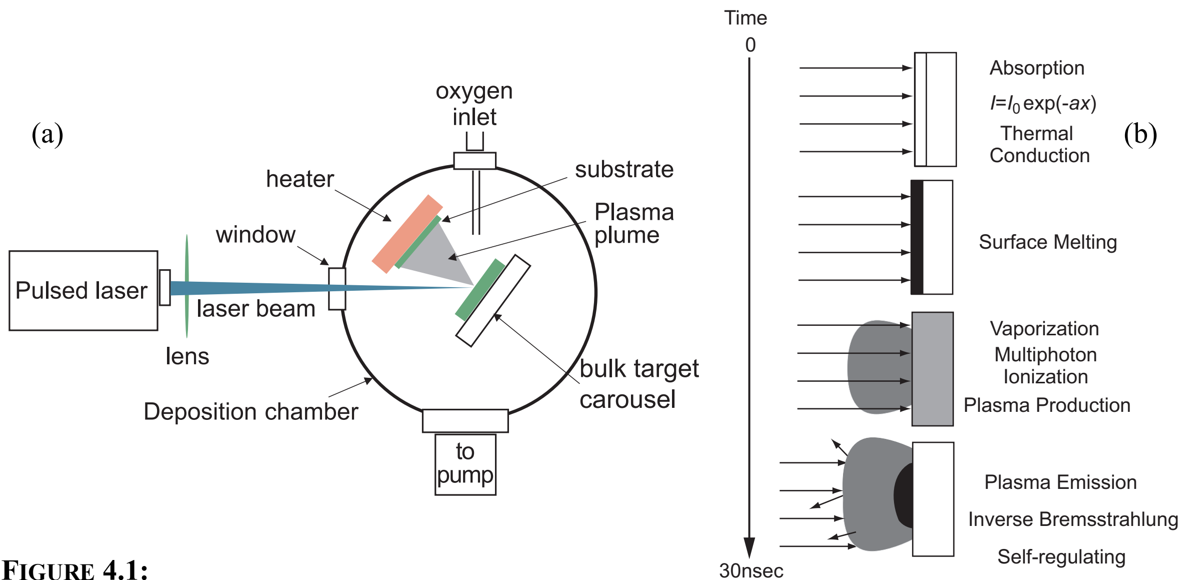

FIGURE 4.1:
Working principle of the pulsed laser deposition (PLD) [5]
(a) Simplified setup of a PLD system for the deposition of oxide thin films
(b) Time evolution of the plasma plume that develops at the surface of the target

"plume" reaches the substrate surface with a broad energy distribution of 0.1 to > 10 eV. A chronological resolution of the evolution of the plume can be found in Figure 4.1 (b).

Using PLD, numerous different material systems could be successfully deposited, amongst others also thin films of perovskite ceramics such as BTO and STO [119], BST [121] or SRO [122]. In the course of this work, the involved parameters had to be optimized to achieve the successful deposition of high-quality single crystalline thin films. The parameters used for the deposition of the films investigated here can be summarized as follows:

- $p_{O_2} = 0.25$ mbar (oxygen partial pressure)
- $T_g = 700°$ C (growth Temperature at the STO substrate)
- oxygen flow rate: 144.5 mln/min
- laser repetition rate: 5 – 10 Hz
- Laser energy density: 5 J/cm^2
- deposition rate: 10 – 20 nm/min.

For substrate purposes, commercially available STO single crystals ((100) orientation, manufacturer: Crystec GmbH) with an area of 1 x 1 cm^2 and a thickness of about 1 mm were used.

In an *in-situ*[5] process, first the bottom electrodes were deposited, resulting in SRO layers of about 100 nm thickness. Prior to this deposition, the substrate was heated up to the desired process temperature, after which the ambient O_2 pressure has been adjusted to a constant pressure. To get a “clean” atmosphere in the process chamber, the pump exhausted the “used” oxygen, while fresh oxygen has been let in, thus resulting in stable flow-rates and oxygen pressures. After setting up the chamber parameters according to the desired values, the laser has been switched on with a suitable repetition frequency. For the next layer to be deposited, the SRO target has been replaced by turning the target carousel and positioning the BST target into the laser beam without breaking the low vacuum, thus allowing an in-situ deposition of the thin films of interest. The film thicknesses deposited in this second step range from about 10 nm up to about 300 nm. Depending on the certain concept, a third deposition step has been performed. Here, top electrodes with thickness of about 30 nm were deposited in a subsequent in-situ deposition step after changing the target back to SRO at the same temperature and pressure as the BST films before.

Top Electrode Structuring

Besides the aforementioned deposition of the perovskite materials via PLD, additional samples were prepared with top electrodes of Pt deposited *ex-situ* in a dc-sputtering system. The Pt as well as the SRO top electrodes had to be structured to finally form a plate capacitor configuration with a suitable geometry ratio. In principle, this structuring could be done using a *lift-off* process [5] or by means of a *dry etching* step. For the Pt case, it has been experimentally observed that a treatment of the BST surface with chemicals such as the developer and photoresist in the lift-off process *prior* to the deposition of Pt leads to a significant deterioration of the dielectric properties of the thin film capacitors. In case of SRO top electrodes, the photoresist would not withstand the high temperatures necessary for the PLD process. Therefore, a dry etching process had been used for defining both the Pt and SRO top contacts, which by the way makes it easier to compare the two different material systems.

Here, photoresist (AZ5214) has been spun on the top electrode layer and has been prebaked, thus establishing a so called *positive tone* process. The thus prepared photoresist was then ex-

5. Different processing steps are performed in series without changing the reaction chamber (here: PLD chamber) and without breaking the process atmosphere (vacuum)

posed by means of a photolithographic mask and UV-light. A succeeding developer bath removed the photoresist which had been exposed to the UV-light, while the unexposed area defining the top electrode contacts remained on the top layer. In a final processing step, the thus pre-structured samples have been dry-etched in an Ar-plasma RIBE (reactive ion beam etching; Oxford Instruments Ionfab 300). Using this process, top electrode contacts with 5 x 5 μm^2 up to 200 x 200 μm^2 could be achieved, which together with BST thicknesses of max. 200 nm result in stray-field-free capacitors.

In the following, the system $SrRuO_3/Ba_{0.7}Sr_{0.3}TiO_3/SrRuO_3$ will be termed as *SRO samples* and correspondingly the system $SrRuO_3/Ba_{0.7}Sr_{0.3}TiO_3/Pt$ as *Pt samples*.

4.2 Electrical Characterization Methods

In this sub-chapter, the methods for electrical characterization of the ferroelectric thin film capacitors will be described. A measurement setup was available which allowed the samples to be investigated at different temperatures. This system (Cascade Microtech thermal probe station 9600) comes along with an available temperature range from -65 °C up to 200 °C, using a compressor stage and methanol as the cooling medium in a closed circuit. The system is equipped with two micro-manipulators controlling the needles to contact the device under test and a microscope to magnify the contact area. It is possible to make the necessary electrical connections using the provided BNC connectors to ensure proper shielding of the signals.

The measurement of the different electrical properties was done using equipment such as:

- Impedance analyzer (HP 4194A)
- aixACCT TF analyzer 2000

These instruments are partly equipped with IEEE488 interfaces, so a computer controlled programming of the measurements could be performed using National Instruments LabVIEW as the programming tool.

4.2.1 Small Signal Measurements

One key characterization parameter of ferroelectric materials is their permittivity ε_r. In the early years, it was enough information to know the permittivity for the case of zero field,

$E = 0$, since most applications for ferroelectric materials used only their small signal properties. Nowadays, more and more large signal applications (such as tunable filters etc.) became interesting, so that the polarization dependence of the permittivity had to be investigated. This is most easily characterized by a so-called “capacitance-voltage curve” (C-V curve). The capacitance, which yields the permittivity as can be seen from the well known plate capacitor formula

$$C = \varepsilon_0 \varepsilon_r \frac{A}{t}, \tag{4.1}$$

was measured using an impedance analyzer.

Therefore, one applies an alternating voltage on the device under test and measures the resulting current as well as the phase shift between current and voltage. With these values, the (complex) impedance can be determined, which can be easily transformed into capacitance and loss tangent or whatever parameter one is interested in. The impedance analyzer used here allows to apply alternating voltages with a measurement frequency f_{ac} from 100 Hz up to 15 MHz, while the amplitude of the small signal voltage V_{AC} can be varied from 10 mV up to 1 V. An additional DC voltage bias can be superimposed on the small signal measuring signal, where V_{DC} ranges from -40 V up to 40 V [123]. This allows the measuring of the permittivity at different polarization states, corresponding to different points on the hysteresis loop. The instrument can automatically perform complete dc-voltage sweeps, resulting in C-V curves with

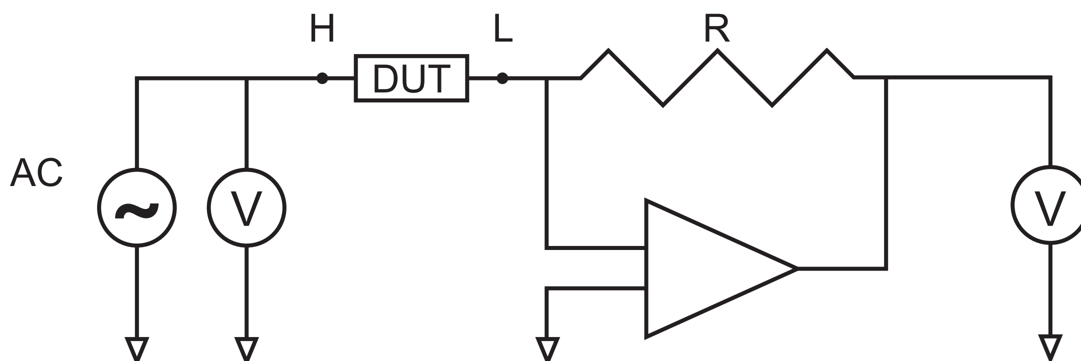

FIGURE 4.2:
Auto balancing bridge method: Currents flowing through the DUT also flow through resistor R. The potential at the “L” (low) point is maintained at zero volts (thus called “virtual ground”), because the current through R balances with the DUT current by operation of the I-V converter amplifier. The DUT impedance is calculated using voltage measurements at the “H” point (high) and across R (from [124]).

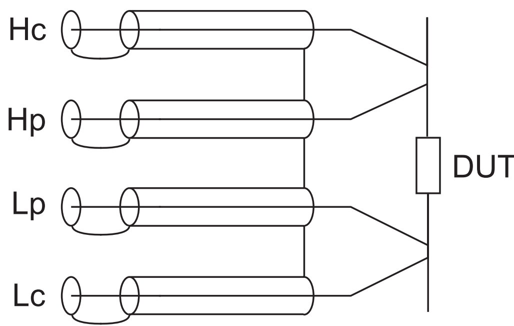

FIGURE 4.3:
Connection diagram of a four terminal pair (4TP) configuration of the measurement cables [124].

predefined start- and stop bias values and a user-defined bias-voltage step. The resulting large signal frequency is quite low, depending on the signal enhancement methods (averaging, integration) one achieves rates of ~100 mHz. A very simplified functional diagram of the used type of impedance analyzer is given in Figure 4.2. For accurate measurements of a device impedance, it is important to know the influence of any cabling or contact needle issue. Most instruments are equipped with integrated compensation functions that allow to reduce these disturbances. Proper use of the short and open compensation modes in advance to the actual impedance measurement together with a four terminal pair configuration of the connecting cables according to Figure 4.3 lead to a significant improvement in measuring accuracy [124].

4.2.2 Hysteresis Measurements

Measuring the polarization in ferroelectric materials is always connected with some kind of hysteresis curve. In these measurements however, one applies large signals to the device under test with a frequency of up to 2000 Hz (or even higher). With these measurements it is possible to determine certain parameters of the ferroelectric such as remanent polarization P_r or coercive voltage V_c (or field E_c). The basic principle of such a measurement is presented in Figure 4.4 (a). Here, a signal generator with its internal resistance R_i is connected in series with the ferroelectric device under test and a current amplifier. The “amplifier” can be a simple shunt resistor or a defined capacitor (Sawyer-Tower method [125]).

Virtual Ground Method

A more sophisticated method for measuring polarization loops is the virtual ground operational amplifier technique [126] which allows better measurements of slow transient responses. Its principle circuit is shown in Figure 4.4 (b). Here, the bottom electrode of the capacitor under investigation is connected to the virtual ground potential from the operational amplifier. De-

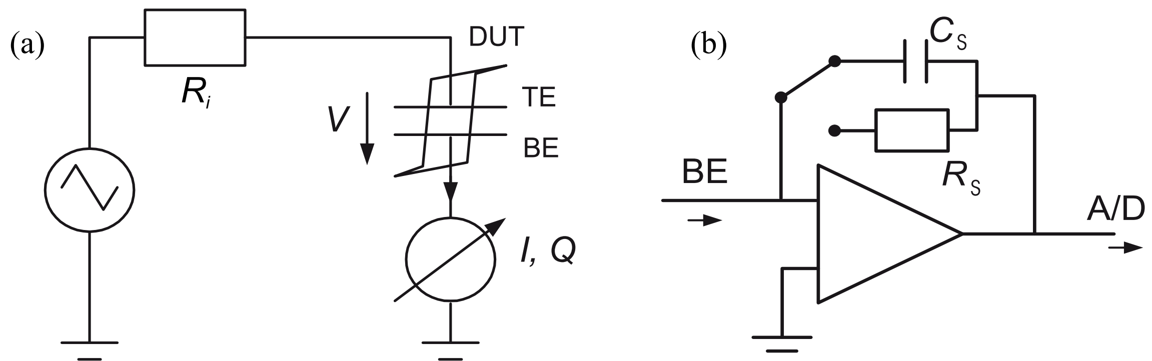

FIGURE 4.4:
(a) Schematic hysteresis measurement setup: Waveform generator, device under test and amplifier.
(b) Virtual ground operational amplifier circuit.

pending on the choice of the circuit element in the feedback loop, the amplifier acts as a current amplifier (Resistor R_s) or a current integrator (Capacitor C_S) and provides a signal proportional to the current or proportional to the charge (which is the integrated current). The hysteresis curves presented in this work were recorded with an aixACCT TF analyzer 2000 [127].

5 Results

In this chapter, the achieved experimental results from microstructure characterization and electrical characterizations are presented.

5.1 Physical Characterization: X-Ray Diffraction

The samples have been analyzed by X-Ray diffraction (XRD) [128,129] concerning their phase purity and crystallographic texture using a Philips X'PERT diffractometer with a CuK_{α} cathode. Measurements have been performed using the Bragg-Brentano geometry (θ - 2θ), in which the counter records lattice planes parallel to the film surface. A comparison of the results with those of powder diffractometer databases[6] gives insight into the preferential crystallographic orientation of the films.

Figure 5.1 shows the results of XRD measurements on the two sample series with different

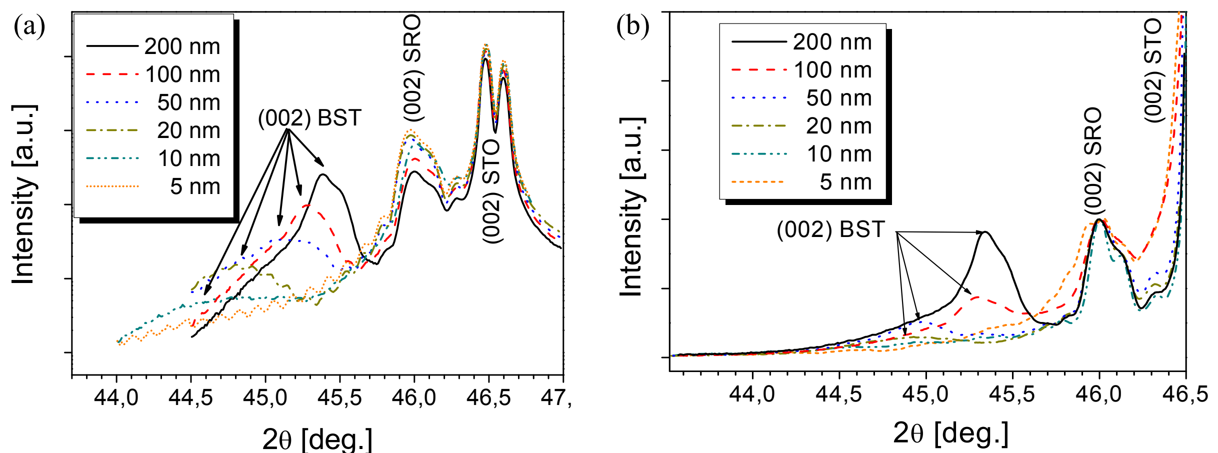

FIGURE 5.1:
XRD measurement of STO/SRO/BST heterostructures with different BST thicknesses
(a) Samples with DC-sputtered Pt top electrodes
(b) Samples with epitaxial SRO top electrodes deposited by PLD

BST thicknesses. Whereas the left figure (Figure 5.1 (a)) shows measurements on samples with Pt top-electrodes, the right figure (Figure 5.1 (b)) displays the results from similar samples with SRO top electrodes. As can be seen, both series show peaks in the range of ~45°, which is about the angle to be expected for the (002) orientation in powder samples of this

6. e.g. database of the International Center of Diffraction Data (ICCD)

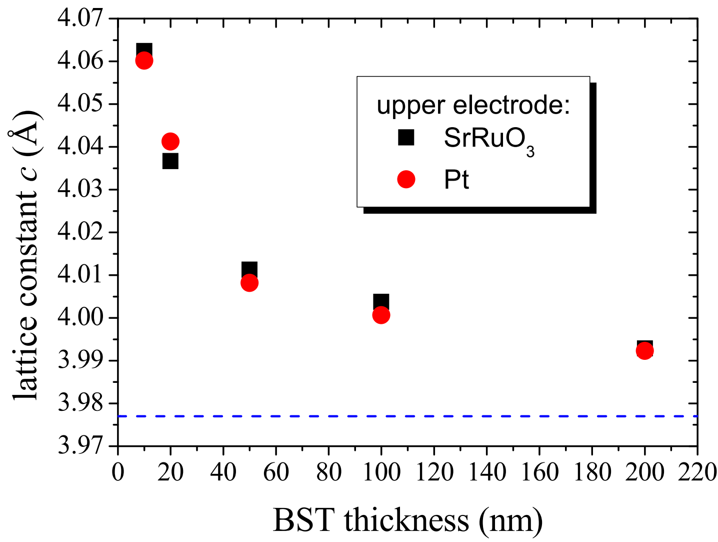

FIGURE 5.2:
Thickness dependence of the out-of-plane lattice constant c of epitaxial BST films determined by x-ray diffraction. The dotted line shows the bulk lattice constant.

BST composition (45.4° – 45.6°). The peak at ~46° can be attributed to the (002) orientation of SRO, which would be expected at exactly 46.2° according to the diffraction database. In general, it is remarkable that the BST peak is shifted to lower angles with decreasing film thickness, which gives a hint on the dependence of the out-of-plane lattice constants on the film thickness. These have been calculated using the X-ray diffraction calculation program PowderCell [130] and can be found in Figure 5.2. The samples show nearly identical lattice constants, regardless of the used electrode material, which means that their strain state does not differ at the particular film thickness (cmp. chapter 2.4) and does not depend on the top electrode. It can be seen that the STO substrate imposes compressive stress on the BST thin-film, in a way that the out-of-plane lattice constant becomes strongly elongated for the thinnest films. With increasing film thickness the out-of-plane lattice constant more and more decreases and approaches a final lattice constant, since above a critical thickness t_c misfit dislocations will be introduced due to energetic reasons which cause a thickness dependent strain relaxation. This final value is clearly higher than the bulk BST lattice constant (3.977 Å according to [62]).

The complete microstructure analysis of the involved samples has been carried out in Ref. 131, where the high-quality cube-on-cube epitaxial relationship between BST, SRO, and STO was proved by XRD φ-scan measurements ([303]SRO//[303]BST//[303]SRO//[303]STO indexed referring to the pseudocubic SRO unit cell). Rocking curves with a full width of 0.05° at half-maximum of the BST (002) peak were measured for both Pt/BST/SRO and SRO/BST/SRO

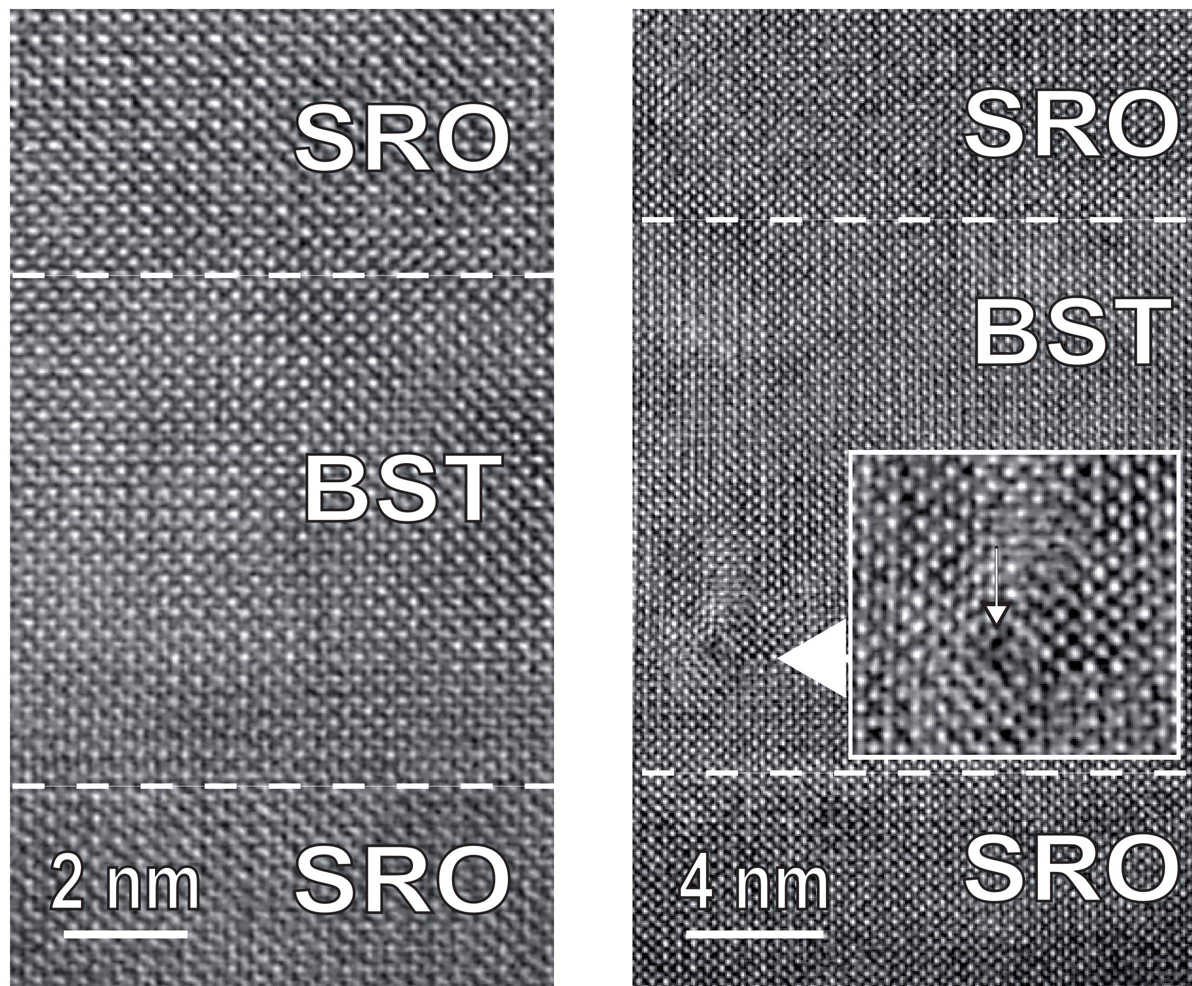

FIGURE 5.3:
HRTEM images of the SRO/BST/SRO system. Thickness of the BST layers are 10 nm (left) and 17 nm (right). The images show sharp BST/SRO interfaces with no misfit dislocations in the thinner and some misfit dislocations in the thicker sample.

stacks, which indicates that crystalline quality and strain state are independent on the top-electrode material.

To find out the critical thickness t_c, above which the generation of misfit dislocations is energetically favorable, high resolution transmission electron microscopy (HRTEM) images have been analyzed.[7] Using this method, atomic distances in crystals can be resolved, allowing here a direct conclusion on possible misfit dislocations. Additional information about the mechanisms of (HR)TEM can be found in Ref. 5.

7. HRTEM images were kindly prepared by J. Q. He and C. L. Jia (IFF, FZ Jülich).

Examples of such images are shown in Figure 5.3: On the left, a sample with SRO top and bottom electrode is presented, while the thickness of the BST layer could be determined to 10 nm. The right image shows a similar sample with a BST thickness of 17 nm. The BST/SRO interfaces in both cases are very sharp and do not display secondary (mixed) phases. Remarkably, there is no evidence of misfit dislocations in the thinner sample, while some misfit dislocations can be found in the thicker sample (marked by arrows, see magnification included in the right image). From these observations, the critical thickness can be approximated to

$$t_c \approx 10\ \text{nm}. \tag{5.1}$$

5.2 Electrical Characterization: Small Signal Response

Measurements of the small signal capacitance yield informations about the dielectric constant of the ferroelectric material at various conditions. In principle, one finds the contributions of the reversible polarization of the material under investigation, as has been investigated by Bolten [132]. In order to measure the pure capacitance (that gives the permittivity), one has to make sure that no polarization switching occurs which would falsify the measurements due to switching currents. Thus, the amplitude of the excitation voltage has to be kept below the value that allows for the polarization to be switched, or in other words: Small amplitudes of the excitation field will only result in small reversible displacements of the domain walls inside the material and reducing the amplitude of the excitation field results in a suppression of the irreversible displacements. The reversible capacitance according to Bolten is then defined as

$$C_{rev}(E) = \lim_{E_{AC} \to 0} C(E, E_{AC}), \tag{5.2}$$

where E_{AC} denotes the amplitude of the oscillating small signal excitation that is used to determine the capacitance, and E depicts the applied bias field. Indeed, this is the best (theoretical) method to determine the capacitance value of a device under test, but practically cannot be applied in real experiments: Since the measuring equipment as introduced in chapter 4.2.1 uses a non-vanishing amplitude of the excitation voltage, the task will be to determine the small signal capacitance with sufficient precision even in the case of non-zero excitation levels.

In the course of this work, capacitance measurements at V_{AC} = 10 mV (for better matching the zero excitation voltage need) and V_{AC} = 100 mV (for achieving a better signal-to-noise ratio SNR) excitation voltage level were performed.

The dielectric loss tangent tan (δ) (cmp. chapter 2.2) has been recorded simultaneously with the small signal capacitance and serves as a measure of the capacitor quality. For the measurement, a model circuit had to be chosen which would be the best approximation to the real capacitor. In this work, all small signal capacitance measurements were performed with a simplified C_p-D setup, which means a capacitor in parallel to a lossy element.

5.2.1 Voltage Dependence of the Small Signal Capacitance

Applying an electric field on a ferroelectric crystal either in its ferroelectric or paraelectric phase leads to a displacement of the atoms in the lattice against each other. The restoring force in the case of a real ionic lattice, such as a perovskite material arises from the local fields generated by the neighboring atoms and leads to a non-linear contra-force. The consequence of this is that the linear dependence between the dielectric displacement D and the electric field E (see Eq. (2.5)) no longer holds. Instead, the introduction of a *field-dependent* permittivity $\underline{\varepsilon}(E)$ is necessary. The effect of this non-linearity becomes significant at high electric fields. Hence, the effect is more frequently observed in thin films than in bulk dielectrics because high electric fields are more easily reached in thin films at only moderate voltages. A high permittivity corresponds to a smaller restoring force between the ions of the lattice and a large atomic displacement at a given field.

In the following, examples of the field dependent permittivity of the Pt and SRO samples will be illustrated. These graphs are often referred to as capacitance-voltage-curves (CV-curves), although usually the dielectric constant ε_r will be plotted so that the curves are independent of any geometry and can be easily compared with each other. It should be mentioned that all CV-curves presented in this work were measured with one DC-bias sweep from negative voltages up to positive voltages followed by one sweep from positive voltages down to negative voltages. The applied frequency for the CV-curves has been fixed at 10 kHz, while the bias voltage was assumed to be positive when the potential at the top electrode was higher than that of the bottom electrode. In particular cases, this results in two cone-shaped curves, each shifted for a

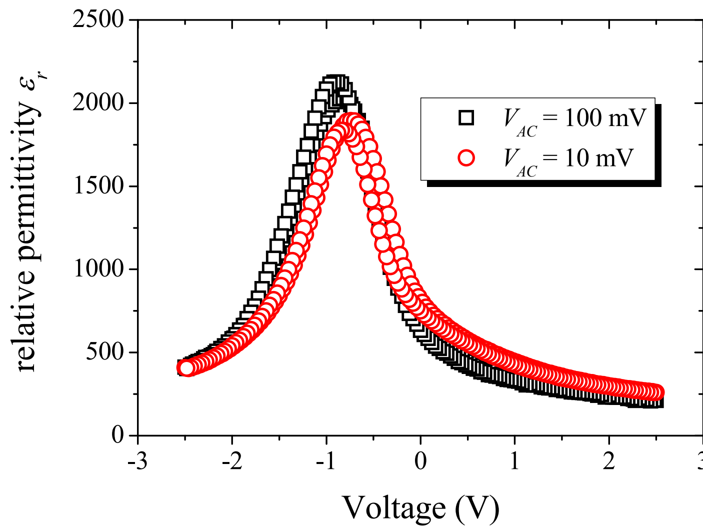

FIGURE 5.4: Voltage dependent permittivity curves of a Pt-sample with 130 nm BST thickness measured at room temperature with excitation voltage levels of V_{AC} = 100 mV (squares) and V_{AC} = 10 mV (circles)

certain amount of voltage up or down, relative to one central voltage value (0 V or very close to 0 V for the SRO samples), while in others these two curves do not differ from each other.

Pt samples

Figure 5.4 shows a *C-V*-measurement performed at room temperature (RT) with an excitation level of V_{AC} = 100 mV for a 130 nm Pt-sample (squares). The permittivity in the capacitor reaches a maximum value of $\varepsilon_{rmax,\mathrm{Pt}}\big|_{100\ \mathrm{mV}} \approx 2130$, which is by a factor of around 2/3 lower than the value reported in Ref. 64 for bulk ceramics at that particular temperature $(\varepsilon_{bulk} \approx 3000)$. Additionally, the CV-curve exhibits a shift towards negative voltages (V_{shift} = 0.8 V) with a slightly asymmetrical shape.

The same measurement was done at a lower excitation voltage level of V_{AC} = 10 mV and is plotted in Figure 5.4 (circles). Here, the amplitude $\varepsilon_{rmax,\mathrm{Pt}}\big|_{10\ \mathrm{mV}} \approx 1900$ of the CV-curve measured at V_{AC} = 10 mV is slightly lower compared to the 2130 for the case of V_{AC} = 100 mV. Besides this, no serious differences between these two curves could be observed.

Measurements on several samples with different BST thickness at the same temperature and excitation levels as mentioned above were performed. Figure 5.5 (a) shows the resulting CV-curves from measurements at V_{AC} = 100 mV. In general, a decrease of the permittivity with decreasing film thickness can be observed, similar to what has been reported earlier in the framework of the “dead-layer” model (chapter 3). The amplitudes of the dielectric constants

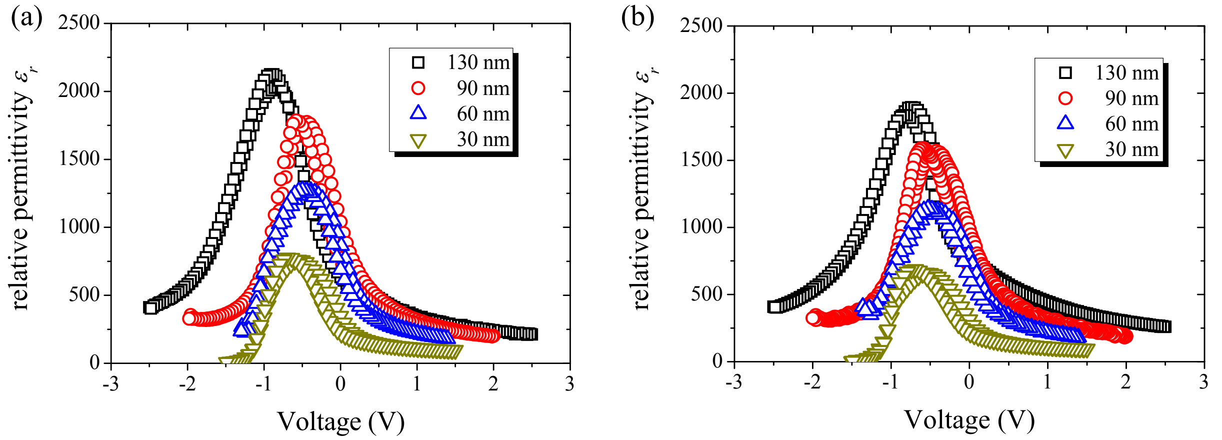

FIGURE 5.5:
CV-curves of Pt samples with different BST thickness, again measured at RT
(a) V_{AC} = 100 mV
(b) V_{AC} = 10 mV

$\varepsilon_{rmax,\mathrm{Pt}}|_{100\ \mathrm{mV}}$ can be determined to 2130 (measured at the 130 nm BST capacitors), 1790 (90 nm BST), 1270 (60 nm BST), and 780 (30 nm BST). There is a noticeable shift towards negative voltages for all curves by around -0.8 to -0.5 V with slightly different shaped partial curves depending on the direction of the voltage sweep (up or down). This shift can be attributed to an internal electric field caused by different electrode work functions (4.6 – 4.8 eV for SRO [69] and 5.3 eV for Pt [68]). Again, these measurements were repeated on the same samples at a reduced excitation voltage level of 10 mV. The resulting CV-curves can be found in Figure 5.5 (b), while their amplitudes $\varepsilon_{rmax,\mathrm{Pt}}|_{10\ \mathrm{mV}}$ are in general slightly lower compared to the results from the measurements at V_{AC} = 100 mV. For the 130 nm sample, the value can be determined to 1900 (2130 at V_{AC} = 100 mV), the 90 nm sample yields a maximum permittivity of 1590 (1790 at V_{AC} = 100 mV), 1150 is the peak value for the 60 nm sample (1270 at V_{AC} = 100 mV) and the 30 nm sample gives a maximum permittivity of 690 (compared to the 780 for the measurement at V_{AC} = 100 mV). Again, the overall differences between both measurements are not very serious, nevertheless one should keep in mind that in order to get the pure dielectric capacitance it is advisable to account for the lowest possible excitation level.

The analysis of the reciprocal capacitance density $A/C_{eff} = c_{eff}^{-1}$ as a function of the BST thickness for samples under investigation is depicted in Figure 5.6. Here, the capacitance values at the maximum of the CV-curves have been utilized. As can be seen, a linear dependence

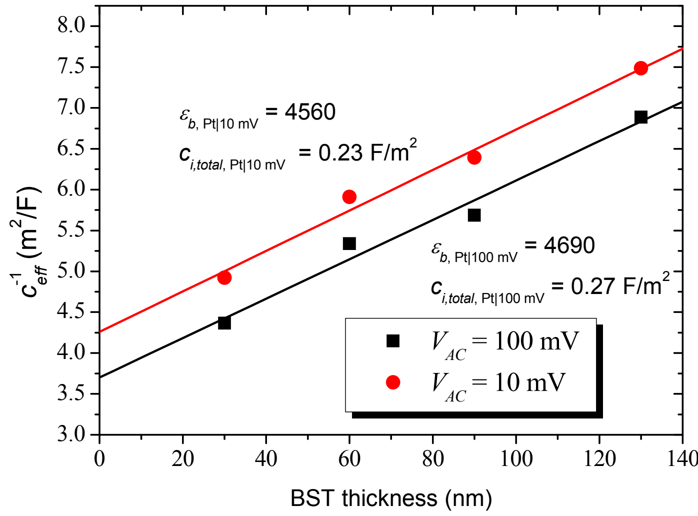

FIGURE 5.6: Thickness dependence of the reciprocal capacitance density for the Pt samples.

of c_{eff}^{-1} (squared and round data markers in the graph) on the BST thickness t is valid for the Pt samples, regardless of the used excitation voltage level. From a linear fit on these data points one can find the core parameters ε_b and $c_{i,total}$ according to Eq. (3.1). While ε_b describes the permittivity of a Pt sample with an infinitely thick BST layer (denoted here as the bulk permittivity), $c_{i,total}$ can be regarded as the total capacitance density of the low permittivity interface layer that has the same value in each sample irrespective of its actual BST thickness. Here, the determined values for the permittivity are quite identical with $\varepsilon_{b,\,\mathrm{Pt}}\big|_{100\ \mathrm{mV}} \approx 4690$ and $\varepsilon_{b,\,\mathrm{Pt}}\big|_{10\ \mathrm{mV}} \approx 4560$, both exceeding the value $\varepsilon_b \approx 3000$ found in Ref. 64 which was measured on bulk ceramic samples. It is important to mention that due to a possible shift of the phase transition (cmp. next sub-chapters), a comparison of permittivity values at constant temperatures may result in a comparison of materials with different state, e.g. the material may be in its FE state in one sample, whereas it may be in its PE state for another sample at the same temperature. For the interface capacitance density, values of $c_{i,\,total,\,\mathrm{Pt}}\big|_{100\ \mathrm{mV}} = 0.27\ \mathrm{F/m^2}$ and $c_{i,\,total,\,\mathrm{Pt}}\big|_{10\ \mathrm{mV}} = 0.23\ \mathrm{F/m^2}$ could be determined.

SRO Samples

Similar as for the Pt samples, measurements of CV-curves were also performed at the SRO samples. An example of such a measurement is given in Figure 5.7. Here, the CV-curve from a 125 nm BST capacitor with epitaxial SRO top electrodes is shown, whereas the whole measurement was performed at room temperature using an oscillation voltage level of $V_{AC} = 100\ \mathrm{mV}$ (squares). The maximum value of the measured permittivity curve can be

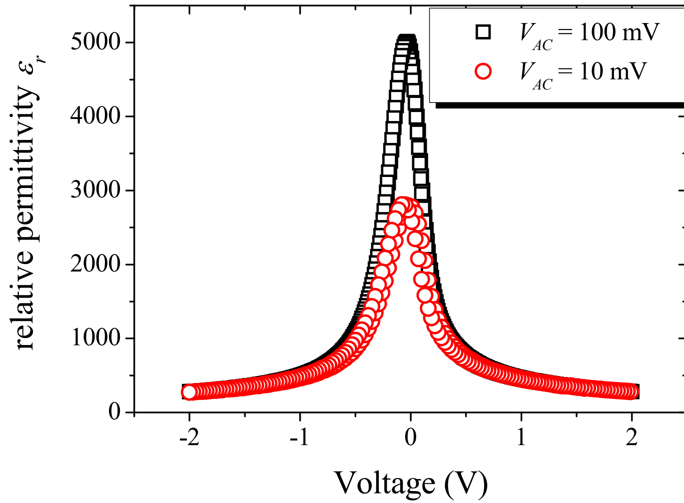

FIGURE 5.7: Permittivity curve of a 125 nm BST capacitor with SRO top electrode measured at room temperature with excitation voltage levels of $V_{AC} = 100$ mV (squares) and $V_{AC} = 10$ mV (circles)

found as high as $\varepsilon_{rmax}|_{100\ \mathrm{mV}} \approx 5010$. Here, the curve is almost exactly centered at 0 V, while the two partial curves do not really differ from each other. The sample exhibits a high tunability, i.e. applying a small DC-bias voltage results in a huge decrease of the capacitance.

The same type of measurement was performed on this sample with $V_{AC} = 10$ mV and has also been plotted into Figure 5.7 (circles). It is obvious that the two determined curves strongly differ in their maximum permittivity values: While the measurement at $V_{AC} = 100$ mV yields a maximum value of $\varepsilon_{rmax}|_{100\ \mathrm{mV}} \approx 5010$, the measurement using an excitation voltage of $V_{AC} = 10$ mV results in a lower value of $\varepsilon_{rmax}|_{10\ \mathrm{mV}} \approx 2800$, which is only slightly more than half of the value at $V_{AC} = 100$ mV.

Performing the same measurements on additional SRO samples with different thicknesses, a series of CV-curves resulted that can be found in Figure 5.8 (a) (for $V_{AC} = 100$ mV). Again, the permittivity decreases with decreasing BST thickness as mentioned before in the dead-layer framework. Here, the amplitudes $\varepsilon_{rmax,\ \mathrm{SRO}}|_{100\ \mathrm{mV}}$ of the CV-curves can be determined to 5010 (125 nm BST thickness), 3420 (70 nm), 2980 (50 nm) and 1470 (15 nm).

The same analysis with a reduced excitation level of $V_{AC} = 10$ mV is shown in Figure 5.8 (b). The graph looks quite similar to that recorded with $V_{AC} = 100$ mV, but in detail differs when comparing the maximum permittivity $\varepsilon_{rmax,\ \mathrm{SRO}}|_{10\ \mathrm{mV}}$ with $\varepsilon_{rmax,\ \mathrm{SRO}}|_{100\ \mathrm{mV}}$ for each thickness: For the thickest film (125 nm), the measured permittivity is only about 2800 (compared to the 5010 at $V_{AC} = 100$ mV), the permittivity of the 70 nm sample could be measured to 2260

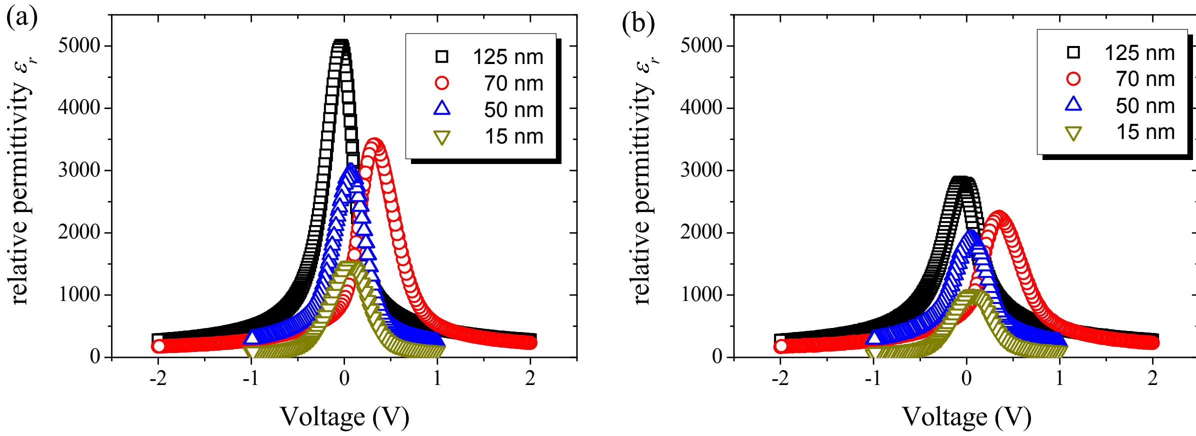

FIGURE 5.8:
CV-curves of SRO samples with different BST thickness, measured at RT
(a) V_{AC} = 100 mV at RT
(b) V_{AC} = 10 mV at RT

(3420 in the case of V_{AC} = 100 mV), the value of the 50 nm sample could be determined to 1910 (2980 at V_{AC} = 100 mV) and the permittivity maximum of the 15 nm sample decreased to 1010 (instead of 1470 for V_{AC} = 100 mV).

Finally, the analysis of the reciprocal capacitance density according to Eq. (3.1) was performed, as can be seen in Figure 5.9. The "bulk" permittivity of the SRO samples could be calculated to $\varepsilon_{b,\,\mathrm{SRO}}\big|_{100\ \mathrm{mV}} \approx 7510$ and $\varepsilon_{b,\,\mathrm{SRO}}\big|_{10\ \mathrm{mV}} \approx 3740$, while the interface capacitance density was determined to $c_{i,\,total,\,\mathrm{SRO}}\big|_{100\ \mathrm{mV}} = 0.93\ \mathrm{F/m^2}$ and $c_{i,\,total,\,\mathrm{SRO}}\big|_{10\ \mathrm{mV}} = 0.78\ \mathrm{F/m^2}$. Obviously, there is a striking difference in the measured bulk

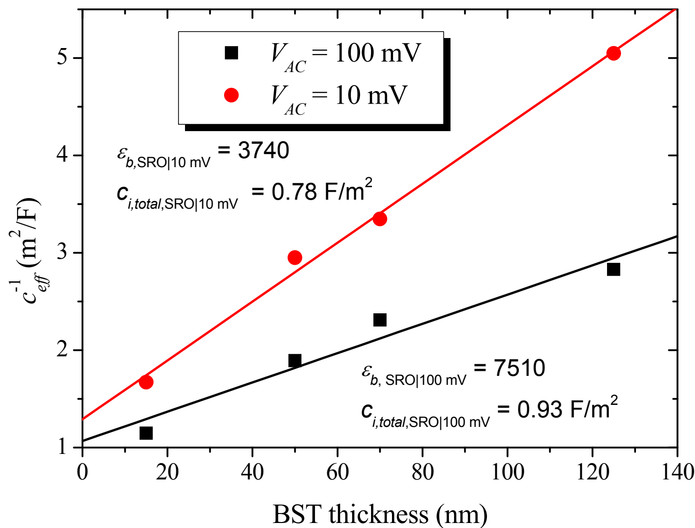

FIGURE 5.9:
Thickness dependence of the reciprocal capacitance density for the SRO samples.

permittivity when the excitation level V_{AC} is varied: The value becomes more than twice as high for the higher excitation amplitude, while the interface capacitance density only slightly changes.

Hence, the calculated bulk permittivity and reciprocal interface capacitance of the Pt and SRO sample series at room temperature range in a similar order of magnitude when choosing the lower excitation voltage level V_{AC} = 10 mV, but strongly differ in the case of V_{AC} = 100 mV.

5.2.2 Temperature dependence

From the considerations in chapter 2.2 a general temperature dependence of the permittivity in ferroelectrics can be expected. Measurements of the capacitance in a wide temperature range will be discussed in the following.

Pt samples

Figure 5.10 (a) shows the dependence of the permittivity measured on a 130 nm BST capacitor with Pt top electrode at three different temperatures when using an excitation voltage level of V_{AC} = 100 mV. As expected, the permittivity amplitude of the curves increases with increasing temperatures up to ~300 K and then decreases with further increasing the temperature. Again, the same measurements were performed at the lower V_{AC} = 10 mV. Figure 5.10 (b) shows the resulting CV-curves that look quite similar to those shown in Figure 5.10 (a).

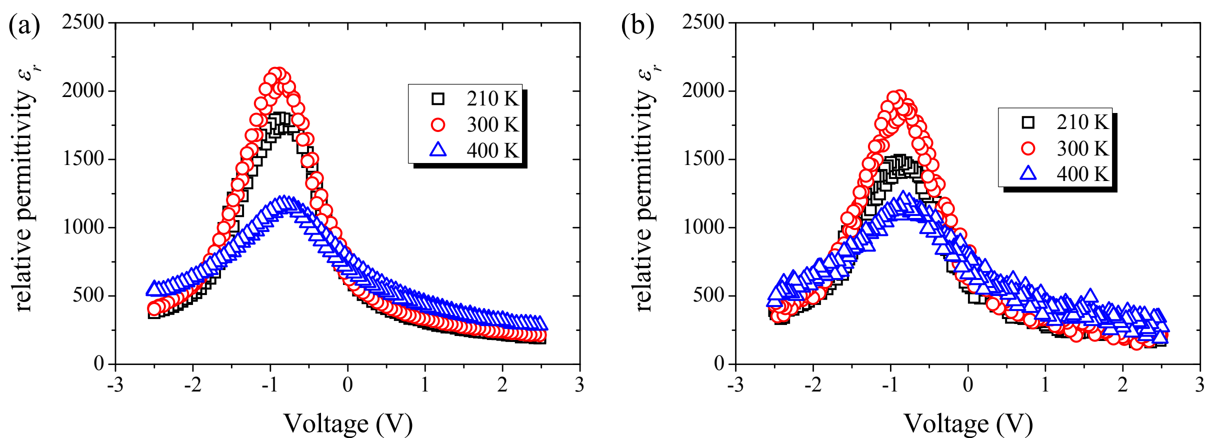

FIGURE 5.10:
CV-curves from a Pt sample with 130 nm BST thickness, measured at three different temperatures
(a) V_{AC} = 100 mV
(b) V_{AC} = 10 mV

To get a better overview on the temperature dependence of the maximum permittivity values, Figure 5.11 shows the development of the permittivity over a temperature range from 210 K up to 470 K on the same 130 nm Pt sample, measured with an excitation level of V_{AC} = 100 mV (squares). The resulting ε_r vs. T curve shows a distinct, but somehow broadened peak with a maximum permittivity of $\varepsilon_{rmax,\,\mathrm{Pt}}\big|_{100\ \mathrm{mV}} \approx 2130$. In contrast to other publications dealing with (polycrystalline) thin films [15,89], a pronounced peak in the ε_r vs. T curve can be observed at a phase transition temperature $T_{C,\,\mathrm{Pt}}\big|_{100\ \mathrm{mV}} \approx 290\ \mathrm{K}$, marked with a circle in the graph. This value is slightly lower compared to the 310 K found in Ref. 64. From measurements at V_{AC} = 10 mV, the temperature dependent permittivity values were also extracted and have also been plotted into Figure 5.11 (circles). The resulting phase transition can be determined to $T_{C,\,\mathrm{Pt}}\big|_{10\ \mathrm{mV}} \approx 310\ \mathrm{K}$, which is about 20 K higher than measured with V_{AC} = 100 mV, while the permittivity $\varepsilon_{rmax,\,\mathrm{Pt}}\big|_{10\ \mathrm{mV}} \approx 1980$ at that temperature is slightly lower than with 100 mV.

It becomes obvious, that a lower excitation voltage level yields an apparently higher phase transition temperature, which is an important result. For the Pt sample under investigation here, the T_C-shift ΔT_C = 20 K is quite moderate, but nevertheless one has to keep in mind that the choice of high excitation voltage levels result in an apparently lower phase transition temperature. The difference in the amplitudes of both ε_r vs. T will be discussed in detail in the next chapter. Finally, Figure 5.11 shows that at temperatures above the phase transition (T > 340 K) the used V_{AC} does not influence the resulting permittivity values.

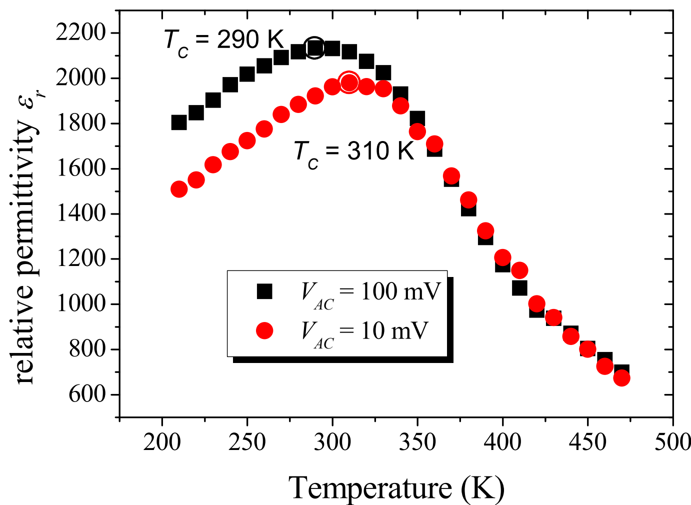

FIGURE 5.11: Temperature dependence of the permittivity of a 130 nm thick BST capacitor with Pt top-electrode and excitation voltage levels of V_{AC} = 100 mV (squares) and V_{AC} = 10 mV (circles)

Temperature dependent measurements of the CV-curves were performed for various samples with different thicknesses in the Pt series. Figure 5.12 (a) shows the resulting ε_r vs T-curves that were found when measuring with V_{AC} = 100 mV. Obviously, the phase transition temperature varies with the BST film thickness: By decreasing the BST thickness of the capacitors, the phase transition temperature increases from starting values of ~ 290 K for the 130 nm sample up to 360 K for the 30 nm sample. The maximum permittivity values $\varepsilon_{rmax,\,\mathrm{Pt}}\big|_{100\ \mathrm{mV}}$ of the samples behave as expected when decreasing from 2130 (130 nm BST thickness) to 1790 (90 nm) down to 1270 (60 nm) and finally reach a value of 830 (30 nm). With decreasing BST-thickness, the resulting ε_r vs T-curves become broader so that the ferroelectric phase transition is less pronounced and even show a smeared phase transition in the case of the thinnest (30 nm) samples.

Similar investigations on the Pt samples were performed in the complete temperature range using V_{AC} = 10 mV and yield the ε_r vs T-curves shown in Figure 5.12 (b). On the first view, there is no significant difference between the analyses for 10 and 100 mV. The phase transition temperatures are shifted for about 20 K upwards, while the permittivities at the phase transition become slightly diminished compared to the measurements at V_{AC} = 100 mV: For the 130 nm sample, one can find a permittivity amplitude of $\varepsilon_{rmax,\,\mathrm{Pt}}\big|_{10\ \mathrm{mV}} \approx 1980$ (compared to the 2130 at V_{AC} = 100 mV), the value for the 90 nm sample drops down to 1640 (from 1790), at 60 nm

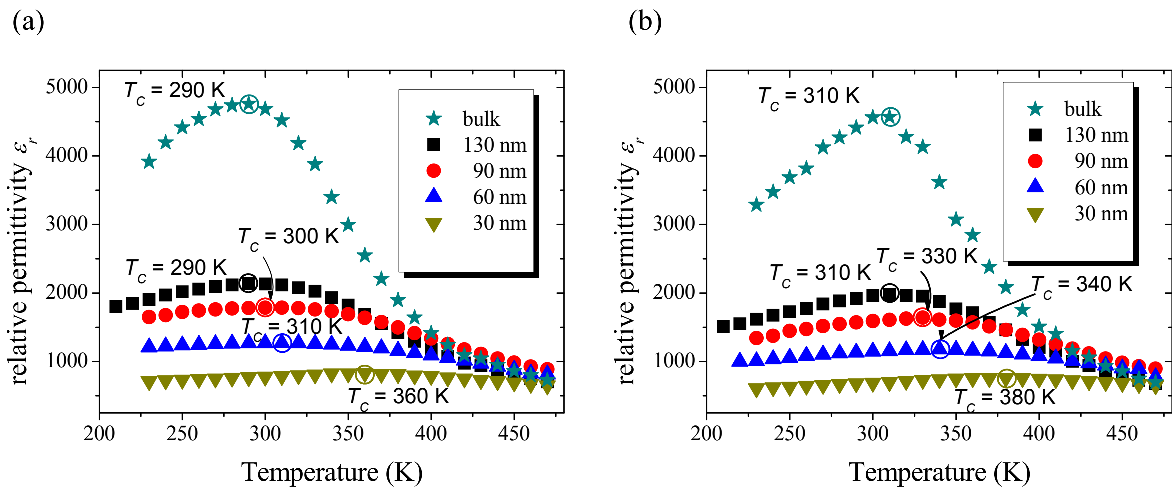

FIGURE 5.12:
Temperature dependence of the permittivity of Pt samples at all available BST thicknesses as well as the calculated bulk permittivity values (stars).
(a) V_{AC} = 100 mV
(b) V_{AC} = 10 mV

the permittivity maximum can be determined to 1180 (instead of 1270) and the 30 nm sample yields a maximum permittivity value of about 760 (compared to 830 found before).

Those values determined at the lower V_{AC} value might not be the absolute true permittivity values, but should be close to what is expected to be the "pure" permittivity without a significant influence of the polarization switching.

An analysis of the reciprocal capacitance density (cmp. Figure 5.6) has been performed for the complete temperature range, so that the temperature dependence of the bulk permittivity as well as that for the interface capacitance could be achieved. The resulting graph of the extracted bulk permittivity has been plotted into Figure 5.12. For both chosen excitation voltages, the phase transition temperature of the bulk permittivity follows the trend from the samples with values of $T_{C,\text{ bulk}}\big|_{100\text{ mV}} \approx 290\text{ K}$ and $T_{C,\text{ bulk}}\big|_{10\text{ mV}} \approx 310\text{ K}$ (same as what has been found for the 130 nm sample). The corresponding amplitudes of the bulk permittivities can be determined to $\varepsilon_{b,max}\big|_{100\text{ mV}} \approx 4760$ as well as $\varepsilon_{b,max}\big|_{10\text{ mV}} \approx 4570$.

For comparison reasons, Figure 5.13 (a) shows the bulk permittivities determined for the two V_{AC} levels. Similar to what has been observed for the measured permittivity of the "real" samples, the calculated bulk permittivity from the thickness series also shows a shift of the phase transition temperature for about 20 K as well as a nearly identical behavior for both V_{AC} levels

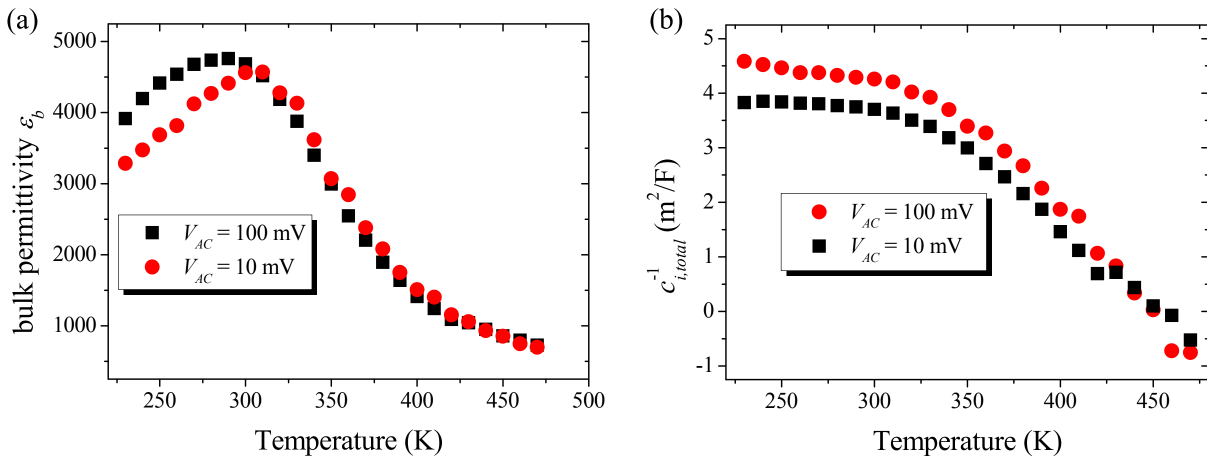

FIGURE 5.13:
(a) Comparison of the bulk permittivity values measured with two different excitation voltage levels.
(b) Temperature dependence of the reciprocal interface capacitance density derived from the Pt sample series using two different V_{AC} voltages.

in the temperature region above the phase transition. The reciprocal interface capacitance density $c_{i,\,total,\,\mathrm{Pt}}^{-1}$, derived from the second parameter of the analysis according to Eq. (3.1), has been plotted in Figure 5.13 (b). Here, the values determined above the phase transition for the two different excitation voltages do not match as perfect as it was the case for the bulk permittivity, but they nevertheless show a very similar trend with values in the same order of magnitude. The thus determined interface capacitance shows a strong temperature dependence in the observed temperature region. The interface values $c_{i,\,total}^{-1}(T)$ decrease by increasing the temperature from a more or less stable plateau at temperatures between 230 and 300 K (around 4 m^2/F) down to a zero-interface at around 450 K and become even negative at higher temperatures.

SRO samples

CV-curves at different temperatures were also determined for SRO samples, as can be seen in the resulting graphs in Figure 5.14 (a). Here, a similar temperature dependence can be observed as seen before at the Pt samples. Also noticeable is the shape of the curves: They are all well centered around 0 V, while for the lowest temperatures the two partial curves are slightly shifted to either side of the 0 V, indicating the ferroelectric phase which at higher temperatures disappears. Measurements with V_{AC} = 10 mV show a similar but in detail different view, as can be found in Figure 5.14 (b). Here, the ferroelectricity can be detected better due to the

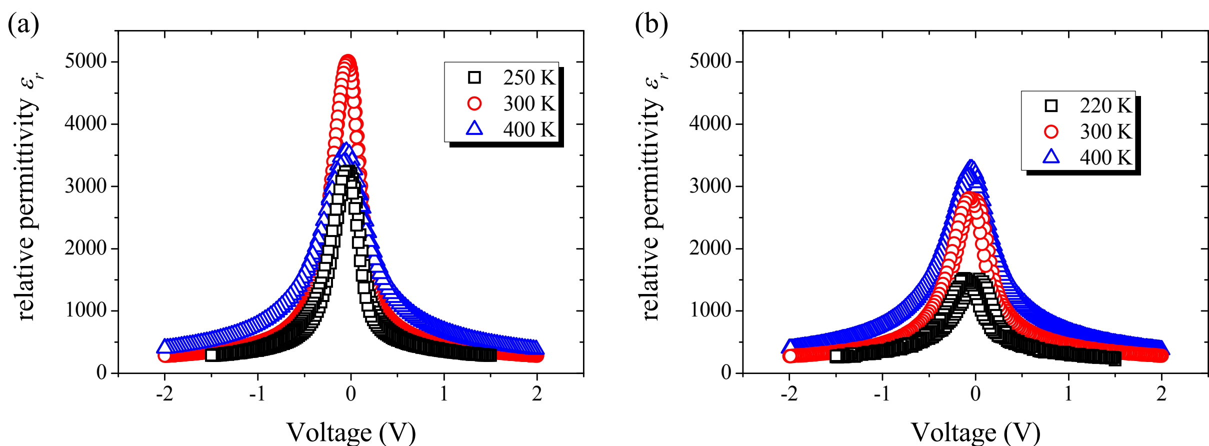

FIGURE 5.14:
CV-curves measured on one SRO sample with 125 nm BST thickness, performed at three different temperatures
(a) V_{AC} = 100 mV
(b) V_{AC} = 10 mV

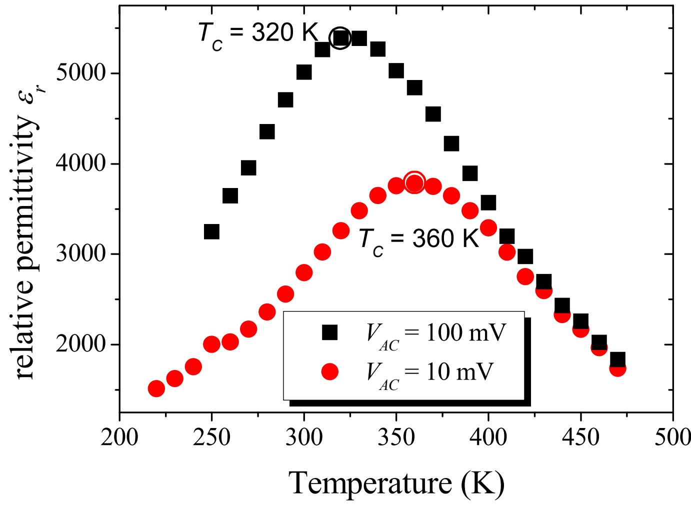

FIGURE 5.15: Temperature dependence of the permittivity of a 125 nm BST sample with SRO top electrodes, measured with $V_{AC} = 100$ mV (squares) and $V_{AC} = 10$ mV (circles)

larger shift of the partial curves in the low temperature measurement. Also noteworthy is the reduced permittivity amplitude, that has already been mentioned in the RT comparison of the measured CV curves at that sample.

Again, the complete temperature dependence of the permittivity for such a sample has been investigated over a larger temperature range, as can be seen in Figure 5.15. The resulting ε_r vs T-curve performed at $V_{AC} = 100$ mV (squares) shows a bulk-like behavior with a maximum value of $\varepsilon_{rmax,\,\mathrm{SRO}}\big|_{100\ \mathrm{mV}} \approx 5390$, which is even slightly higher than the value of ~5200 found for the ceramic samples [64]. The corresponding phase transition temperature (marked with a circle) can be found at $T_{C,SRO} \approx 320\ \mathrm{K}$, a value that is slightly higher compared to the 310 K found at the ceramic samples. Using an excitation voltage of $V_{AC} = 10$ mV, the temperature dependence of the 125 nm SRO sample has been plotted into the same Figure 5.15 (circles). Again, a sharp ferroelectric phase transition can be detected, while the phase transition temperature has been shifted up to $T_{C,SRO} \approx 360\ \mathrm{K}$ (compared to the 320 K at $V_{AC} = 100$ mV). The permittivity at this temperature can be determined to the value of $\varepsilon_{rmax,\,\mathrm{SRO}}\big|_{10\ \mathrm{mV}} \approx 3780$, which is much lower than the 5390 found with $V_{AC} = 100$ mV. As expected, the temperature dependence of the permittivity becomes independent of the used V_{AC} when measuring at temperatures above the phase transition.

The same type of measurements has been performed at all available SRO samples. Figure 5.16 (a) shows the resulting graphs for measurements at $V_{AC} = 100$ mV, which reveal

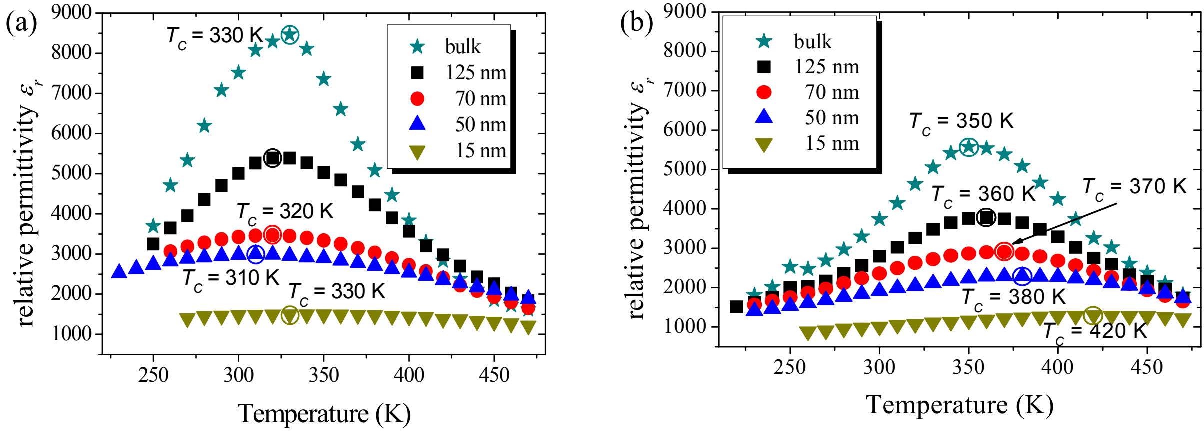

FIGURE 5.16:
Temperature dependence of the permittivity of SRO samples at all available BST thicknesses as well as the calculated bulk permittivity values (stars)
(a) V_{AC} = 100 mV
(b) V_{AC} = 10 mV

more or less stable values of the phase transition temperature in this measurement series of around $T_{C,\,\mathrm{SRO}}\big|_{100\ \mathrm{mV}} \approx 320 \pm 10\ \mathrm{K}$. The maximum permittivity values $\varepsilon_{rmax,\,\mathrm{SRO}}\big|_{100\ \mathrm{mV}}$ of the samples follow the trend of decreasing permittivities with decreasing film thickness. In detail, they decrease from 5390 (125 nm) down to 3470 (70 nm) and 3000 (50 nm) and finally reach the value of 1500 (15 nm). Especially at the thinnest samples the phase transition becomes strongly smeared with a permittivity plateau, thus making it difficult to definitely find the real phase transition, which could be somewhere between 300 and 380 K.

From measurements at V_{AC} = 10 mV, the plots in Figure 5.16 (b) result for the temperature dependent permittivity of the SRO samples. The graph is very different to what has been found in the case of V_{AC} = 100 mV (Figure 5.16 (a)), which manifests mostly in the dependence of the phase transition temperature $T_{C,\,\mathrm{SRO}}\big|_{10\ \mathrm{mV}}$ on the BST thickness: Here, similar to what has been found for the Pt samples, the values increase with decreasing film thickness from 360 K at 125 nm over 370 for the 70 nm sample up to 380 K at 50 nm and finally reach a T_C-value of 420 K for the thinnest 15 nm sample. The corresponding maximum permittivity values $\varepsilon_{rmax,\,\mathrm{SRO}}\big|_{10\ \mathrm{mV}}$ are all much lower than in the case of V_{AC} = 100 mV and can be determined to 3780 for the 125 nm sample (compared to the 5390 for V_{AC} = 100 mV), 2910 for the 70 nm sample (3470 for V_{AC} = 100 mV), 2290 for the 50 nm sample (3000 at V_{AC} = 100 mV) and 1300 for 15 nm (1500 at V_{AC} = 100 mV). Again, the phase transition for the thinnest sample

(15 nm) becomes rather smeared with a plateau-like maximum so that the actual phase transition temperature could lie somewhere between 400 and 440 K.

An analysis of the reciprocal capacitance density has been performed for the SRO samples in the whole temperature region according to Eq. (3.1). The calculated bulk permittivity ε_b is also shown in Figure 5.16. For the measurements at $V_{AC} = 100$ mV (Figure 5.16 (a)), a maximum bulk permittivity can be determined to $\varepsilon_{b,max}\big|_{100\text{ mV}} \approx 8470$. The corresponding phase transition temperature $T_{C,\text{ bulk}}\big|_{100\text{ mV}}$ also stays more or less in the region of the phase transition temperatures of the single samples (~320 K) and can be determined to 330 K. The results of the analysis for the measurements at $V_{AC} = 10$ mV has been plotted in Figure 5.16 (b), where a maximum bulk permittivity of $\varepsilon_{b,max}\big|_{10\text{ mV}} \approx 5580$ could be determined. This value is only about 66% of the amount that could be determined for $V_{AC} = 100$ mV, while the phase transition follows the trend of increasing phase transition temperatures with increasing film thickness (supposed is an infinite film thickness for the calculated bulk permittivity).

For comparison reasons, both derived bulk permittivities as a function of temperature were plotted in Figure 5.17 (a). It is obvious that in the lower temperature region the determined values strongly differ, while a better agreement can be observed at higher temperatures (above the phase transition temperature).

From the same analysis, the temperature dependence of the total reciprocal interface capaci-

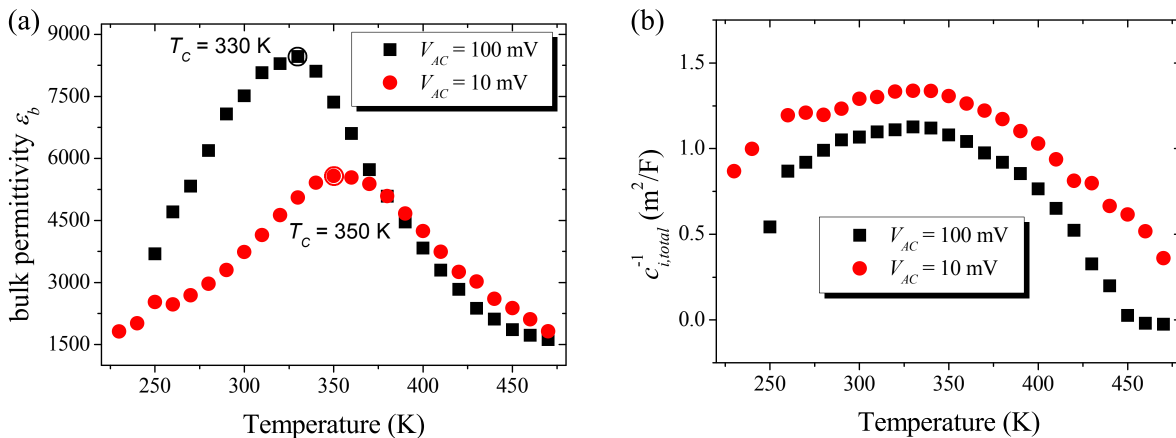

FIGURE 5.17:
(a) Temperature dependence of the bulk permittivity of the SRO samples, measured at $V_{AC} = 10$ mV and 100 mV
(b) Temperature dependence of the total interface capacitance density for the SRO samples

tance density $c_{i,\,total,\,\mathrm{SRO}}^{-1}$ could be derived, which has been plotted in Figure 5.17 (b). Here, the two different V_{AC} values result in a similar trend of the measured capacitance density, while the overall interface seems to be better in the case of V_{AC} = 100 mV. Compared to the Pt sample, the values behave more or less similar, while the absolute values of $c_{i,\,total}^{-1}$ are lower in the temperature region below ~430 K, which means a better interface in the case of BST/SRO than BST/Pt.

The analysis of the temperature dependence of the reciprocal capacitance density, as shown for Pt in Figure 5.13 (b) and for SRO in Figure 5.17 (b) reveals the total interface capacitance density for both interfaces in the thin film BST capacitor. From Figure 3.1, a more precise model considering two independent interfaces can be derived, which in analogy to Eq. (3.1) may be described by

$$\frac{1}{c_{eff}} = \frac{1}{c_{i1}} + \frac{1}{c_b} + \frac{1}{c_{i2}}. \tag{5.3}$$

Considering the SRO samples, both interfaces may be expected to be equal, so that the individual (reciprocal) SRO interface capacitance density can be expressed simply as $c_{i,\,\mathrm{SRO}}^{-1} = c_{i,\,total,\,\mathrm{SRO}}^{-1}/2$. For the separation of the interfaces of the Pt samples, the Pt interface capacitance density can be found with $c_{i,\mathrm{Pt}}^{-1} = c_{i,\,total,\mathrm{Pt}}^{-1} - c_{i,\mathrm{SRO}}^{-1}$ using the SRO values deter-

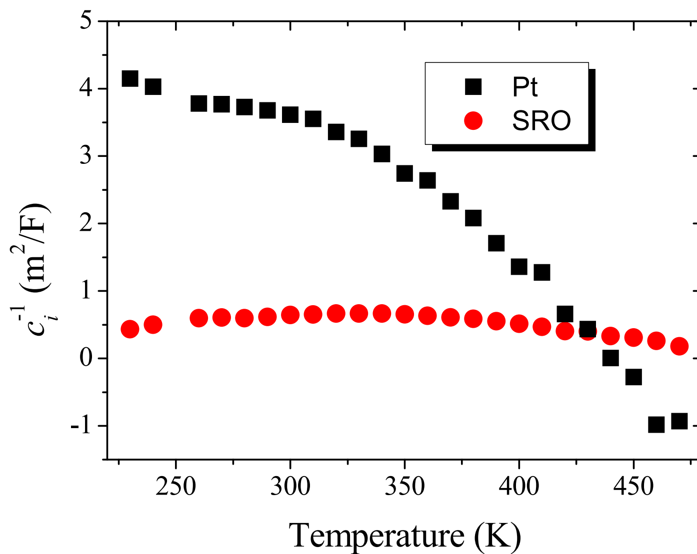

FIGURE 5.18: Temperature dependence of the separated reciprocal interface capacitance densities c_i^{-1} for the measurement with V_{AC} = 10 mV, performed on Pt samples (squares) and SRO samples (circles)

mined from the total SRO interface. This calculation has been done for 10 mV, and the results can be found in Figure 5.18. It can be seen that the trend of the values in the Pt samples as well as in the SRO samples does not differ significantly from that of the total interface. For the Pt samples the absolute values of the single interface approximately are the same as found for the total interface shown in Figure 5.13 (b), since in the series connection of two capacitors with dissimilar capacitance the value of the smaller capacitor (here the Pt interface capacitance) dominates. When considering SRO samples the values simply become half of their size compared to Figure 5.17 (b).

5.2.3 Loss tangent

Figure 5.19 shows the temperature dependent loss tangent recorded at certain investigated samples. In the case of a specimen with 90 nm BST thickness and Pt top electrodes, Figure 5.19 (a) shows a slight decrease of tan(δ) with increasing temperatures from 250 up to 400 K, while it increases again at temperatures between 400 and 470 K. The difference between measurements at V_{AC} = 10 mV and V_{AC} = 100 mV is rather negligible, while the smaller SNR for the measurements at 10 mV leads to a higher amount of noise, which manifests in the higher "roughness" of the tan(δ) curve. The absolute values of the loss tangent can be observed to be well below 0.1 up to the increase of tan(δ) at higher temperatures (T > 450 K).

A similar measurement is displayed in Figure 5.19 (b) for the 125 nm SRO sample, which dif-

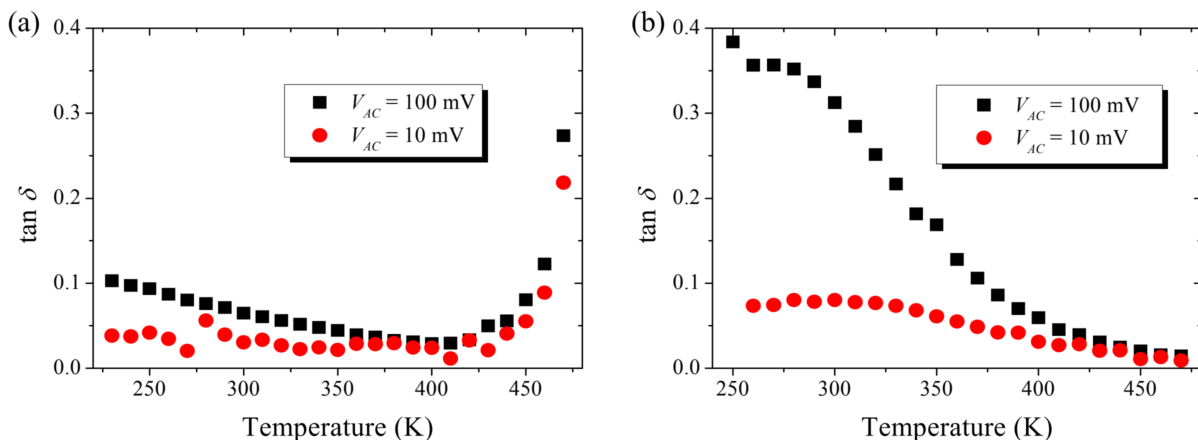

FIGURE 5.19:
Temperature dependent loss tangent of the investigated samples
(a) Pt sample with 90 nm BST thickness
(b) SRO sample with 125 nm BST thickness

fers drastically in comparison to what was found for the Pt samples: While tan(δ) at V_{AC} = 10 mV does not exceed 0.1 in the whole temperature range and decreases monotonically after its maximum of 0.08 at 280 K, the behavior for measurements at V_{AC} = 100 mV looks different. Here, tan(δ) has its maximum of 0.38 at 250 K (or even higher at lower temperatures) and decreases with increasing temperature until it reaches nearly identical values as the at 10 mV for temperatures above 400 K.

In general, the value of tan(δ) as the relationship between the imaginary and the real part of the capacitance gives a measure for the amount of resistance in comparison to its reactance (*R/X*). Since the measurements here were performed at non-zero frequencies, the dielectric loss is not only influenced by the capacitor DC-resistance but also by (ferroelectric) polarization switching.

5.3 Electrical Characterization: Large Signal Hysteresis Measurements

In the following, polarization measurements of both sample series will be presented. The frequency used in these measurements was chosen as 2 kHz (cmp. chapter 4.2.2), which resulted in reduced leakage currents compared to lower measurement frequencies. As it was already shown in recent publications, the choice of the frequency influences the coercive voltage V_C (and thus the coercive field E_c), but has a negligible impact on the remanent polarization P_r [126,132].

Pt samples

Figure 5.20 (a) shows a hysteresis measurement of a Pt sample with 130 nm BST thickness that was recorded at room temperature. From this curve, the remanent polarization P_r has been achieved, which in the depicted case can be found as the zero voltage polarization value. In general, the *P*-*V* curves may show an *imprint* (shifted to positive or negative voltages), so that the polarization at 0 V does not coincide with the remanent polarization. Therefore, P_r will be calculated as

$$P_r = \frac{|P^*_{r+}| + |P^*_{r-}|}{2} \tag{5.4}$$

with P^*_{r+} as the real remanent polarization in the upper part of the hysteresis loop (cycled from

positive to negative voltage) and P^*_{r-} as the real remanent polarization in the lower part of the hysteresis loop (cycled from negative to positive voltage), both determined at the *corrected* remanent voltage $V_r = (V_{c+} + V_{c-})/2$. Here, V_{c+} and V_{c-} are the values of the positive and negative coercive voltage determined from a standard hysteresis measurement.

Similar measurements have been performed for the Pt samples with 90 and 60 nm BST thickness, as shown in Figure 5.20 (b) and Figure 5.20 (c). For both samples an imprint of about -400 mV has been determined, which in this case coincides with the resulting voltage shift from the room temperature *C-V* curves presented in Figure 5.5 (a) and Figure 5.5 (b).

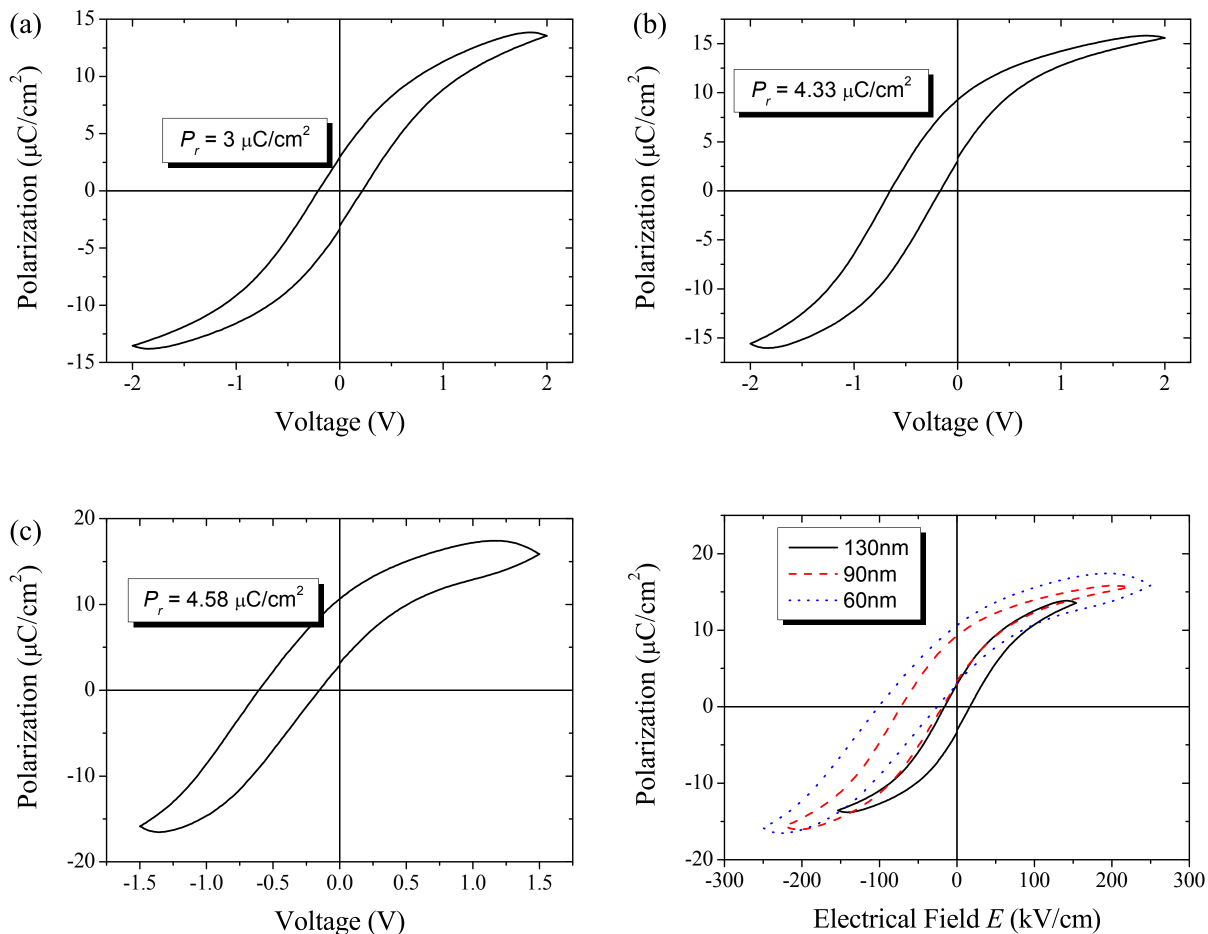

FIGURE 5.20:
Hysteresis measurement, performed on Pt samples at RT
(a) 130 nm BST thickness
(b) 90 nm BST thickness
(c) 60 nm BST thickness
(d) The hysteresis loops of (a) - (c) shown as a function of the applied electrical field

The presented hysteresis curves in Figure 5.20 (b) and Figure 5.20 (c) result in an apparent remanent polarization value of $P_r \approx 4.3$ .. 4.6 μC/cm^2. However, from the *P*-*V* loop of the 60 nm sample in Figure 5.20 (c) it can be assumed that this value is falsified strongly by leakage currents, since the curves at the maximum (and minimum) bias voltage are not as tapered as expected. In contrast, the loop in Figure 5.20 (b), determined from the 90 nm sample still looks rather free from strong leakage currents, which makes this P_r value more reliable. Figure 5.20 (d) shows all three aforementioned hysteresis loops in one diagram as a function of the applied electrical field. Notably, the coercive field increases with decreasing thickness of the BST film, which has been already reported in previous publications [133].

The thinnest sample (30 nm) did not allow the measurement of meaningful hysteresis loops due to its strong leakage currents which made it impossible to conclude on the ferroelectricity of this sample.

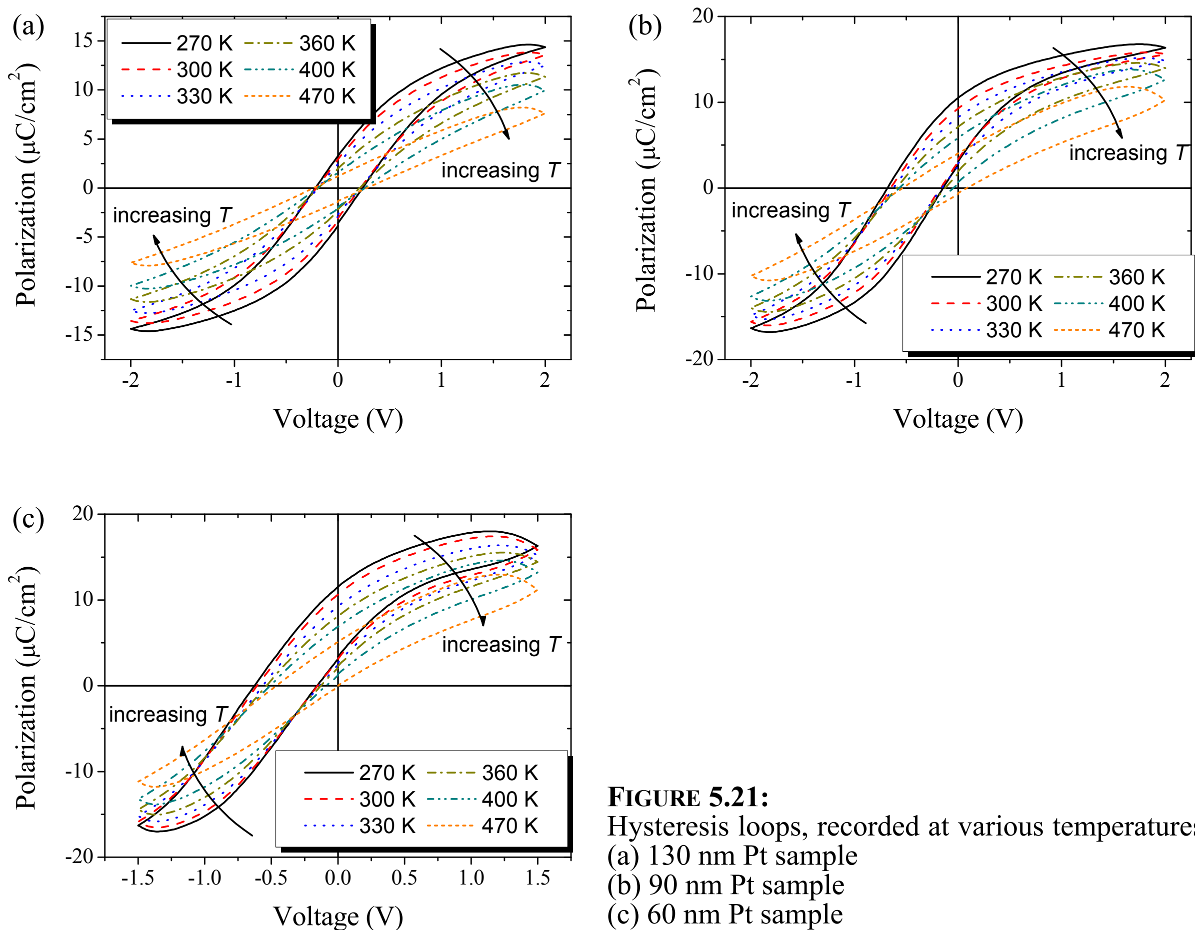

FIGURE 5.21:
Hysteresis loops, recorded at various temperatures:
(a) 130 nm Pt sample
(b) 90 nm Pt sample
(c) 60 nm Pt sample

For the three thicker Pt samples (130, 90 & 60 nm BST thickness), hysteresis loops have been recorded also at various temperatures. Figure 5.21 shows the achieved *P-V* curves, which yield some remarkable results. For all samples under investigation, the maximum polarization value decreases with increasing temperature, as marked by the arrows. For the 130 nm sample (Figure 5.21 (a)), it can be seen that the coercive voltage did not change significantly with temperature, while the remanent polarization at that sample gradually decreases. The curves become more and more slanted by increasing the temperature and show broader ends, which indicates an increase of the leakage currents in the sample.

The temperature dependence of the hysteresis curves of the 90 and 60 nm samples is slightly different to what has been found for the 130 nm sample (Figure 5.21 (b) and (c)). Here, the curves show a shift of their coercive voltage by increasing the temperature due to their larger imprint, while the remanent polarization decreases as seen from the 130 nm sample. These curves also become slanted, while the leakage current seems to increase stronger than in the case of the 130 nm sample.

In general, it seems that the samples (partly) keep their ferroelectric state even at temperatures above their phase transition, determined from the temperature dependent small signal capacitance measurements of chapter 5.2.2.

SRO samples

Measurements of the ferroelectric hysteresis were also performed for the SRO samples and are presented in Figure 5.22. The remanent polarization values P_r decrease with decreasing BST thickness from 9.9 μC/cm^2 for the 125 nm sample over 9.24 μC/cm^2 for the 70 nm sample down to 7.76 μC/cm^2 measured at the 50 nm sample. This trend is opposite to what has been found for the Pt samples. The quality of the hysteresis loops seems to be satisfying, but one has to keep in mind that there was no chance to apply higher voltages on the thinner samples (70 & 50 nm) without generating large leakage currents. Thus, the curves appear to be slightly opened in the negative voltage region. Figure 5.22 (d) shows the hysteresis loops of the three samples all plotted in one diagram as a function of the applied electrical field. As it could be seen for Pt (Figure 5.20 (d)), again an increase of the coercive field with decreasing BST thickness is observable.

Large leakage currents made it impossible to achieve reliable *P-V* loops for the thinnest sample (15 nm), as it was also observed for the thinnest Pt sample.

As in the case of the Pt samples, the SRO samples were also characterized by means of their ferroelectricity in the available temperature region, thus resulting in the temperature dependence of their hysteresis loops as displayed in Figure 5.23. As can be seen, the coercive voltage for the 125 and 70 nm samples is more or less constant for the investigated temperatures, while it slightly shifts in the case of the 50 nm sample. All samples show a decrease in the maximum polarization by increasing the temperature (marked by arrows), as it could be observed for the Pt samples before. The hysteresis curves all become slanted with higher temperatures, thus in-

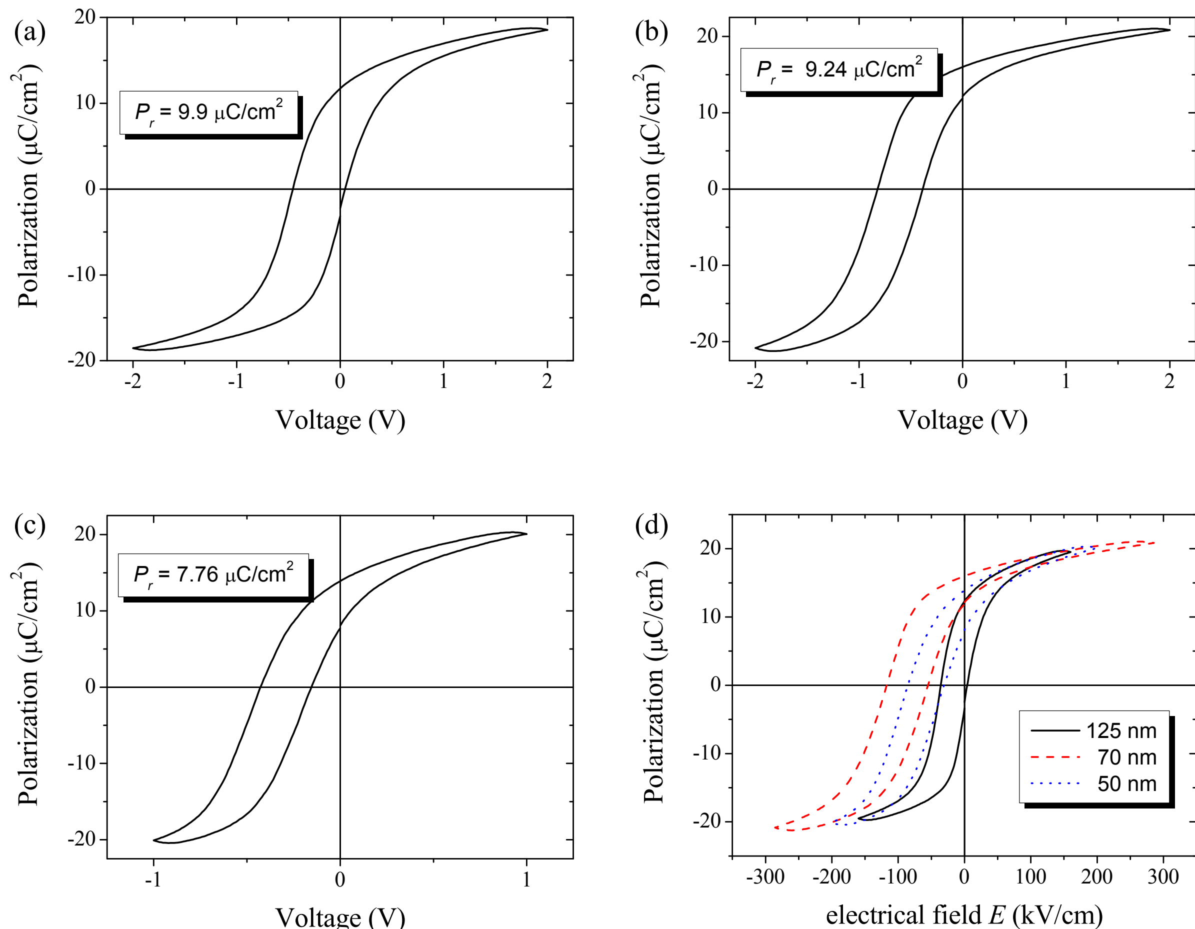

FIGURE 5.22:
Hysteresis loops measured on SRO samples at RT
(a) 125 nm
(b) 70 nm
(c) 50 nm
(d) The polarization of (a) - (c) shown as a function of the applied electrical field *E*.

dicating an increase of the leakage currents that occur in the polarization measurements.

5.4 Summary of the Experimental Results

To summarize this chapter, the following findings can be reported (here, only the values determined from the measurements with V_{AC} = 10 mV will be discussed):

- With the PLD technique it was possible to fabricate high quality epitaxial BST thin film capacitors with room temperature dielectric constants by far exceeding the values reported from earlier works. The achieved values for the thickest samples (~130 nm) are 2800 for SRO samples and 1900 for Pt, whereas the values reported from Refs. 12-18 and 84-90 reveal only low RT permittivities not exceeding 300.

- Analyses of the capacitor thickness series with Pt and epitaxial SRO top electrodes display a drastic difference in their RT interfacial capacitance density. Whereas a capacitance density of 1.55 F/m^2 has been determined for the SRO samples, the corresponding value for Pt

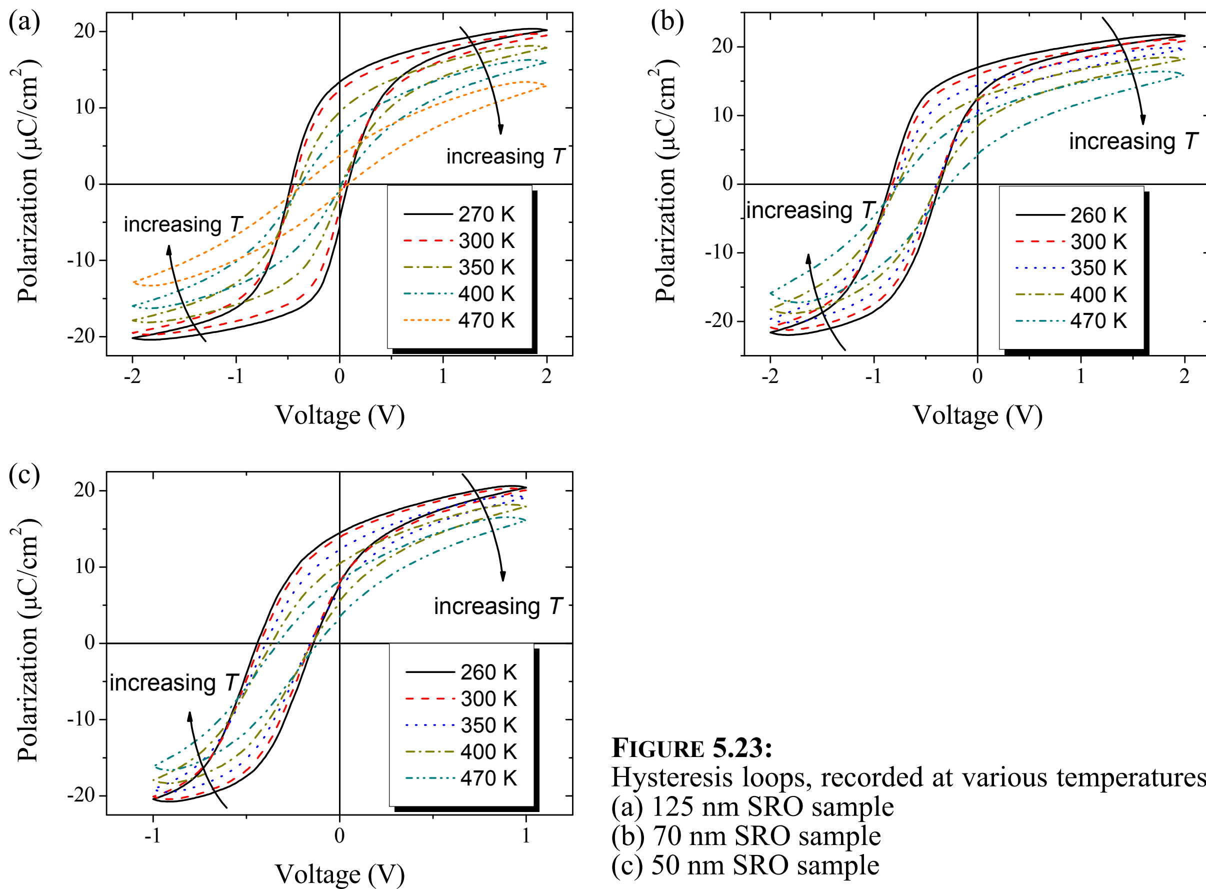

FIGURE 5.23:
Hysteresis loops, recorded at various temperatures:
(a) 125 nm SRO sample
(b) 70 nm SRO sample
(c) 50 nm SRO sample

ranges at only 0.28 F/m^2 (see Figure 5.18). From the literature (Refs. 12-18 and 84-90), the highest values reported at similar conditions are 0.2 F/m^2.

- The RT bulk permittivity from the thickness series (cmp. Figure 5.6 and Figure 5.9) can be evaluated as 3740 for SRO and 4560 for the Pt samples. This seems surprising, since a higher permittivity would have been expected for SRO than for Pt, but can be explained by the difference in the phase transition temperature of the Pt and SRO samples. The corresponding values from the literature (Refs. 12-18 and 84-90) do not exceed a RT bulk permittivity of 1000.
- The phase transition temperature becomes thickness dependent in both sample series with an increase of T_C for decreasing film thickness. For Pt, the bulk permittivity and also that of the thickest sample (130 nm) can be determined to 310 K, which is the same as determined in Ref. 64 for bulk crystals. For the SRO sample, a slightly higher phase transition temperature (compared to the bulk crystals) of T_C = 350 K can be found. In general, the temperature dependence of the permittivity reveals distinctive ferroelectric-to-paraelectric phase transitions for the thickest samples in both series.
- The loss tangent for both sample series can be observed in a wide temperature range to be well below 0.1, while for the Pt samples the value finally increases with increasing temperatures, similar as it was displayed in Ref. 17.
- From polarization-voltage loops a clear evidence of ferroelectricity at RT and temperatures above can be found for the thicker samples in both series, which so far has not been reported before. The RT values of the remanent polarization can be determined as 10 μC/cm^2 (125 nm BST) for the SRO samples and 3 μC/cm^2 (130 nm BST) for the Pt samples. The polarization values of the SRO show the trend to increase with increasing thickness, whereas the Pt samples display an inverted thickness dependence. Both series show a second order phase transition, e.g. no exact transition temperature can be determined from the temperature dependence of the remanent polarization.
- In general, the system SRO/BST/SRO on STO results in higher overall permittivity values compared to SRO/BST/Pt (~ 2 times higher) at comparable thicknesses, while the dielectric loss can be determined to approximately the same low (< 0.1) values. Also, the paraelectric

to ferroelectric phase transition in the SRO samples is shifted to higher temperatures compared to the Pt samples. The interface capacitance values around RT found for the SRO samples are by a factor of ~4-6 higher in comparison to Pt. Finally, the ferroelectric hysteresis loops show that the SRO samples show higher polarization values and a smaller amount of leakage current compared to Pt samples at the same temperature.

From the validation of the experimental results it follows, that although both sample series show dielectric properties mostly exceeding what has been reported for comparable systems up to now, the samples with SRO top electrode still show a superior behavior compared to the (likewise excellent) samples with Pt top electrodes.

6 Discussion

In this chapter, the following main observations will be discussed:

- Measured permittivity and phase transition temperature depending on the excitation voltage.
- Phase transition temperature and their different trends in SRO and Pt samples depending on the film thickness
- General differences of the permittivity between SRO and Pt samples

6.1 Influences from the Measurement Voltage Level

The analysis in chapter 5.2.1 exhibits that there is a strong influence of the excitation voltage amplitude V_{AC} on the small signal capacitance for measurements at the SRO samples, while its influence is less critical for the Pt samples. An extensive analysis of the impact of the chosen excitation voltage amplitude on the resulting (measured) capacitance is displayed in Figure 6.1. Here, the so called “permittivity gain” $\varepsilon/\varepsilon|_{10\ \mathrm{mV}}$ of a 130 nm Pt sample (Figure 6.1 (a)) and a 125 nm SRO sample (Figure 6.1 (b)) is presented with the temperature as an additional parameter. It can be noticed that the ratio between the measured capacitance with higher and that with lower (10 mV) excitation voltage of the Pt sample does not exceed

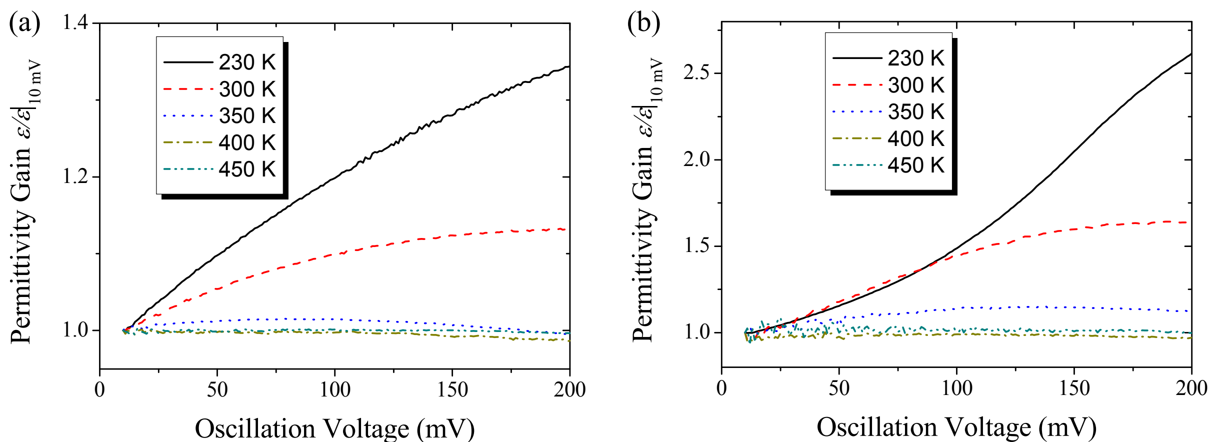

FIGURE 6.1:
Dependence of the permittivity @10 kHz on the applied excitation voltage level for different temperatures, normalized to the particular 10 mV permittivity
(a) Pt sample with 130 nm BST
(b) SRO sample with 125 nm BST

1.4 in the case of the lowest temperature and decreases further with higher temperature. In contrast, this ratio reaches values as high as 2.6 (and probably even higher) in the case of the SRO samples at the lowest temperatures, meaning that the (apparent) permittivity shows a pronounced increase with increasing oscillation voltage levels. Again, this ratio decreases when the temperature is raised, but is found to be significantly > 1 even at elevated temperatures as high as 350 K. From plots similar to those presented in Figure 6.1, the temperature dependence of the permittivity with the amplitude of the excitation field (instead of the voltage) as an additional parameter can be derived. These permittivity values for the 130 nm Pt sample and the 125 nm SRO sample are shown in Figure 6.2 (a) and Figure 6.2 (b). Both plots show an increase of the permittivity with increasing AC field as well as a decrease of the temperature of the maximum permittivity T_m with increasing E_{AC}. The evolution of T_m as a function of the ex-

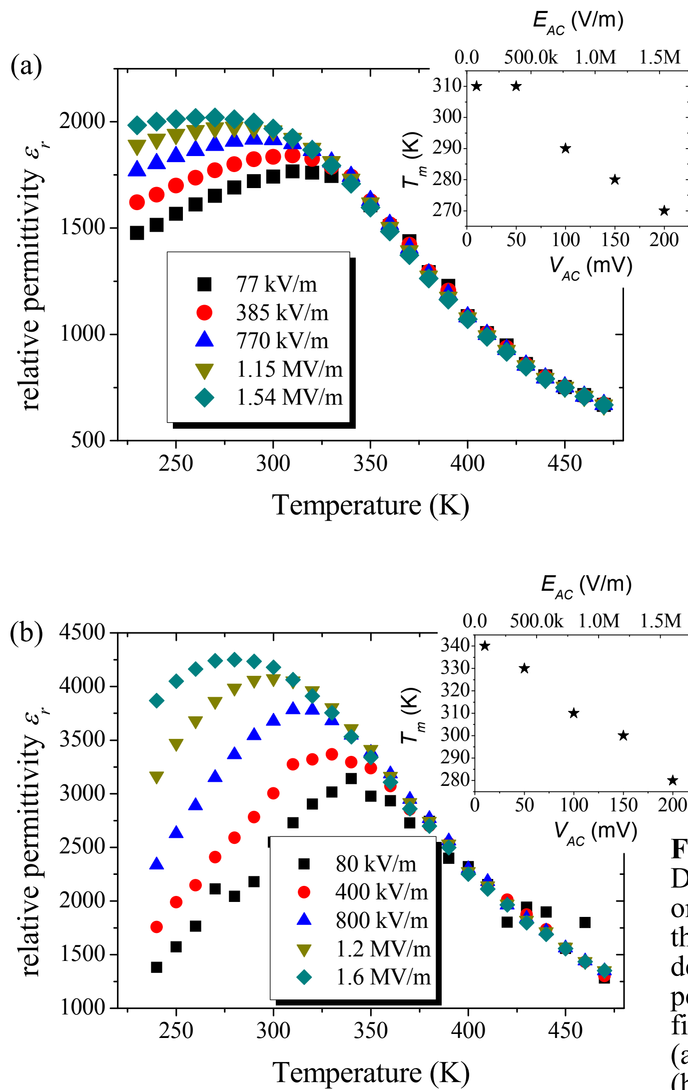

FIGURE 6.2:
Dependence of the permittivity @10 kHz on the temperature, for varying levels of the excitation field. Insets show the dependence of the temperature with maximum permittivity on the excitation voltage and field respectively.
(a) Pt sample with 130 nm BST
(b) SRO sample with 125 nm BST

citation field (and voltage) can be found in the insets of each plot. In general, the SRO sample displays a more pronounced increase of the permittivity and a stronger shift of the maximum temperature with increasing V_{AC} level in comparison to the Pt sample.

The general dependence of the permittivity on the amplitude of the alternating field E_{AC} can be fitted to simple polynomials (first and second order), as it was reported for BST thin film capacitors by Tyunina et al. [134]. For normal ferroelectrics, the linear dependence is dominated by the contribution from the domain wall motion [135] and can be described as $\varepsilon_r = \varepsilon_\alpha + \alpha E_{AC}$. In certain cases, however, a square dependence can be expected [136], so that the permittivity can be found as $\varepsilon_r = \varepsilon_\beta + \beta(E_{AC})^2$. This i.e. has been observed for relaxor ferroelectrics, which are discussed in detail in Ref. 137-139 (and references therein).

Figure 6.3 shows the permittivity depending on the excitation field E_{AC} measured at 230 K for the Pt and SRO sample (open symbols) as well as the corresponding polynomial fits (solid lines). The initial part of the $\varepsilon(E_{AC})$ curve resulting for the Pt sample can be best fitted linearly, resulting in fit parameters of $\varepsilon_\alpha = 1439$ and $\alpha = 4.8 \cdot 10^{-4}$ m/V. In the case of SRO samples, an even better fit can be achieved using a second order polynomial with $\beta = 1564$ and $\varepsilon_\beta = 1.08 \cdot 10^{-9}$ m^2/V^2.

A change of the top electrode would not convert a normal ferroelectric material into a relaxor type or vice versa. Instead, an investigation of the applied and effective field according to Ref. 140 will help to understand the differences. Therefore, the simple sketch of a capacitor as shown in Figure 6.4, divided in its particular elements should be examined. Here, the voltage

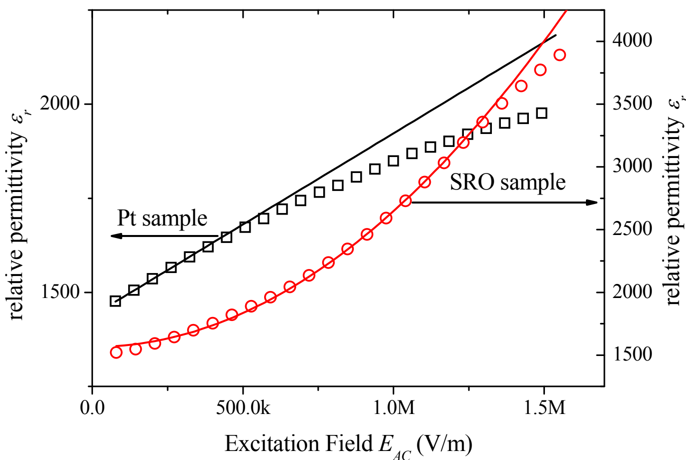

FIGURE 6.3: Field dependent permittivity measured at 230 K and 10 kHz (open symbols) and the corresponding polynomial fits (1st and 2nd order, solid lines).

V_t (which corresponds to a field E_t) is applied across the total capacitance C_t with its permittivity ε_t. This capacitance can be divided into the bulk capacitance C_b with its bulk permittivity ε_b and the interface capacitance C_i with its interface permittivity ε_i. The corresponding partial voltages are V_b and V_i, resulting in fields E_b and E_i. Simple equations have been deduced that relate the permittivities and the involved fields. For the total permittivity, one finds

$$\frac{1}{\varepsilon_t} \approx \frac{1}{\varepsilon_b} + \frac{1}{\varepsilon_{in}}, \tag{6.1}$$

where $\varepsilon_{in} = \varepsilon_i t / t_i = c_i t / \varepsilon_0$ describes the interface contribution to ε_t with the interface permittivity, thickness and capacitance density ε_i, t_i and c_i as well as the total thickness t. The effective field across the bulk capacitance can be evaluated as

$$E_b \approx E_t \left[1 - \frac{\varepsilon_t}{\varepsilon_{in}}\right]. \tag{6.2}$$

With these two equations, the effective bulk permittivity can be plotted as a function of the effective field across the bulk. As it is known from chapter 5.2.1, the value derived for c_i is dependent on the applied AC voltage mostly in the lower temperature region. However, for simplicity reasons the calculations here were done with fixed values of c_i that have been determined for the 10 mV case, i.e. $c_{i,\,\mathrm{Pt}} = 0.22\ \mathrm{F/m^2}$ and $c_{i,\,\mathrm{SRO}} = 1.15\ \mathrm{F/m^2}$ for a temperature of 230 K. For the 130 nm Pt sample as shown in Figure 6.5 (a), this reveals a few remarkable findings: The effective field across the bulk capacitance is drastically lowered compared to the applied field on the total sample. This is understandable when considering Figure 6.4 as a capacitive voltage divider with a low interface capacitance C_i compared to the higher bulk capacitance C_b. Moreover, the uncovered bulk permittivity now becomes highly dependent on the real applied field E_b with values starting at ~2700 at about 40 kV/m reaching high values of

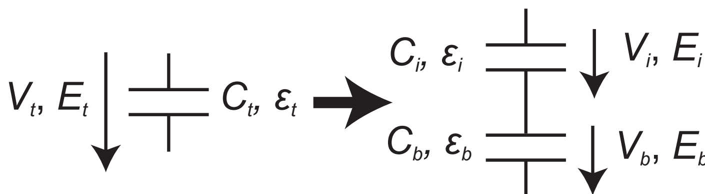

FIGURE 6.4: Schematic of the total capacitor with the applied field and voltage and the idealized splitting into interface and bulk capacitor with the corresponding fields and voltages

~5200 at about 590 kV/m. In general, the ε_b vs. E_b curve has a slight concave shape that may hint on the recovered relaxor properties of the true bulk material, although a square fit would not be perfectly suitable. As can be found in Figure 6.5 (b), the higher interface capacitance of SRO leads to a higher voltage drop across the bulk capacitor, which means higher effective fields than for the Pt samples. The shape of the ε_b vs. E_b curve for the SRO sample becomes more concave, so that a squared fit would be suitable. Interestingly, the achieved maximum permittivity is approximately the same as determined for the Pt sample, while the necessary amplitude of the effective field is more than twice that of the Pt value. In principle, this can be understood when taking a look on the general temperature dependence of the bulk permittivities of the Pt and SRO samples (Figure 5.13 (a) and Figure 5.17 (a)): Due to the different phase transition temperatures of the bulk ($T_{C,Pt}$ = 310 K vs. $T_{C,SRO}$ = 350 K) and the more pronounced peak of the $\varepsilon_{b,SRO}$ vs. T curve, the bulk permittivity determined for Pt samples shows higher values at lower temperatures compared to the SRO samples.

The general idea of relaxor properties in the BST thin films seems to be confirmed in both sample series, even if a full recovery of the relaxorlike behavior of the bulk permittivity in the case of the Pt samples is not possible. The suppression of the permittivity gain as seen from the measurements of the Pt samples is understandable when considering the low interface permittivity that leads to a strong voltage drop across the interface capacitance. From these consider-

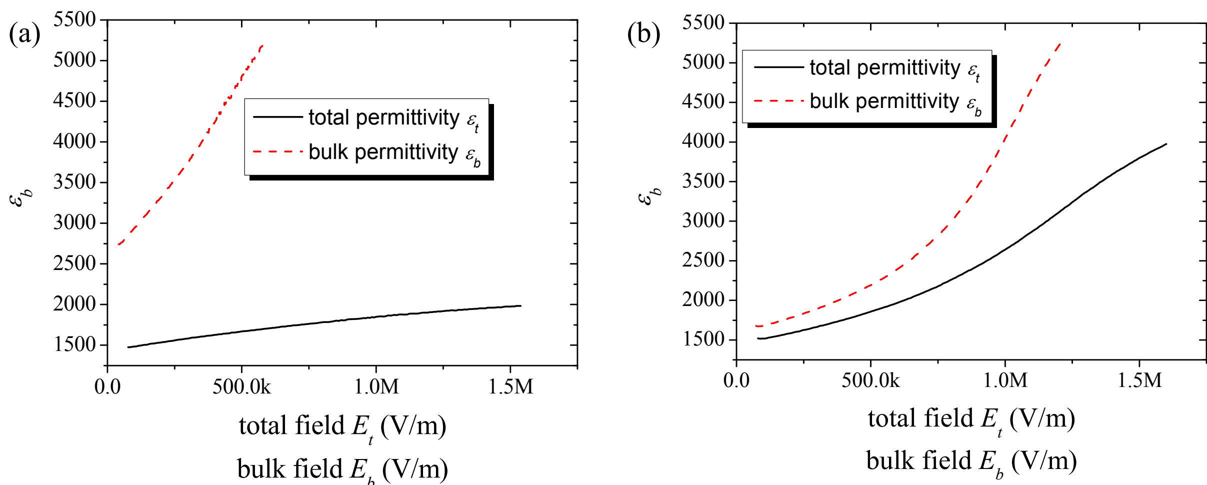

FIGURE 6.5:
Measured total permittivity and calculated effective bulk permittivity with the corresponding applied and effective fields
(a) 130 nm Pt sample
(b) 125 nm SRO sample

ations it becomes obvious that the amount of the true effective field that is applied on the true bulk permittivity strongly depends on the value of the interface capacitance.

To determine the frequency dependence of the permittivity (and thus to further examine the samples under the light of relaxors), corresponding measurements have also been performed for the samples investigated in this work, while the resulting ε_r vs. f plots can be found in Figure 6.6: For the 130 nm Pt sample only a moderate dependence of the permittivity on the used measurement frequency for all temperatures (Figure 6.6 (a)) can be seen, whereas the dispersion in the case of the SRO sample is more pronounced (Figure 6.6 (b)). The stronger decrease of the permittivity of the Pt-sample at frequencies above 100 kHz may result from the higher capacitance of the investigated capacitor (~1.2 nF for a contact pad with 10,000 μm^2) in contrast to the used SRO capacitor (~0.2 nF for a contact pad with 900 μm^2), which results in a higher RC time constant and a lower cut-off frequency.

From the plots shown in Figure 6.6 the temperature dependent permittivity has been plotted into Figure 6.7 with the measurement frequency as an additional parameter. It is obvious that for both investigated samples the permittivity becomes frequency independent in the high temperature region (above 350 K for the Pt sample and above 400 K for the SRO sample). In the lower temperature region a frequency dispersion can be found, which is more pronounced in the SRO and less visible for the Pt sample. In general, the temperature of the maximum permit-

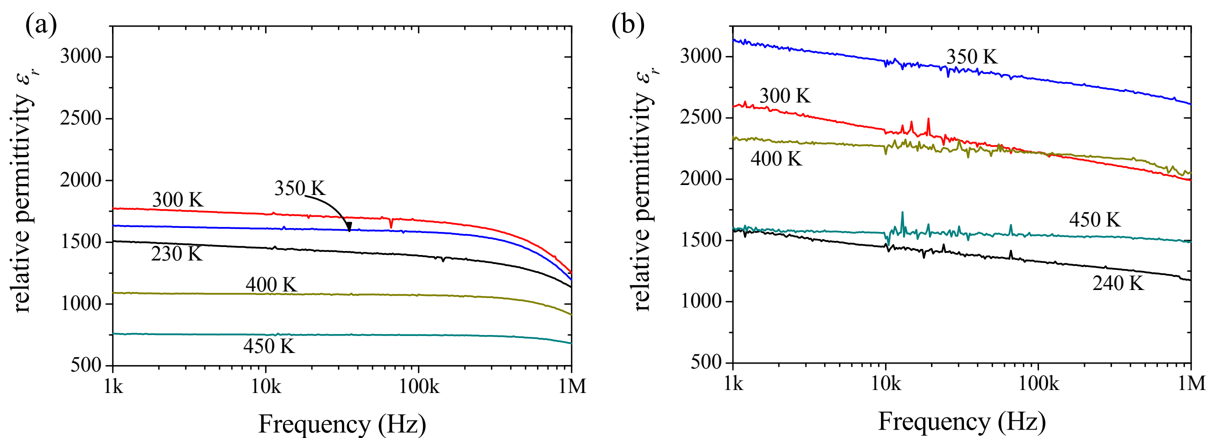

FIGURE 6.6:
Frequency dependence of the permittivity with the temperature as an additional parameter, measured at V_{AC} = 10mV
(a) Pt sample with 130 nm BST
(b) SRO sample with 125 nm BST

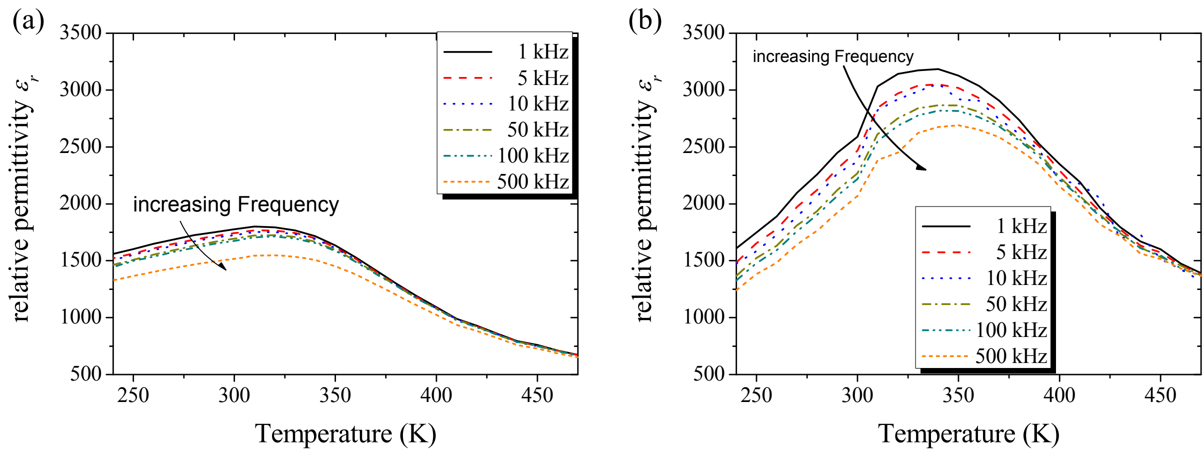

FIGURE 6.7:
Dependence of the permittivity @10 mV on the temperature, for varying measurement frequencies.
(a) Pt sample with 130 nm BST
(b) SRO sample with 125 nm BST

tivity T_m does not shift strongly for either sample and can be determined for Pt to 310 K (1 - 10 kHz) and 320 K (50 - 500 kHz) and for SRO to 340 K (1 - 50 kHz) and 350 K (100 and 500 kHz). From the observed frequency dependence of the permittivity it seems to be justified to attribute certain properties of the BST samples investigated in this work to relaxor phenomena. This behavior is more pronounced in the case of SRO samples and becomes obscured for the Pt samples due to their lower interface capacitance values which also may be caused by extrinsic influences such as interface amorphization.

The above considerations as well as the results of the polarization loops and capacitance – voltage curves (with the corresponding dielectric loss) indeed support the assumption of a coexistence of ferroelectric and relaxor properties also in the samples in this work. In detail, the following has been found:

- The samples here do not show polarization loops of square shape, as one would expect for ferroelectrics, but rather display so-called slim loops with a slanted gradient in the region near the coercive field typically for relaxor ferroelectrics (see Figure 5.20 & Figure 5.22).

- The temperature dependent remanent polarization P_r measured for both sample series, as shown in Figure 6.8, does not vanish at the corresponding phase transition temperature T_C, as one would expect from ferroelectrics. Instead, it decreases smoothly through the dynamic transition temperature T_m due to the fact that polar nanodomains (caused by inhomogeneous

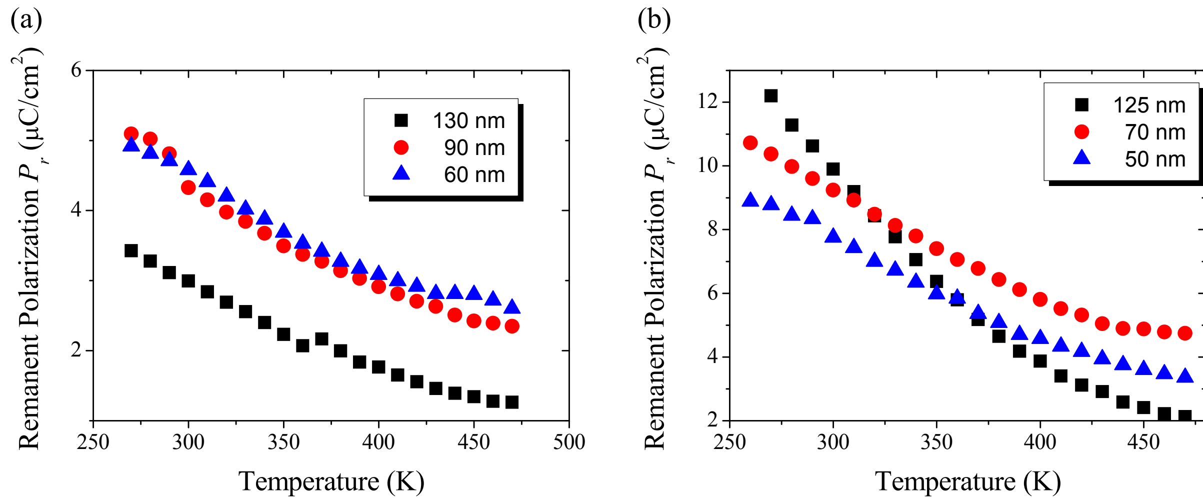

FIGURE 6.8:
Temperature dependence of the remanent polarization P_r from samples with different thicknesses, extracted from the measured polarization hysteresis loops.
(a) Pt samples
(b) SRO samples

distributions of the Sr and Ba atoms in the BST lattice) persist even at the highest temperature, which is typically for relaxors.

- The dielectric permittivity does not show a sharp and narrow peak at T_C (FWHM ≈ 10 - 20 K) independent of the measurement frequency (in the audio range), but rather exhibits a very broad peak and a strong frequency dispersion in their absolute value and (small but noticeable) their maximum position (T_m) (see Figure 6.7).
- The dissipation factor tan(δ) is rather high (~10%) compared to what could be expected for "good" ferroelectrics (<1%)

The origin of the strong dependence of the permittivity on the excitation voltage level V_{AC} can be related to the BST relaxorlike properties, which are strongly suppressed for the Pt samples, as shown above. The different trends of the thickness dependent phase transition temperature in the two different sample series at varying excitation levels will be discussed in the following: Figure 6.9 shows the permittivity as a function of the applied electrical *field* E_{AC} for the samples measured at 230 K and 10 kHz. Here, markers have been added to identify the values of equal excitation voltage (10, 50, 100, 150, and 200 mV). As one can see, the absolute deviation of the applied field at equal driving voltage becomes larger for larger fields, so that a comparison of the permittivity of samples with different thickness for higher excitation levels

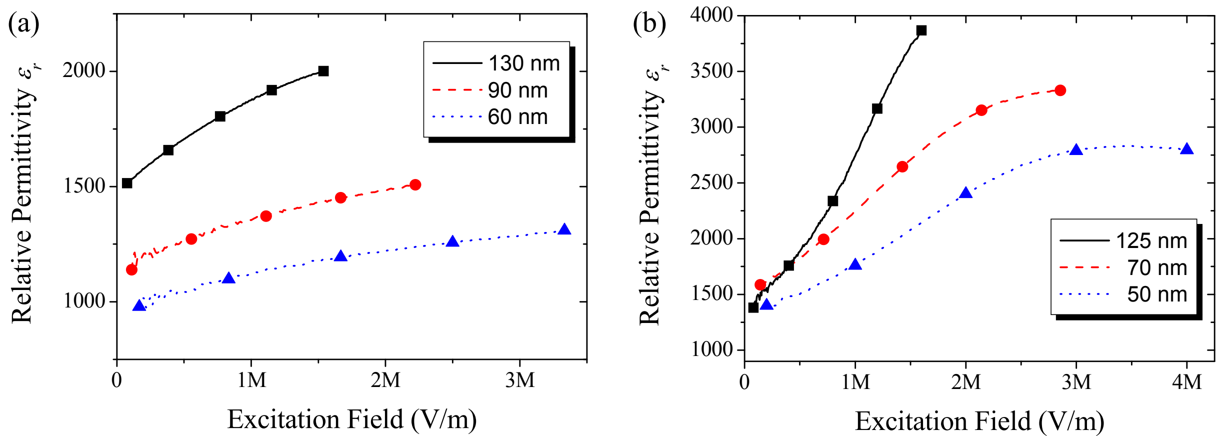

FIGURE 6.9:
Permittivity of samples with different BST thickness dependent on the excitation field, measured at 230 K and using a frequency of 10 kHz. Symbols mark the driving voltages 10, 50, 100, 150, and 200 mV from left to right
(a) Pt samples
(b) SRO samples

should be done at the same field, not the same voltage, as it was done in Figure 6.10. Here, similar to what is shown in Figure 6.2, for each sample (125, 70, and 50 nm BST thickness) the shift of T_m with increasing excitation field has been determined within the given measurement accuracy as approx. 20 – 30 K and can thus be regarded as thickness independent. In detail, the analyses have been performed at E_{AC} levels of 200 kV/m, 1 MV/m, and 1.6 MV/m, which require driving voltages of 25, 125, and 200 mV for the 125 nm sample, 14, 70, and 112 mV for the 70 nm sample and finally 10, 50 and 80 mV for the 50 nm sample. This result means that in contrast to what has been shown in Figure 5.16 (a), one can now conclude that applying higher AC fields on the samples will lead to uniform shifts of the phase transition by the same amount of temperature for each thickness and does not invert the general trend of decreasing temperatures of the maximum permittivity with increasing BST thickness. Considering Pt samples, the use of constant excitation fields instead of constant excitation voltages should not make a serious difference as the constant trend of T_m in Figure 5.12 predicts. This can be explained with the fact that in these samples the relaxorlike properties are suppressed because of the lower interface capacitance values.

Concluding this subchapter, the following should be noted:

The phase transition temperature as a thickness independent material parameter becomes thickness dependent in thinner BST films with increasing T_C values for decreasing BST thick-

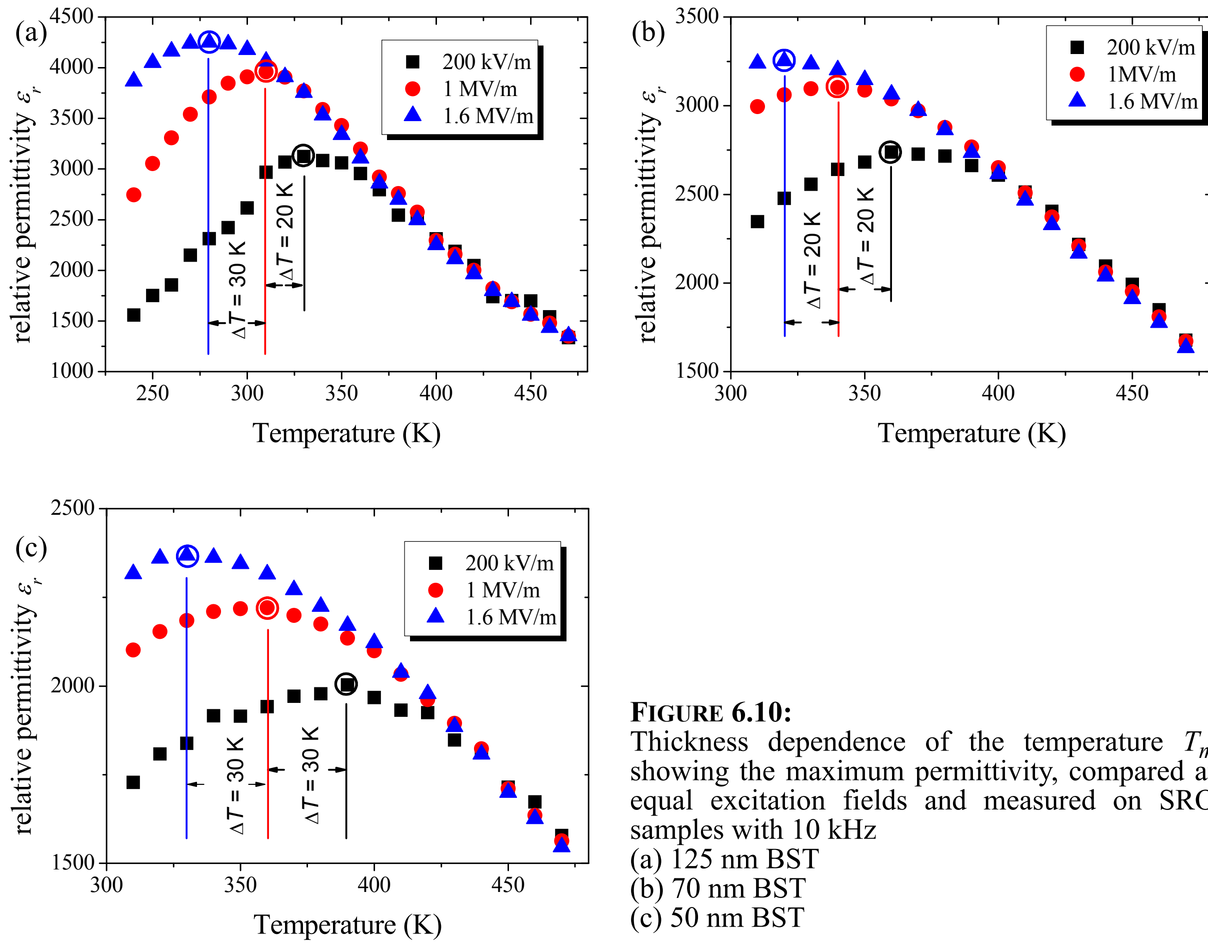

Figure 6.10:
Thickness dependence of the temperature T_m showing the maximum permittivity, compared at equal excitation fields and measured on SRO samples with 10 kHz
(a) 125 nm BST
(b) 70 nm BST
(c) 50 nm BST

ness. Mechanisms responsible for this behavior will be explained in the following sub-chapters. By choosing equal excitation voltage levels when measuring the permittivity of a thickness series of thin film capacitors with relaxorlike properties (such as the SRO samples in this work), an additional, now counteracting apparent thickness dependence may cancel the overall temperature dependence of the phase transition. When applying equal excitation fields instead of equal voltages, this apparent counteracting thickness dependence disappears and the overall trend of T_m (or T_C) remains independent of the level of E_{AC}. There exist publications, where a decrease of the phase transition with decreasing film thickness has been reported [17,96]. In Ref. 17, the excitation field has been kept constant at 650kV/m, which can be regarded as a suitable measurement parameter. Nevertheless, there must be additional influences from mechanisms that result in an apparent decrease of the phase transition temperature with decreasing film thickness, which will be explained in the next sub-chapters. The authors of Ref. 15 performed an initial comparison of the CV-curves for excitation voltage levels of 0.01,

0.05, and 0.1 V, where they did not find any difference in the temperature range from RT up to 473 K. This is understandable, since their samples are paraelectric in that temperature region and a possible relaxorlike behavior will not show up. In Ref. 96, no information about the used measurement parameters is given, so it is only speculative whether constant AC voltages could be responsible for the observed trend of the phase transition.

Finally, for any further interpretation only the achieved values and parameters of the measurements at low excitation voltage levels will be considered.

6.2 Strain Effects

From the considerations in chapter 2.4 it is obvious that the misfit strain inside heteroepitaxial films can be controlled by the choice of the underlying substrate material. Additionally, by variations of the film thickness the internal strain state can be altered by the introduction of misfit dislocations at the growth temperature T_g. It is widely accepted that the generation of misfit dislocations in perovskite films occurs only at T_g, because the dislocation glide must be suppressed at $T \ll T_g \sim 700°\ \mathrm{C}$ due to relatively high Peierls[8] barriers. From Ref. 73, the thickness dependent dislocation density ρ can be calculated as

$$\rho(t) = \eta S_m^0(T_g)(1 - t_c/t), \tag{6.3}$$

with t_c as the critical thickness below which no misfit dislocations will be generated and η as a factor which makes it possible that the equilibrium dislocation density is not reached due to kinetic reasons ($\eta \leq 1$). Eq. (2.8) together with Eq. (6.3) leads to

$$S_m(T, t) = \frac{b(1-\rho) - a_0}{a_0} = \frac{b}{a_0} - 1 + \frac{b}{a_0}\eta S_m^0(T_g)(1 - t_c/t), \tag{6.4}$$

8. To maintain the motion of a dislocation through a periodical potential (such as a crystal lattice), a force called the *Peierls force* is required [141].

which can be easily converted to

$$S_m(T, t) = S_m^{\infty}(T) + \eta S_m^0(T_g)\frac{t_c}{t}, \tag{6.5}$$

describing the temperature and thickness dependent strain in the films. Here, $S_m^{\infty}(T) = S_m^0(T) - \eta S_m(T_g)$ represents the in-plane strains S_1 and S_2 in a very thick film $(t \gg t_c)$, which would be fully relaxed at T_g under equilibrium conditions ($\eta = 1$). The temperature dependence of $S_m^{\infty}(T)$ may be described in a first approximation by a linear relation

$$S_m^{\infty}(T) \approx (1 - \eta)S_m^0(T_g) + (\alpha_b - \alpha_0)(T - T_g), \tag{6.6}$$

where α_b and α_0 are the thermal expansion coefficients of the substrate and the paraelectric film, respectively.

Eq. (2.24) allows the evaluation of the out-of-plane lattice strain according to Ref. 81 as

$$S_3 = \frac{c - a_0}{a_0} = -\frac{\partial G}{\partial \sigma_3} = \frac{2s_{12}S_m}{s_{11} + s_{12}} + \left[Q_{11} - \frac{2s_{12}Q_{12}}{s_{11} + s_{12}}\right]P_3^2, \tag{6.7}$$

with the material parameters as explained in chapter 2.4. With Eq. (6.7), the calculation of the strain-dependent out-of-plane lattice constant $c = a_0(S_3 + 1)$ can be done, using the following values and definitions:

- $S_m^0(T_g = 973\text{ K}) \approx -15 \cdot 10^{-3}$, $S_m^0(T = 300\text{ K}) \approx -12 \cdot 10^{-3}$ (strains were calculated using the data of lattice constants and thermal expansion coefficients of $BaTiO_3$, $SrTiO_3$, and SRO, cmp. Ref. 142)
- $\eta = 0.7$, determined using the experimental value of $S_m = (a - a_0)/a_0 \approx -2 \cdot 10^{-3}$, which was evaluated from the measured in-plane lattice constant $a \approx 0.397$ nm of a 200-nm BST film and the estimated prototypic-cell size $a_0(T = 300\text{ K}) \approx 0.3977$ nm
- $P_3^2 = -a_3^*/(2a_{33}^*)$ results from $\partial\tilde{G}/\partial P_3 = 0$ (using the P^4 approximation in Eq. (2.26))

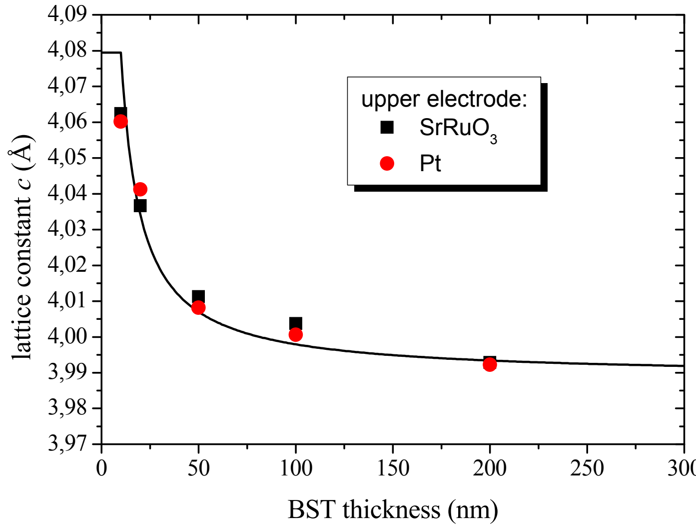

FIGURE 6.11: Measured out-of-plane lattice constants (symbols) and the corresponding calculated thickness dependence (solid line).

- $a_3^* = a_1 - 2S_m Q_{12}/(s_{11}+s_{12})$, $a_{33}^* = a_{11} + Q_{12}^2/(s_{11}+s_{12})$
- $a_1 = 3.83 \cdot 10^6$ Vm/As (evaluated from the data given in Ref. 64), $a_{11} = 1.767 \cdot 10^8$ m^5/C^2F
- $s_{11} = 5.9 \cdot 10^{-12}$ m^2/N, $s_{12} = -1.9 \cdot 10^{-12}$ m^2/N
- $Q_{11} = 0.10$ m^4/C^2, $Q_{12} = -0.0346$ m^4/C^2 (these values were calculated by linear interpolation of the $BaTiO_3$ and $SrTiO_3$ parameters given in Refs. 75 and 143)

With all of the above equations and values the resulting thickness dependence $c(t)$ of the out-of-plane lattice constant could be calculated, which has been plotted in Figure 6.11 together with the values measured by XRD. It can be seen that the curve found in this way is in a good agreement with the experimentally determined values, which supports the validity of Eq. (6.5).

Paraelectric State

Eq. (6.5) can be substituted into the Curie-Weiss-type law of the permittivity depending on strain, which in the paraelectric regime has been introduced in Eq. (2.31) as,

$$\varepsilon = \frac{\varepsilon_0 K_s}{S_m - S_m^*}. \tag{6.8}$$

This leads to the following relation for the reciprocal permittivity of a paraelectric film:

$$\frac{1}{\varepsilon(T,t)} = \frac{1}{\varepsilon^{\infty}(T)} + \eta\frac{S_m^0(T_g)t_c}{\varepsilon_0 K_s}\frac{t_c}{t}. \tag{6.9}$$

Here, $\varepsilon^{\infty}(T) = \varepsilon_0 K_s/(S_m^{\infty}(T) - S_m^*(T))$ describes the permittivity of a very thick strained BST film $(t \gg t_c)$, while Eq. (6.9) itself shows that the intrinsic reciprocal permittivity is linear dependent on the reciprocal film thickness t^{-1}. It can be seen that depending on the sign of $S_m^0(T_g)$, the permittivity of the paraelectric film either increases or decreases with increasing thickness. From Eq. (6.9) the reciprocal capacitance density (at $t > t_c$) can be evaluated as

$$\frac{1}{c_{eff}} = \frac{t}{\varepsilon} + \eta\frac{S_m^0(T_g)t_c}{\varepsilon_0 K_s}. \tag{6.10}$$

From the extrapolation of c_{eff}^{-1} to zero thickness, a nonzero intercept results which is caused by the strain relaxation. This intercept can be negative (for compressive in-plane film strains, $S_m^0(T_g) < 0$) or positive (for tensile in-plane film strains, $S_m^0(T_g) > 0$), which should be kept in mind as a noteworthy result.

Ferroelectric Regime

Considering epitaxial films in their ferroelectric state, a tetragonal *c*-phase with the out-of-plane spontaneous polarization $(P_1 = P_2 = 0,\ P_3 \neq 0)$ can be found. The dependence of the permittivity ε on the misfit strain in the ferroelectric case can be described again using a Curie-Weiss type law as

$$\varepsilon = \frac{\varepsilon_0 K_{sc}}{S_m^* - S_m}, \tag{6.11}$$

since near the second-order phase transition the P^4 approximation is valid [91]. In contrast to the paraelectric case (Eq. (6.8)), here the lattice strains must be $S_m < S_m^*$ and the parameter describing the sensitivity of the permittivity on the strain can be found as $K_{sc} = K_s/2$, which shows analogy to what has been found in Eq. (2.18) and Eq. (2.23) for the pre-factor above and

below the phase transition temperature.

Eq. (6.5), which has been validated according to Figure 6.11, can now be substituted into Eq. (2.31), leading to an equation describing the intrinsic reciprocal permittivity dependent on thickness and temperature (in analogy to the above discussed paraelectric case):

$$\frac{1}{\varepsilon(T,t)} = \frac{1}{\varepsilon^{\infty}(T)} - \eta\frac{S_m^0(T_g)t_c}{\varepsilon_0 K_{sc}}\frac{}{t}. \quad (6.12)$$

Accordingly, $\varepsilon^{\infty}(T) = \varepsilon_0 K_{sc}/(S_m^*(T) - S_m^{\infty}(T))$ describes the permittivity of a very thick strained BST film ($t \gg t_c$), while the thickness dependent term in Eq. (6.12) differs from that in Eq. (6.9) by the negative sign and the two times larger amplitude. In analogy to the paraelectric case in the previous sub-chapter, the thickness dependent reciprocal capacitance can be derived from Eq. (6.12) as

$$\frac{1}{c_{eff}} = \frac{t}{\varepsilon^{\infty}(T)} - \eta\frac{S_m^0(T_g)t_c}{\varepsilon_0 K_{sc}}. \quad (6.13)$$

In analogy to Eq. (6.10), Eq. (6.13) again appears as a linear equation in *t*, with the difference in the negative sign and a two times smaller pre-factor K_{sc} (compared to K_s)

Summary of the Strain Effects

Eq. (6.10) and Eq. (6.13) as the key results reveal the following aspects which are valid in both states (PE or FE):

- The slope of the dependence c_{eff}^{-1} reflects the permittivity ε^{∞} of a thick strained film, which does not correspond with the permittivity of the bulk material, ε_b.
- The extrapolation of the measured thickness dependence of the inverse capacitance to $t = 0$ may give a considerable nonzero intercept even when the interface effect is negligible $(c_i^{-1} \to 0)$.

Substitution of the numerical values for the involved parameters as given above into Eq. (6.10) and Eq. (6.13) results in apparent reciprocal interface capacitances of $c_i^{-1} = 0.9688\ \mathrm{m^2/F}$ in

the ferroelectric case and $c_i^{-1} = -0.4844\ \mathrm{m^2/F}$ in the paraelectric case. These values can be regarded as the theoretical limits of the intercept, solely defined by effects of the strain relaxation when no extrinsic influences have to be considered. It can be seen that the room temperature interface capacitance density determined in chapter 5.2.1 for SRO samples ($c_{i,SRO}^{-1} = 1.282\ \mathrm{m^2/F}$) is very close to that theoretical minimum for the ferroelectric case, while the value for Pt ($c_{i,Pt}^{-1} = 4.348\ \mathrm{m^2/F}$) is clearly higher. As shown above, depending on the state of the material (ferro- or paraelectric) the strain contribution of the interface capacitance may have a negative sign. This in combination with additional contributions to the interface capacitance can lead to a reduction of the total interface capacitance density, as will be shown in the following chapters.

To conclude this sub-chapter, it must be stressed that the increase of T_C (compared to the bulk ceramics) measured with the "correct" excitation voltage of $V_{AC} = 10$ mV, can be explained by the strain effect as well. Indeed, the thermodynamic considerations from chapter 2.5 predict

$$T_C = T_0 + S_m 4\varepsilon_0 C \frac{Q_{12}}{(s_{11}+s_{12})}, \tag{6.14}$$

with T_0 and C as the Curie-Weiss temperature and constant of the bulk material, respectively. Taking $T_0 = 290$ K, $C = 1.18 \cdot 10^5$ K (Ref. 64), Q_{12}, s_{11} and s_{12} as mentioned above and by calculating $S_m = (a - a_0)/a_0$ via the thickness dependence of the in-plane lattice constant $a = \sqrt{a_0^3/c}$, a thickness dependent phase transition temperature results as shown in Figure 6.12 (solid line)[9]. The squared and round symbols in Figure 6.12 display the experimentally determined phase transition temperatures for the Pt and SRO samples (cmp. chapter 5.2.2) and show in principle a good agreement to the trend of the calculated phase transition temperature. It will be shown in the next chapter what might be responsible for the difference between the measured phase transition and that calculated using Eq. (6.14).

9. assuming a constant volume a_0^3 of the BST cell, with $a_0 = 0.3977$ Å as the estimated prototypic cell size

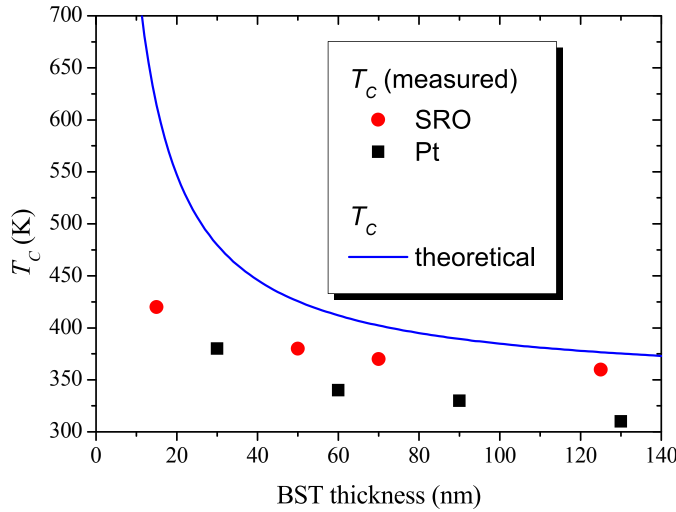

FIGURE 6.12: Phase transition temperature T_C (solid line), calculated using Eq. (6.14) and the experimentally determined values for SRO (round symbols) and Pt (squared symbols)

6.3 Depolarizing Fields and their Competition with Strain Effects

From the thickness dependence of the film out-of-plane lattice parameter *c,* determined by XRD, which fits to the same theoretical curve *c*(*t*) for both SRO and Pt samples (cmp. Figure 6.11), the conclusion follows that the BST strain state is insensitive to the material used for the top electrode. Therefore, the difference in the dielectric analysis between SRO and Pt cannot be attributed to the strain contribution described in the previous sub-chapter.

Another contribution to the thickness dependence results from the reduction of the applied electric field inside the film due to a finite screening length of the electrodes, as described in chapter 3. The room temperature single interface capacitance densities $c_{i,\,\mathrm{Pt}}\big|_{10\ \mathrm{mV}} = 0.277\ \mathrm{F/m^2}$ and $c_{i,\,\mathrm{SRO}}\big|_{10\ \mathrm{mV}} = 1.55\ \mathrm{F/m^2}$, as determined from Figure 5.18, result in values of the total capacitance density of $c_{i,\,total,\,\mathrm{Pt}}\big|_{10\ \mathrm{mV}} = 0.139\ \mathrm{F/m^2}$ for a Pt/BST/Pt system and $c_{i,\,total,\,\mathrm{SRO}}\big|_{10\ \mathrm{mV}} = 0.775\ \mathrm{F/m^2}$ for the SRO/BST/SRO system. In Ref. 31, the total capacitance density values have been evaluated using Eq. (3.5) and Eq. (3.6) as 0.25 F/m^2 for samples with Pt electrode and 0.9 F/m^2 for SRO samples as a theoretical limit for a finite interface capacitance that arises only from screening contributions. Whereas here the permittivity of the SRO electrode has been assumed as $\varepsilon_{SRO} \approx 100$, it has been measured in Ref. 108 using optical methods and was determined to be $\varepsilon_{SRO} \approx 8.45$. With this value, the maximum achievable capacitance density (considering only screening properties of the electrode) reduces to 0.257 F/m^2, so that only a small difference between SRO and Pt should be observable. As a result follows that the experimentally determined 0.775 F/m^2 are closer to the 0.9 F/m^2 than

the 0.257 F/m^2, which either means that the parameters for calculating the screening length of the SRO electrodes (permittivity, electron density, etc.) are chosen incorrectly (cmp. 3.2), or that a negative extrinsic contribution leads to a modified interface capacitance (as will be discussed later). From Ref. 33 however, the interface capacitance of the "intrinsic dead layer" has been determined to $c_i = 0,615$ F/m^2 which now fits considerably better with respect to the experimental 0.775 F/m^2.

Using a simple phenomenological model, the properties of strained ferroelectric capacitors have been analyzed. In contrast to the previous calculations [31], here it was taken into account that the electrode screening ability also affects the temperature T_C of the ferroelectric phase transition, which modifies the thickness dependence of the dielectric response additionally. The thermodynamic considerations now allow a better understanding of the differences found between Pt and SRO samples.

The interface between the ferroelectric film and the electrode can be characterized by assuming thin low permittivity layers (of intrinsic or extrinsic origins) with characteristics independent of the thickness of the film t. In chapter 3.2 it was shown how the electric fields of the ferroelectric film and these interfacial layers can be evaluated, resulting in a depolarizing field $E_{dep} \approx -P/(c_{int}t)$ that exists inside the ferroelectric (see Eq. (3.11)). Here, P is the out-of-plane polarization of the film, whereas all interface contributions (intrinsic as well as extrinsic influences) are summarized as: $c_{int} = (1/2)\varepsilon_0\varepsilon_d/d$. If variations of the ferroelectric polarization near the film surfaces are negligible, $d = \sqrt{\varepsilon_m} \cdot l_{TF} \ll t$ is the thickness of the interface layer with a low permittivity $\varepsilon_d = \varepsilon_m$, where l_{TF} and ε_m are the Thomas-Fermi screening length and the lattice dielectric constant of the electrode material, respectively [31].

In a recent publication of Pertsev et al., the influence of the depolarizing field has been discussed using a P^8 approximation [144]. The differentiation of the (then 8th order) film thermodynamic potential (cmp. Eq. (2.26)) leads to

$$2a_3^*P + 4a_{33}^*P^3 + 6a_{111}P^5 + 8a_{1111}P^7 + \ldots = E. \tag{6.15}$$

With the continuity condition for the electric displacement $D = \varepsilon_0 E + P$ and the electrostatic

potential at the interfaces, Eq. (6.15) can be rewritten as

$$2\left[a_3^* + \frac{1}{2(\varepsilon_0 + c_{int}t)}\right]P + 4a_{33}^*P^3 + 6a_{111}P^5 + 8a_{1111}P^7 + \ldots = -\frac{c_{int}}{(\varepsilon_0 + c_{int}t)}V. \tag{6.16}$$

Here, V is the voltage applied to the electrodes whereas E represents the total field inside the ferroelectric film, which is the algebraic sum of the applied field and the depolarizing field E_{dep}. Now, the total capacitance density $c_t = \partial D(V)/\partial V$ can be evaluated as

$$c_t = \frac{c_{int}}{(\varepsilon_0 + c_{int} \cdot t)}\left[\frac{\varepsilon_0}{t} + \frac{c_{int}}{1 + (\varepsilon_0 + c_{int} \cdot t)\chi^{-1}}\right], \tag{6.17}$$

where the inverse susceptibility of the ferroelectric film is represented by

$$\chi^{-1} = \partial E/\partial P = 2a_3^* + 12a_{33}^*P^2 + 30a_{111}P^4 + 56a_{1111}P^6 + \ldots$$

From the P^4 approximation the spontaneous polarization can be found as $P_s^2 \approx -[a_3^* + 1/(2c_it)]/(2a_{33}^*)$ and the reciprocal susceptibility may be evaluated as $\chi^{-1} \approx -4a_3^* - 3/(c_it)$. Now, the inverse of the total capacitance density can be written as

$$\frac{1}{c_t} \approx \chi^{-1}t + \frac{1}{c_{int}} = \frac{t}{\varepsilon^{\infty}} - \frac{2}{c_{int}}, \tag{6.18}$$

where ε^{∞} is the permittivity of a thick strained film, as mentioned in the above sections. As a remarkable result, Eq. (6.18) shows that the extrapolation of the inverse total capacitance $1/c_t$ to zero film thickness has a negative intercept. This is only valid for films in the ferroelectric state, while for paraelectric materials the standard result $c_t^{-1}(t \to 0) = 1/c_{int}$ follows.

In the P^6 and higher order approximations, the reciprocal total capacitance c_t^{-1} becomes non-linear, but it can be seen that the nonlinearity is usually negligible when plotting $c_t^{-1}(t)$ in the

limited thickness range $t_{min} \le t \le t_{max}$. This makes it possible to approximate the reciprocal capacitance density as

$$\frac{1}{c_t} \approx \frac{t}{\varepsilon_{eff}} - \frac{\kappa}{c_{int}}, \tag{6.19}$$

in analogy to Eq. (6.18) but with two fitting parameters ε_{eff} and κ. Remarkably, the extrapolation to zero thickness gives a negative intercept $-\kappa/c_{int}$, which may significantly vary with temperature.

The influence of both strain and depolarizing field effects on the phase transition temperature has been calculated in Ref. [144] as

$$T_C = T_0 + 4\frac{\varepsilon_0 C Q_{12}}{s_{11}+s_{12}} S_m^{\infty}(T_g) - \varepsilon_0 C\left[\frac{3}{2c_{int}} - 4\frac{Q_{12} t_c \eta}{s_{11}+s_{12}} S_m^0(T_g)\right]\frac{1}{t}, \tag{6.20}$$

where the thickness dependence of the misfit strain, given by Eq. (6.5), has been taken into account, while its weak temperature dependence described by Eq. (6.6) has been neglected. The thickness dependence of T_C can be thus determined by the difference between the two terms in square brackets in Eq. (6.20). While the first term is positive, the second one must be negative ($S_m^0 < 0$ and $Q_{12} < 0$), so that the variation of T_C is governed by the competition of the strain relaxation and the depolarizing-field effect, as already mentioned in chapter 6.3. When the latter prevails, the critical temperature is expected to decrease in thinner films. On the other hand, T_C will increase with decreasing thickness, if the dominant term in Eq. (6.20) is associated with the relaxation of compressive misfit strain. In addition to the thickness dependence of T_C solely from strain as shown in Figure 6.12, Figure 6.13 now shows the calculated thickness dependence of T_C when also the depolarizing field has been considered. It can be seen that these calculated values now much better fit the experimentally determined phase transition temperature both for the SRO as well as the Pt samples. For the calculation, c_{int} in Eq. (6.20) has been chosen to 0.7 F/m^2 for SRO and 0.45 F/m^2 for the Pt samples. These values are comparable to the theoretical value of $c_i = 0.615$ F/m^2 given in Ref. 33, hence this fitting parameter is confirmed by theory.

A reduction of T_C in thinner films has been observed in Au/$Ba_{0.5}Sr_{0.5}TiO_3$/$La_{0.5}Sr_{0.5}CoO_3$ and Pt/$Ba_{0.7}Sr_{0.3}TiO_3$/Pt thin-film capacitors [17,96]. As reported in Ref. 17, the samples have been fabricated as Si/Pt/BST, which does not lead to epitaxially grown films or an associated misfit strain relief, so only the depolarizing field effect may be found, which agrees with the trend of the thickness dependent phase transition temperature. At the same time, the dielectric-peak position T_m was found to shift to higher temperatures with decreasing thickness in Au/$Ba_{0.5}Sr_{0.5}TiO_3$/$SrRuO_3$ and Pt/$Ba_{0.7}Sr_{0.3}TiO_3$/$SrRuO_3$ capacitors [16,92], which can be attributed to the strain relaxation process in the epitaxial films. Both sample series investigated in this work, however, show the latter behavior, as can be seen in chapter 5.

The thickness dependence of the polarization and permittivity in thin ferroelectric films with $t > t_c$ is also affected by the competition of strain and depolarizing field effects. In the P^4 approximation, the reciprocal total capacitance density can be described by

$$\frac{1}{c_t} = \frac{t}{\varepsilon^{\infty}} - 2\left[\frac{1}{c_{int}} - 4\frac{Q_{12}t_c\eta}{s_{11}+s_{12}}S_m^0(T_g)\right]. \tag{6.21}$$

Eq. (6.21) demonstrates that the dependence $c_t^{-1}(t)$ remains linear, but the intercept is defined now by the algebraic sum of two terms with opposite sign. Evidently, the intercept becomes positive when the contribution due to strain relaxation is larger than the depolarizing-field contribution. The situation becomes reversed in the paraelectric state with $c_t^{-1}(t \to 0) \approx c_{int}^{-1} - 4Q_{12}t_c\eta S_m^0(T_g)/(s_{11}+s_{12})$. Remarkably, the intercept here becomes

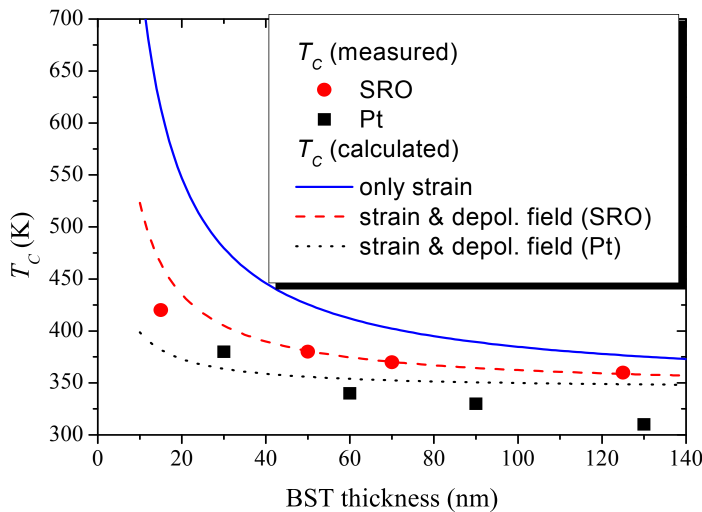

FIGURE 6.13:
Phase transition temperature T_C, calculated using Eq. (6.14) (solid line) and Eq. (6.20) (dashed and dotted line) as well as the experimentally determined values for SRO (round symbols) and Pt (squared symbols)

negative when the strain-related effect prevails over the depolarizing-field one.

6.4 Comparison with experimental Values

Whereas a change of the sign of the intercept has also been observed in the P^4 approximation, its temperature dependence could only be seen when using the P^8 approximation. With the above derived expressions for the reciprocal total capacitance density in the ferroelectric and paraelectric state, the intercept $c_t^{-1}(t \rightarrow 0)$ has been calculated for epitaxial BTO films, as shown in Figure 6.14. Here, two different cases were considered: (a) A capacitor with electrodes that show good screening properties, e.g. an assumed interface capacitance of c_{int} = 1 F/m^2 (Figure 6.14 (a)) and (b) a capacitor incorporating electrode material showing deteriorated screening properties, displayed here by an interface capacitance density of c_{int} = 0.2 F/m^2 (Figure 6.14 (b)). It can be observed that with both assumed interface capacitance values, a change of sign of $c_t^{-1}(t \rightarrow 0)$ occurs during the transition from the paraelectric to the ferroelectric phase. In the case of electrodes with good screening properties (higher interface capacitance density), the strain effect dominates, thus the sign of $c_t^{-1}(t \rightarrow 0)$ changes from positive in the ferroelectric phase to negative in the paraelectric phase. For the assumed electrodes with degraded screening properties (lower interface capacitance density), the depolarizing field ef-

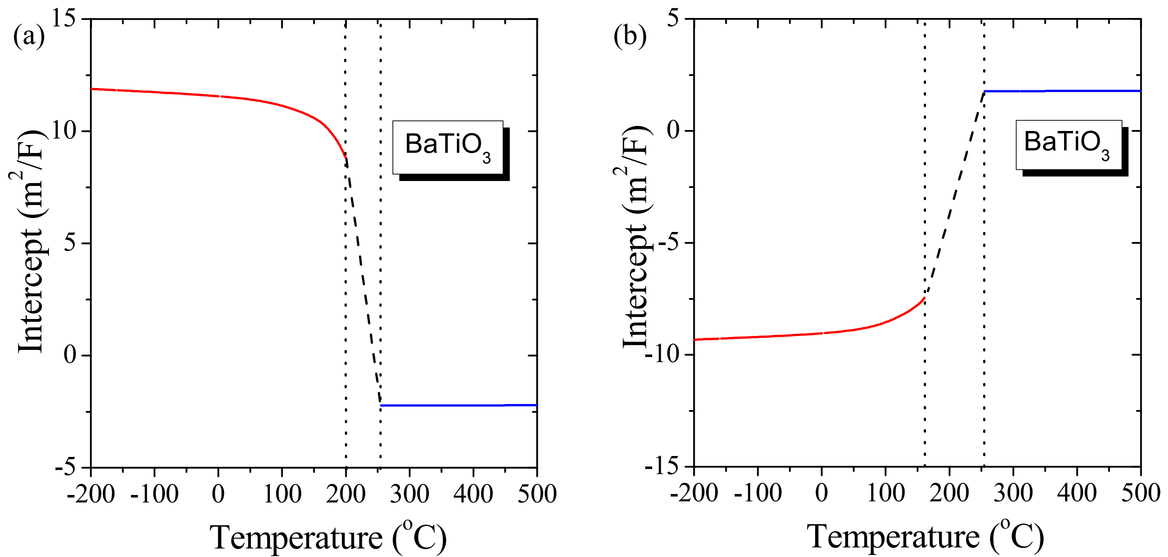

FIGURE 6.14:
Temperature dependence of intercept c_t^{-1} ($t \rightarrow 0$) calculated for $BaTiO_3$ thin-film capacitors with electrodes of different screening abilities.
(a) c_{int} = 1 F/m^2
(b) c_{int} = 0.2 F/m^2

fect overrides the influences of strain relaxation, resulting in a change of the sign of $c_t^{-1}(t \rightarrow 0)$ from negative in the ferroelectric phase to positive in the paraelectric phase.

When the temperature dependence of the intercept, as shown in Figure 6.14 is compared to the temperature dependent values resulting from measurements of the SRO and Pt samples in chapter 5 (cmp. Figure 5.13 & Figure 5.17), the following becomes obvious:

- In principle, the temperature dependence of the Pt samples (Figure 5.13) shows a very good agreement to the behavior of a capacitor with electrodes having good screening abilities (Figure 6.14 (a)), thus the strain relaxation effects dominate the intercept $c_t^{-1}(t \rightarrow 0)$.
- For the SRO samples, this temperature dependence (Figure 5.17) does not show the same good agreement as in the Pt case, but nevertheless can be regarded as qualitatively comparable. Hence, also here the strain relaxation effects dominate the capacitance density.

It follows from this comparison that only the theoretical approach incorporating electrodes with good screening properties can be confirmed by the experimental values. This is reasonable, since both sample series show the same strain state, as discussed in chapter 6.2 and do not differ much in the theoretical estimates of their interface capacitance density associated with the screening space charge in the electrodes which can be calculated using the results of Refs. 31 and 108.

6.5 Validation of the Theoretic Findings

To conclude this chapter, the results of the theoretical discussion about the experimentally achieved values will be summarized:

- It has been shown that the different trends of the thickness dependence of the phase transition temperature evaluated for the SRO and Pt samples can be solely explained by the influence of the excitation voltage levels. Using equal excitation fields rather then equal excitation voltages, no serious difference in the trend of the phase transition temperature for each thickness can be observed.
- In general, the BST layers investigated here show a relaxorlike dependence of the permittivity on the excitation amplitude, which in case of the Pt samples is obscured by the low inter-

face capacitance and the subsequently lower voltage drop across the bulk capacitor. From recalculations of the real applied field assuming a capacitive voltage divider, the relaxor properties in principle can be recovered. A microscopic interpretation concerning the relaxor properties in perovskites is given in Ref. 137 and Ref. 138. In the present case, an inhomogeneous distribution of STO and BTO in the BST-matrix can be assumed, that leads to nanodomains with long-range interaction.

- From the analysis of the out-of-plane lattice constant it can be found that both SRO and Pt samples are in the same thickness dependent strain state. The experimentally determined thickness dependence of the lattice constant can be evaluated theoretically by means of the thermodynamic theory.
- A thickness and strain dependent apparent interface capacitance could be evaluated by means of a Curie-Weiss type dependence of the permittivity on the lattice mismatch strain. The experimentally determined values in general show a good agreement with the thus calculated values. The shift of the phase transition temperature depending on the strain in the BST layer has been evaluated and reveals a fair agreement to what has been found experimentally.
- Additional effects from depolarizing fields compete with the strain effects, while their contributions to the apparent interface capacitance and the phase transition temperature have opposite signs. The measured values of the phase transition temperature agree much better with the calculated values when both strain *and* depolarizing fields are considered. Depending on the dominating effect the resulting apparent interface capacitance may be higher or lower and even can become negative. A comparison of the experimentally determined temperature dependence of the interface capacitance with the theoretically determined one revealed a good agreement with the case of electrodes with good screening abilities in both the SRO and Pt samples. In general, the depolarizing field is thought to be strongly dependent on the screening abilities of the used electrode, which seem to be better in the SRO case compared to the Pt case.
- Since theoretically both the strain effects and the depolarizing field result in apparent interface capacitance values of the same order of magnitude as observed experimentally, it

seems to be difficult to distinguish between both influences. The strain state in the two compared sample series was found to be identical, so that from the difference in the screening abilities of the electrode material a separation may be accomplished.

7 Conclusion

7.1 Summary

In the course of this work, high quality epitaxial $Ba_{0.7}Sr_{0.3}TiO_3$ (BST) thin films with $SrRuO_3$ (SRO) bottom electrodes have been fabricated on $SrTiO_3$ (STO) single crystalline substrates using the pulsed laser deposition (PLD) technology. SRO (epitaxial via PLD) as well as Pt (by sputter deposition) have been deposited on these bilayers to finally form BST thin film capacitors. These samples have been termed accordingly SRO samples and Pt samples.

Physical analyses approved the BST films to be single crystalline with smooth, defect-free interfaces to the electrode layers. From electrical analyses, small signal capacitance values as well as ferroelectric polarization loops of the samples have been determined at a variety of temperatures, voltages and frequencies. The interpretation of these measurements revealed values of the room temperature interface capacitance density as high as 1.55 F/m^2 in the SRO samples, which is at the order of magnitude as expected when having solely intrinsic influences and clearly outnumbers the values from previously reported studies. The polarization-voltage loops show that ferroelectricity can be found even at temperatures high above RT, which otherwise has not been reported yet. RT remanent polarization values of ~10 µC/cm^2 for the SRO sample and ~3 µC/cm^2 for the Pt sample (both ~130 nm) have been found, while in general the polarization loops are rather strongly slanted slim-loops.

- The analysis of the out-of-plane lattice constant revealed that both sample series are in the same thickness dependent strain state. The experimentally determined thickness dependence of the lattice constant agrees very well to a theoretically calculated one using a thermodynamic theory. From a Curie-Weiss type dependence of the permittivity on the lattice mismatch strain a thickness and strain dependent apparent interface capacitance has been evaluated as well as an estimate of the strain dependent shift of the phase transition temperature. The experimentally values for c_i and T_C agree fairly well with these theoretical estimates.
- Additional contributions from a depolarizing field to the apparent interface capacitance and the shift of the phase transition temperature have been discussed. Theoretical calculations

reveal that these contributions in the case of the intercept have a different sign compared to the strain influence, but can be roughly estimated to be in the same order of magnitude. Since the strain contribution has been shown to be the same in both series, a separation of the apparent interface capacitance into its components due to the assumed different depolarizing field contributions for Pt and SRO might be possible. Considering the influence of the depolarizing field on the phase transition temperature explains and corrects the inaccuracy that remains when comparing the observed thickness dependent phase transition temperatures with the calculated ones that were derived allowing solely strain contributions.

Those theoretical considerations have shown that the term „interface capacitance“ has to be used carefully. This parameter in general involves apparent contributions caused by the thickness dependence of the intrinsic film permittivity, and may also become negative in special cases. In the present case, the influences from the depolarizing fields as well those from the lattice mismatch strain are in the same order of magnitude and therefore may counteract each other. In general, the consideration of both mechanisms allows for a better understanding of the observed differences in the behavior of the two sample series.

The maximum permittivity values for the thickest BST films (~130 nm) have been determined as 3800 (SRO) and 2100 (Pt) and correspond to phase transition temperatures T_C of 360 K (SRO) and 310 K (Pt). In general, the BST thin film capacitors investigated here show a relaxorlike dependence of the permittivity on the applied excitation voltage amplitude, which can lead to an overestimation of the determined permittivity at higher excitation levels. In the case of the Pt samples this behavior is strongly obscured by the low interface capacitance and the correspondingly lower effective field at the bulk capacitor. By correcting the real effective field and the real bulk permittivity, a partial recovery of the relaxorlike properties of the Pt samples has been shown. Thus, relaxor properties in BST thin films are more pronounced when dealing with better (thus defect free) interfaces but in most cases have not been reported due to deteriorated electrode/film interfaces. In general, an inhomogeneous distribution of STO and BTO in the BST-matrix that leads to the formation of polar nanodomains may be responsible for the observed relaxor phenomenon.

In summary, the experimental findings result in dielectric properties by far exceeding what has been reported for comparable systems up to now. After all, the samples with oxide electrodes

(SRO) show a superior behavior compared to the Pt samples. Using the effects of misfit strain relaxation and depolarizing fields together with the nonlinear thermodynamic theory of ferroelectrics the experimentally observed thickness dependent shift of the phase transition temperature and the occurrence of a non-zero intercept in the linear fit of the reciprocal capacitance density can be understood. The partial suppression of the relaxor properties of BST thin films with Pt electrodes can be qualitatively explained by the less perfect film/electrode interface in these samples compared to the SRO samples.

7.2 Outlook

Further evaluation of Pt and SRO with respect to their suitability as electrode material in thin film BST capacitors should be considered. While the SRO layers can be regarded as high-quality single crystalline films, the Pt electrodes suffer from a poor interface to the BST: In addition to their non-epitaxial growth, contamination and amorphization of the interface is likely due to the incorporated ex-situ deposition process. Additional studies with epitaxial Pt electrodes and better interface characteristics are necessary to finally judge about any of the two´s applicability in an actual memory device.

With the awareness of the relaxor properties in the BST samples, some more investigations would be necessary to further understand its origins. One of the major questions in this context must be to asses the inhomogeneities on the nano-scale, comparable to the correlation length r_c of the dipole nanoclusters as mentioned in [137]. A variation of the material composition in a way that both epitaxial STO as well as $BaTiO_3$ (BTO) samples could be investigated would give a further insight into this issue: Since here no inhomogeneous distribution of any clusters is expected, also no relaxor behavior should occur.

As a major goal for future work, the elimination of the inhomogeneities in thin BST films (and thus the source of the relaxor-like properties) must be regarded. Having accomplished this task, it would seem possible to regain the real bulk properties of BST even in thin films of a few nm thickness. A similar recovery of bulk properties has been successfully achieved by Saad et al. in the case of BTO lamellae [102], where they eliminated the deleterious influence from defects in the thin films.

References

[1] O. Auciello, R. Waser (Eds.), Science and Technology of Electroceramic Thin Films, *NATO ASI-Series E: Applied Sciences* **284**, Kluwer Academic Publishers (1995)

[2] O. Auciello, R. Ramesh, Guest Editors, Electroceramic Thin Films, Part I: Processing, *Mat. Res. Bulletin* **21**, No. 6 (1996)

[3] O. Auciello, R. Ramesh, Guest Editors, Electroceramic Thin Films, Part II: Device Applications, *Mat. Res. Bulletin* **21**, No. 7 (1996)

[4] H. Schaumburg, *Keramik*, Bd. 5 der Reihe Werkstoffe und Bauelemente der Elektrotechnik, Teubner Verlag, Stuttgart (1994)

[5] R. Waser, *Nanoelectronics and Information Technology*, Wiley - VCH (2003)

[6] N. Setter, D. Damjanovic, L. Eng, G. Fox, S. Gevorgian, S. Hong, A. Kingon, H. Kohlstedt, N. Y Park, G. B. Stephenson, I. Stolichnov, A. K. Tagantsev, D. V. Taylor, T. Yamada, and S. Streiffer, Ferroelectric thin films: Review of materials, properties, and applications, *J. Appl. Phys.* **100**, 051606-1-46 (2006)

[7] J. F. Scott, Ferroelectric memories, *Physics World* **8,** 46-50 (1995)

[8] J. F. Scott and C. A. Paz de Araujo, Ferroelectric Memories, *Science* **246**, 1400-5 (1989)

[9] http://www.itrs.net/Links/2006Update/2006UpdateFinal.htm, *International Technology Roadmap for Semiconductors, 2006 Edition: Front End Processes* (2006)

[10] E. Fujii, Y. Uemoto, S. Hayashi, T. Nasu, Y. Shimada, A. Matsuda, M. Kibe, M. Azuma, T. Otsuki, G. Kano, M. Scott, L. D. McMillan, and C. A. Paz de Araujo, ULSI DRAM technology with $Ba_{0.7}Sr_{0.3}TiO_3$ film of 1.3 nm equivalent SiO_2 thickness and 10^{-9} A/ cm^2 leakage current, *Proceedings of IEEE International Electron Devices Meeting, San Francisco*, 267-70 (1992)

[11] B. E. Gnade, S. R. Summerfelt, D. Crenshaw, Processing and device issues of high permittivity materials for DRAMs, *Nato ASI Series E: Applied Sciences*, **284**, 373-82, O. Auciello and R. Waser (Editors), Kluwer Academic Publishers, Dordrecht (1995)

[12] D. E. Kotecki, A review of high dielectric materials for DRAM capacitors, *Integr. Ferroelectrics*, **16**, 1-20 (1997)

[13] T. M. Shaw, S. Trolier-McKinstry, and P. C. McIntyre, The Properties of Ferroelectric Films at small Dimensions, *Annu. Rev. Mater. Sci.* **30**, 263-298 (2000)

[14] D. E. Kotecki, J. D. Baniecki, H. Shen, R. B. Laibowitz, K. L. Saenger, J. J. Lian, T. M. Shaw, S. D. Athavale, Cabral-C-Jr, P. R. Duncombe, M. Gutsche, G. Kunkel, Y. J. Park, Y. Y. Wang, and R. Wise, $(Ba,Sr)TiO_3$ dielectrics for future stacked capacitor DRAM, *IBM J. Res. Develop.* **43**, 367-82 (1999)

[15] C. Basceri, S. K. Streiffer, A. I. Kingon, and R. Waser, The dielectric response as a function of temperature and film thickness of fiber-textured $(Ba,Sr)TiO_3$ thin films grown by chemical vapor deposition, *J. Appl. Phys.* **82**, 2497-504 (1997)

[16] L. J. Sinnamon, R. M. Bowman, and J. M. Gregg, Investigation of dead-layer thickness in $SrRuO_3/Ba_{0.5}Sr_{0.5}TiO_3/Au$ thin-film capacitors, *Appl. Phys. Lett.* **78**, 1724-6 (2001)

[17] C. B. Parker, J. P. Maria, and A. I. Kingon, Temperature and thickness dependent permittivity of $(Ba,Sr)TiO_3$ thin films, *Appl. Phys. Lett.* **81**, 340-2 (2002)

[18] J. McAneney, L. J. Sinnamon, R. M. Bowman, and J. M. Gregg, Temperature and frequency characteristics of the interfacial capacitance in thin-film barium-strontium-titanate capacitors, *J. Appl. Phys.* **94**, 4566-70 (2003)

[19] A. A. Sirenko, C. Bernhard, A. Golnik, A. M. Clark, J. Hao, W. Si, and X. X. Xi, Soft-mode hardening in $SrTiO_3$ thin films, *Nature* **404**, 373-6 (2000)

[20] C. Zhou and D. M. Newns, Intrinsic dead layer effect and the performance of ferroelectric thin film capacitors, *J. Appl. Phys.* **82**, 3081-3088 (1997)

[21] M. Izuha, K. Abe, and N. Fukushima, Electrical properties of all-perovskite oxide $(SrRuO_3/Ba_xSr_{1-x}TiO_3/SrRuO_3)$ capacitors, *Jpn. J. Appl. Phys.* **36**, 5866-9 (1997)

[22] I. Stolichnov, A. Tagantsev, N. Setter, J. S. Cross, and M. Tsukada, Control of leakage conduction of high-fatigue-endurance $(Pb,La)(Zr,Ti)O_3$ film ferroelectric capacitors with $Pt/SrRuO_3$ electrodes, *Appl. Phys. Lett.* **75**, 1790-2 (1999)

[23] D.-K. Choi, B.-S. Kim, S.-Y. Son, S.-H. Oh, and K.-W. Park, Evaluation of tailored electrode $(Ba,Sr)RuO_3$ for $(Ba,Sr)TiO_3$, *J. Appl. Phys.* **86**, 3347-51 (1999)

[24] V. Craciun and R. K. Singh, Characteristics of the surface layer of barium strontium titanate thin films deposited by laser ablation, *Appl. Phys. Lett.* **76**, 1932-4 (2000)

[25] S. Stemmer, G. R. Bai, N. D. Browning, and S. K Streiffer, Microstructure of epitaxial $Pb(Mg_{1/3}Nb_{2/3})O_3–PbTiO_3$ thin films grown by metalorganic chemical vapor deposition, *J. Appl. Phys.* **87**, 3526-31 (2000)

[26] C. L. Jia, K. Urban, S. Hoffmann, and R. Waser, Microstructure of columnar-grained SrTiO3 and BaTiO3 thin films prepared by chemical solution deposition, *J. Mater. Res.* **13**, 2206-9

[27] E. H. Rhoderick and R. H. Williams, *Metal-Semiconductor Contacts*, Clarendon Press, Oxford (1988)

[28] A. M. Cowley and S. M. Sze, Surface States and Barrier Height of Metal-Semiconductor Systems, *J. Appl. Phys.* **36**, 3212-20 (1965)

[29] W. Mönch, Role of virtual gap states and defects in metal-semiconductor contacts, *Phys. Rev. Lett.* **58**, 1260-3 (1987)

[30] H. Y. Ku and F. G. Ullman, Capacitance of thin dielectric structures, *J. Appl. Phys.* **35**, 265-267 (1964)

[31] C. T. Black and J. J. Welser, Electric-field penetration into metals: consequences for high-dielectric-constant capacitors, *IEEE Transactions on Electron Devices* **46**, 776-80 (1999)

[32] M. Dawber, L. J. Sinnamon, J. F. Scott, and J. M. Gregg, Electrode field penetration: A new interpretation of tunnelling currents in barium strontium titanate (BST) thin films, *Ferroelectrics* **268**, 35-40 (2002)

[33] M. Stengel and N. A. Spaldin, Origin of the dielectric dead layer in nanoscale capacitors, *Nature* **443**, 679-82 (2006)

[34] J. Junquera and P. Ghosez, Critical thickness for ferroelectricity in perovskite ultrathin films, *Nature* **422**, 506-9 (2003)

[35] C. S. Hwang, B. T. Lee, C. S. Kang, K. H. Lee, H.-J. Cho, H. Hideki, W. D. Kim, S. I. Lee, and M. Y. Lee, Depletion layer thickness and Schottky type carrier injection at the interface between Pt electrodes and (Ba, Sr)TiO3 thin films, *J. Appl. Phys.* **85**, 287-95, (1998)

[36] Q. X. Jia, X. D. Wu, S. R. Foltyn, and P. Tiwari, Structural and electrical properties of $Ba_{0.5}Sr_{0.5}TiO_3$ thin films with conductive $SrRuO_3$ bottom electrodes, *Appl. Phys. Lett.* **66**, 2197-9 (1995)

[37] K. Abe, N. Yanase, S. Komatsu, K. Sano, N. Fukushima, and T. Kawakubo, Dielectric and ferroelectric properties of heteroepitaxial $Ba_xSr_{1-x}TiO_3$ films grown on $SrRuO_3$/ $SrTiO_3$ substrates, *IEICE Transactions on Electronics,* **E81-C**, 505-12 (1998)

[38] P. K. Larsen, G. J. M. Dormans, D. J. Taylor, and P. J. van-Veldhoven, Ferroelectric properties and fatigue of $PbZr_{0.51}Ti_{0.49}O_3$ thin films of varying thickness: blocking layer model, *J. Appl. Phys.* **76**, 2405-13 (1994)

[39] A. K. Tagantsev and I. A. Stolichnov, Injection-controlled size effect on switching of ferroelectric thin films, *Appl. Phys. Lett.* **74**, 1326-8 (1999)

[40] M. E. Lines and A. M. Glass, *Principles and applications of ferroelectrics and related materials*, Clarendon Press, Oxford (1977)

[41] B. Jaffe, W. R. Cook, and H. Jaffe, *Piezoelectric ceramics*, Academic Press, London (1971)

[42] F. Jona and G. Shirane, *Ferroelectric Crystals*, Pergamon Press, Oxford, London, New York, Paris (1962)

[43] T. Mitsui, I. Tatsuzaki, and E. Nakamura, *Introduction to the physics of ferroelectrics*, Gordon & Breach, London (1976)

[44] C. Kittel, *Einführung in die Festkörperphysik, 12. tot. new rev. ed. (Introduction to solid state physics)*, Oldenbourg, München (1999)

[45] R. E. Newnham, *Structure-property relations*, Springer-Verlag, Berlin (1975)

[46] B. A. Strukov and A. P. Levanyuk, *Ferroelectric phenomena in crystals. Physical foundations*, Springer-Verlag, Berlin (1998)

[47] A. S. Sonin and B. A. Strukow, *Einführung in die Ferroelektrizität*, Vieweg, Braunschweig (1974)

[48] G. Fasching, *Werkstoffe für die Elektrotechnik*, Springer Verlag Wien New York (1984)

[49] H. - J. Martin, *Die Ferroelektrika*, Akademische Verlagsgesellschaft, Leipzig (1964)

[50] G. H. Haertling, Ferroelectric ceramics: history and technology, *J. Am. Ceram. Soc.* **82**, 797-818 (1999)

[51] N. Setter and R. Waser, Electroceramic materials, *Acta Mater.* **48**, 151-78 (2000)

[52] D. Damjanovic, Ferroelectric, dielectric and piezoelectric properties of ferroelectric thin films and ceramics, *Rep. Prog. Phys.* **61**, 1267-324 (1998)

[53] A. Hippel, R. G. Breckenridge, F. G. Chesley, and L. Tisza, High dielectric constant ceramics, *Ind. Eng. Chem.* **38**, 1097-109 (1946)

[54] B. M. Wul and I. M. Goldman, Dielectric constants of titanates of metals of the second group, *Compt. Rend. Acad. Sci. URSS* **49**, 139-42 (1945)

[55] A. Okazaki and M. Kawaminami, Lattice constant of strontium titanate at low temperatures, *Mater. Res. Bull.* **8**, 545-50 (1973)

[56] T. Mitsui and W. B. Westphal, Dielectric and X-ray studies of $Ca_xBa_{1-x}TiO_3$ and $Ca_xSr_{1-x}TiO_3$, *Phys. Rev.* **124**, 1354-1359 (1961)

[57] J. F. Scott, High-Dielectric Constant Thin Films for dynamic random access memories (DRAM). *Annu. Rev. Mater. Sci.* **28**, 79-100 (1999)

[58] A. I. Kingon, S. K. Streiffer, C. Basceri, and S. R. Summerfelt, High-permittivity perovskite thin films for dynamic random-access memories, *MRS Bull.* **21**, 46-52 (1996)

[59] I. Vendik, O. Vendik, V. Pleskachev, A. Svishchev, and R. Wordenweber, Design of tunable ferroelectric filters with a constant fractional band width, *IEEE MTT-S Int. Microwave Symp. Dig.* **3**, 1461-4 (2001)

[60] B. Acikel, Y. Liu, A. S. Nagra, T. R. Taylor, P. J. Hansen, J. S. Speck, and R. A. York, Phase shifters using (Ba,Sr)TiO_3 thin films on sapphire and glass substrates, *IEEE MTT-S Int. Microwave Symp. Dig.* **2**, 1191-4 (2001)

[61] S. Tappe, U. Böttger, and R. Waser, Investigation of the high frequency properties of BST thin films-a comparison of three different commonly used methods, *Int. Ferroelectrics* **53**, 455-64 (2003)

[62] M. McQuarrie, Structural Behavior in the System (Ba, Ca, Sr) TiO3 and its relation to certain dielectric characteristics, *J. Am. Cer. Soc.* **38**, 444 (1955)

[63] G. A. Smolenskii and K. I. Rozgachev, Ferroelectric properties in the barium titanate and strontium titanate solid solution system, *Zh. Tekh. Fiz.* **24**, 1751-60 (1954)

[64] A. D. Hilton and B. W. Ricketts, Dielectric properties of $Ba_{1-x}Sr_xTiO_3$ ceramics, *J. Phys.* **29**, 1321-5 (1996)

[65] C. B. Eom, R. B. Van-Dover, J. M. Phillips, D. J. Werder, J. H. Marshall, C. H. Chen, R. J. Cava, R. M. Fleming, and D. K. Fork, Fabrication and properties of epitaxial ferroelectric heterostructures with ($SrRuO_3$) isotropic metallic oxide electrodes, *Appl. Phys. Lett.* **63**, 2570-2 (1993)

[66] P. R. van Loan, Conductive ternary oxides of ruthenium, and their use in thick film resistor glazes, *Ceram. Bull.* **51**, 231-3 (1972)

[67] R. J. Bouchard and J. L. Gillson, Electrical properties of $CaRuO_3$ and $SrRuO_3$ single crystals, *Mater. Res. Bull.* **7**, 873-8 (1972)

[68] J. F. Scott, *Ferroelectric Memories*, Springer Verlag, Berlin Heidelberg (2000)

[69] A. J. Hartmann, M. Neilson, R. N. Lamb, K. Watanabe, and J. F. Scott, Ruthenium oxide and strontium ruthenate electrodes for ferroelectric thin-films capacitors, *Appl. Phys. A* **A70**, 239-42 (2000)

[70] B. S. Kwak, A. Erbil, B. J. Wilkens, J. D. Budai, M. F. Chisholm, and L. A. Boatner, Strain relaxation by domain formation in epitaxial ferroelectric thin films, *Phys. Rev. Lett.* **68**, 3733-6 (1992)

[71] J. S. Speck and W. Pompe, Domain configurations due to multiple misfit relaxation mechanisms in epitaxial ferroelectric thin films. I. Theory, *J. Appl. Phys.* **76**, 466-76 (1994)

[72] H. Kohlstedt, N. A. Pertsev, and R. Waser, Size effects on polarization in epitaxial ferroelectric films and the concept of ferroelectric tunnel junctions including first results, *Mater. Res. Soc. Symp. Proc.*, 161-72 (2002)

[73] J. W. Matthews and A. E. Blakeslee, Defects in epitaxial multilayers. I. Misfit dislocations, *J. Cryst. Growth* **27**, 118-25 (1974)

[74] Z. G. Ban and S. P. Alpay, Optimization of the tunability of barium strontium titanate films via epitaxial stresses, *J. Appl. Phys.* **93**, 504-11 (2003)

[75] N. A. Pertsev, A. G. Zembilgotov, and A. K. Tagantsev, Equilibrium states and phase transitions in epitaxial ferroelectric thin films, *Ferroelectrics* **223**, 79-90 (1999)

[76] N. A. Pertsev, A. G. Zembilgotov, and A. K. Tagantsev, Effect of mechanical boundary conditions on phase diagrams of epitaxial ferroelectric thin films, *Phys. Rev. Lett.* **80**, 1988-91 (1998)

[77] N. A. Pertsev, V. G. Koukhar, R. Waser, and S. Hoffmann, Curie-Weiss-type law for the strain and stress effects on the dielectric response of ferroelectric thin films, *Appl. Phys. Lett.* **77**, 2596-8 (2000)

[78] L. Landau, On the theory of phase transformations. I, *Phys. Z. Sowjet.* **11**, 26-47 (1937); L. Landau, On the theory of phase transformations. II, *Phys. Z. Sowjet.* **11**, 545-555 (1937)

[79] V. Ginzburg, On the dielectric properties of ferroelectric (Seignette-electric) crystals and barium titanate, *J. Phys., USSR* **10**, 107-115 (1946)

[80] A. F. Devonshire, Theory of barium titanate. I, *Philosophical Magazine, UK* **40**, 1040-1063 (1949); A. F. Devonshire, Theory of barium titanate. II, *Philosophical Magazine, UK* **42**, 1065-1079 (1951)

[81] N. A. Pertsev, V. G. Kukhar, H. Kohlstedt, and R. Waser, Phase diagrams and physical properties of single-domain epitaxial $Pb(Zr_{1-x}Ti_x)O_3$ thin films, *Phys. Rev. B: Condens. Matter,* **67**, 54107-1-10 (2003)

[82] N. A. Pertsev, J. R. Contreras, V. G. Kukhar, B. Hermanns, H. Kohlstedt, and R. Waser, Coercive field of ultrathin $Pb(Zr_{0.52}Ti_{0.48})O_3$ epitaxial films, *Appl. Phys. Lett.* **83**, 3356-8 (2003)

[83] M. J. Haun, E. Furman, S. J. Jang, and L. E. Cross, Thermodynamic theory of the lead zirconate-titanate solid solution system. I. Phenomenology, *Ferroelectrics* **99**, 13-25 (1989)

[84] P. C. Van Buskirk, J. F. Roeder, and S. Bilodeau, Manufacturing of perovskite thin films using liquid delivery MOCVD, *Int. Ferroelectrics* **10**, 9-22 (1995)

[85] T. Horikawa, N. Mikami, H. Ito, Y. Ohno, T. Makita, and K. Sato $(Ba_{0.75}Sr_{0.25})$ TiO_3 films for 256 Mbit DRAM, *IEICE Transactions on Electronics,* **E77-C**, 385-91 (1994)

[86] W.-J. Lee and H.-G. Kim, Electrical properties of barium strontium titanate (BST) thin films deposited on various Pt-base electrodes, *Int. Ferroelectrics* **11**, 111-9 (1995)

[87] C. S. Hwang, S. O. Park, H.-J. Cho, C. S. Kang, H.-K. Kang, S. I. Lee, and M. Y. Lee, Deposition of extremely thin (Ba,Sr)TiO3 thin films for ultra-large-scale integrated dynamic random access memory application, *Appl. Phys. Lett.* **67**, 2819-21 (1995)

[88] R. Waser, Dielectric analysis of integrated ceramic thin film capacitors, *Int. Ferroelectrics* **15**, 39-51 (1997)

[89] S. K. Streiffer, C. Basceri, C. B. Parker, S. E. Lash, and A. I. Kingon, Ferroelectricity in thin films: The dielectric response of fiber-textured $(Ba_xSr_{1-x})Ti_{1+y}O_{3+z}$ thin films grown by chemical vapor deposition, *J. Appl. Phys.* **86**, 4565-75 (1999)

[90] W. Y. Park, K. H. Ahn, and C. S. Hwang, Effects of in-plane compressive stress on electrical properties of (Ba,Sr)TiO3 thin film capacitors prepared by on- and off-axis rf magnetron sputtering, *Appl. Phys. Lett.* **83**, 4387-9 (2003)

[91] R. Dittmann, R. Plonka, E. Vasco, N. A. Pertsev, J. Q. He, C. L. Jia, S. Hoffmann-Eifert, and R. Waser, Sharp ferroelectric phase transition in strained single-crystalline $SrRuO_3$/ $Ba_{0.7}Sr_{0.3}TiO_3$/$SrRuO_3$ capacitors, *Appl. Phys. Lett.* **83**, 5011-13 (2003)

[92] R. Plonka, R. Dittmann, N. A. Pertsev, E. Vasco, and R. Waser, Impact of the top-electrode material on the permittivity of single-crystalline $Ba_{0.7}Sr_{0.3}TiO_3$ thin films, *Appl. Phys. Lett.* **86**, 202908-1-3 (2005)

[93] W. Känzig, Space Charge Layer Near the Surface of a Ferroelectric, *Phys. Rev.* **98**, 549-50 (1955)

[94] V. G. Bhide, R. T. Gondhalekar, and S. N. Shringi, Surface layers on ferroelectric $BaTiO_3$ crystals, *J. Appl. Phys.* **36**, 3825-33 (1965)

[95] U. Ellerkmann, R. Liedtke, U. Böttger, and R. Waser, Interface related thickness dependence of the tunability in $BaSrTiO_3$ thin films, *Appl. Phys. Lett.* **85**, 4708-10 (2004); U. Ellerkmann, Impact of the interface capacity on failure mechanisms and size effects in ferroelectric thin films, *PhD Thesis RWTH Aachen* (2006)

[96] A. Lookman, R. M. Bowman, J. M. Gregg, J. Kut, S. Rios, M. Dawber, A. Ruediger, and J. F. Scott, Thickness independence of true phase transition temperatures in barium strontium titanate films, *J. Appl. Phys.* **96**, 555-62 (2004)

[97] L. J. Sinnamon, R. M. Bowman, and J. M. Gregg, Thickness-induced stabilization of ferroelectricity in $SrRuO_3/Ba_{0.5}Sr_{0.5}TiO_3$/Au thin film capacitors, *Appl. Phys. Lett.* **81**, 889-91 (2002)

[98] S. Hoffmann, Modifizierte Erdalkalititanat-Dünnschichten für integrierte Bauelemente: Morphologie, dielektrische Eigenschaften und Ladungstransportmechanismen, *PhD Thesis RWTH Aachen* (1994)

[99] R. Liedtke, Herstellung, Charakterisierung und Bauelementsimulation von integrierten, elektrokeramischen Dünnschichtkondensatoren, *PhD Thesis RWTH Aachen* (2003)

[100] K. Abe and S. Komatsu, Dielectric constant and leakage current of epitaxially grown and polycrystalline $SrTiO_3$ thin films, *Jpn. J. Appl. Phys.* **32**, 4186-9 (1993)

[101] C. M. Chu and P. Lin, Electrical properties and crystal structures of $(Ba,Sr)TiO_3$ films and $BaRuO_3$ bottom electrodes prepared by sputtering, *Appl. Phys. Lett.* **72**, 1241-3 (1998)

[102] M. M. Saad, P. Baxter, R. M. Bowman, J. M. Gregg, F. D. Morrison, and J. F. Scott, Intrinsic dielectric response in ferroelectric nano-capacitors, *J. Phys.: Condens. Matter* **16**, L451-6 (2004)

[103] M.-S. Tsai, S. C. Sun, and T.-Y. Tseng, Effect of bottom electrode materials on the electrical and reliability characteristics of $(Ba, Sr)TiO_3$ capacitors, *IEEE Transactions on Electron Devices* **46**, 1829-38 (1999)

[104] O. G. Vendik and S. P. Zubko, Ferroelectric phase transition and maximum dielectric permittivity of displacement type ferroelectrics ($Ba_xSr_{1-x}TiO_3$), *J. Appl. Phys.* **88**, 5343-50 (2000)

[105] A. K. Tagantsev, V. O. Sherman, K. F. Astafiev, J. Venkatesh, and N. Setter, Ferroelectric Materials for Microwave Tunable Applications, *J. Electroceram.* **11**, 5-66 (2003)

[106] C. A. Mead, Anomalous capacitance of thin dielectric structure, *Phys. Rev. Lett.* **6**, 545-546 (1961)

[107] J. G. Simmons, An analytic form of Ku and ullmans equations, *Appl. Phys. Lett.* **6**, 54-55 (1965)

[108] D. J. Kim, J. Y. Jo, Y. S. Kim, Y. J. Chang, J. S. Lee, Yoon, T. K. Song, and T. W. Noh, Polarization relaxation induced by a depolarization field in ultrathin ferroelectric $BaTiO_3$ capacitors, *Phys. Rev. Lett.* **95**, 237602/1-4 (2005)

[109] M. Dawber and J. F. Scott, Models of electrode-dielectric interfaces in ferroelectric thin-film devices, *Jpn. J. Appl. Phys.* **41**, 6848-51 (2002)

[110] I. P. Batra, P. Wurfel, and B. D. Silverman, Phase transition, stability and depolarization field in ferroelectric thin films, *Phys. Rev. B (Solid State), USA* **8**, 3257-65 (1973)

[111] I. P. Batra, P. Wurfel, and B. D. Silverman, Depolarization field and stability considerations in thin ferroelectric films, *J. Vac. Sci. Technol., USA* **10**, 687-92 (1973)

[112] I. P. Batra, P. Wurfel, and B. D. Silverman, New type of first-order phase transition in ferroelectric thin films, *Phys. Rev. Lett.* **30**, 384-7 (1973)

[113] R. R. Mehta, B. D. Silverman, and J. T. Jacobs, Depolarization fields in thin ferroelectric films, *J. Appl. Phys.* **44**, 3379-85 (1973)

[114] M. Großmann, Imprint: An Important Failure Mechanism of Ferroelectric Thin Films in View of Memory Applications, *PhD Thesis RWTH Aachen* (2001)

[115] A. M. Bratkovsky and A. P. Levanyuk, Depolarizing field and "real" hysteresis loops in nanometer-scale ferroelectric films, arXiv:cond-mat/0608283 (2006)

[116] W. Cochran, Crystal stability and the theory of ferroelectricity, *Adv. Phys.* **9**, 387-423 (1960)

[117] U. Poppe, Herstellung von Oxidschichten mit physikalischen Methoden: Sputtern, reaktives Aufdampfen, Laserablation, in R. Hölzle (Ed.), *Elektrokeramische Materialien,* volume 26 of *Vorlesungsmanuskripte des IFF-Ferienkurses,* chapter B4, ppB4.1-38, Forschungszentrum Jülich GmbH, Jülich (1995)

[118] M. Klee, Schichtherstellung mit chemischen Methoden: Sol-Gel, MOD, in R. Hölzle (Ed.), *Elektrokeramische Materialien,* volume 26 of *Vorlesungsmanuskripte des IFF-Ferienkurses,* chapter B5, ppB5.1-16, Forschungszentrum Jülich GmbH, Jülich (1995)

[119] H. Schwarz and H. A. Tourtellotte, Vacuum deposition high-energy laser with emphasis on barium titanate films, *J. Vac. Sci. Technol.* **6**, 373-8 (1969)

[120] D. B. Chrisey and G. K. Hubler, *Pulsed Laser Deposition of Thin Films*, John Wiley & Sons, Inc. (1994)

[121] R. F. Pinizzotto, E. G. Jacobs, H. Yang, S. R. Summerfelt, and B. E. Gnade, Cross-sectional TEM studies of barium strontium titanate deposited on silicon by pulsed laser ablation, *Mater. Res. Soc*. 463-8 (1992)

[122] C. L. Chen, Y. Cao, Z. J. Huang, Q. D. Jiang, Z. Zhang, Y. Y. Sun, W. N. Kang, L. M. Dezaneti, W. K. Chu, and C. W. Chu, Epitaxial $SrRuO_3$ thin films on (001) $SrTiO_3$, *Appl. Phys. Lett.* **71**, 1047-9 (1997)

[123] Hewlett Packard, *HP 4194A Impedance/Gain-Phase Analyzer Operation Manual* (1996)

[124] Agilent Technologies, *Impedance Measurement Handbook* (2006)

[125] C. B. Sawyer and C. H. Tower, Rochelle Salt as a Dielectric, *Phys. Rev.* **35**, 269-73 (1930)

[126] O. Lohse, Verlustmechanismen in ferroelektrischen keramischen Dünnschichtkondensatoren für hochintegrierte nicht-flüchtige Halbleiterspeicher, *PhD Thesis RWTH Aachen* (2001)

[127] aixACCT Systems GmbH, Aachen, Germany, *manual of the TF Analyzer 2000 FE-Module*

[128] H. Krischner, *Einführung in die Röntgenfeinstrukturanalyse*, Vieweg, Braunschweig (1990)

[129] B.D. Cullity and S.R. Stock, *Elements of X-Ray Diffraction (3rd Edition)*, Prentice Hall (2001)

[130] W. Kraus and G. Nolze, *PowderCell, Version 2.3,* Federal Institute for Materials Research and Testing, Berlin, Germany

[131] J. Q. He, E. Vasco, C. L. Jia, R. Dittmann, and R. H. Wang, Microstructure of epitaxial $Ba_{0.7}Sr_{0.3}TiO_3/SrRuO_3$ bilayer films on $SrTiO_3$ substrates, *J. Appl. Phys.* **97**, 104907-1-5 (2005)

[132] D. Bolten, Reversible and Irreversible Polarization Processes in Ferroelectric Ceramics and Thin Films, *PhD Thesis RWTH Aachen* (2002)

[133] J. Rodriguez Contreras, Ferroelectric Tunnel Junctions, *PhD Thesis Universität zu Köln* (2003)

[134] M. Tyunina and J. Levoska, Coexistence of ferroelectric and relaxor properties in epitaxial films of $Ba_{1-x}Sr_xTiO_3$, *Physical Review B (Condensed Matter and Materials Physics), USA* **70**, 132105-1-4 (2004)

[135] D. V. Taylor and D. Damjanovic, Domain wall pinning contribution to the nonlinear dielectric permittivity in $Pb(Zr, Ti)O_3$ thin films, *Appl. Phys. Lett.* **73**, 2045-7 (1998)

[136] E. V. Colla, S. M. Gupta, and D. Viehland, Alternating current field effect on the freezing temperature of relaxor ferroelectrics, *J. Appl. Phys.* **85**, 362-7 (1999)

[137] G. A. Samara, The relaxational properties of compositionally disordered ABO_3 perovskites, *J. Phys. Condens. Mat.* **15**, R367-411 (2003)

[138] L. Zhou, P. M. Vilarinho, and J. L. Baptista, Dependence of the structural and dielectric properties of $Ba_{1-x}Sr_xTiO_3$ ceramic solid solutions on raw material processing, *J. Eur. Ceram. Soc.* **19**, 2015-20 (1999)

[139] R. Waser, U. Böttger, and S. Tiedke, *Polar Oxides: Properties, Characterization, and Imaging*, chapter 15, Wiley-VCH (2005)

[140] M. Tyunina, J. Levoska, S. Leppävuori, and A. Sternberg, Dielectric nonlinearities in ferroelectric thin-film heterostructures, *Appl. Phys. Lett.* **78**, 527-9 (2001)

[141] R. E. Peierls, The size of a dislocation, *Proc. Phys. Soc. Lond.* **52**, 34-7 (1940)

[142] Landolt-Börnstein, *Numerical Data and Functional Relationships in Science and Technology, New Series*, Vol. III/29a, Springer, Berlin, 1992; Y. S. Touloukian, R. K. Kirby, R. E. Taylor, and T. Y. R. Lee, *Thermal Expansion: Nonmetallic Solids (Thermophysical Properties of Matter*), Vol. 13, Plenum, New York, 1977

[143] N. A. Pertsev, A. K. Tagantsev, and N. Setter, Phase transitions and strain-induced ferroelectricity in $SrTiO_3$ epitaxial thin films, *Phys. Rev. B: Condens. Matter,* **61**, R825-9 (2000)

[144] N. A. Pertsev, R. Dittmann, R. Plonka, and R. Waser, Thickness dependence of intrinsic dielectric response and apparent interfacial capacitance in ferroelectric thin films, *J. Appl. Phys.* **101**, 074102-1-9 (2007)

Jül-4266
März 2008
ISSN 0944-2952

JÜLICH
FORSCHUNGSZENTRUM